

# Discrete Element Modeling of a Vibratory Subsoiler

by

Jaco van der Linde

*Thesis presented in partial fulfilment of the requirements for  
the degree of Master of Science in Mechanical Engineering at  
the University of Stellenbosch*



Department of Mechanical and Mechatronic Engineering,  
University of Stellenbosch,  
Private Bag X1, 7602 Matieland, South Africa.

Supervisor: Mr. D.N.J. Els

December 2007

# Declaration

I, the undersigned, hereby declare that the work contained in this thesis is my own original work and that I have not previously in its entirety or in part submitted it at any university for a degree.

Signature: .....  
J. van der Linde

Date: .....

Copyright © 2007 University of Stellenbosch  
All rights reserved.

# Abstract

## Discrete Element Modeling of a Vibratory Subsoiler

J. van der Linde

*Department of Mechanical and Mechatronic Engineering,  
University of Stellenbosch,  
Private Bag X1, 7602 Matieland, South Africa.*

Thesis: MScEng (Mech)

December 2007

Vibrating a tillage tool is an effective way of reducing the draft force required to pull it through the soil. The degree of draft force reduction is dependent on the combination of operating parameters and soil conditions. It is thus necessary to optimize the vibratory implement for different conditions.

Numerical modelling is more flexible than experimental testing and analytical models, and less costly than experimental testing. The Discrete Element Method (DEM) was specifically developed for granular materials such as soils and can be used to model a vibrating tillage tool for its design and optimization. The goal was thus to evaluate the ability of DEM to model a vibratory subsoiler and to investigate the cause of the draft force reduction.

The DEM model was evaluated against data obtained from field testing done with a full scale single tine vibratory subsoiler. Soil testing was also done for material characterization and for the calibration of DEM material properties.

The subsoiler was simulated using a commercial code, *PFC3D*. The effect on the simulation results of particle diameter, different bonding models and damping models was investigated. The final simulations were evaluated against the experimental results in terms of the draft force and material behaviour. The cause of the draft force reduction due to vibration was also investigated with the aid of the DEM model.

From the results it was concluded that DEM is able to model the vibratory subsoiler for its design and optimization. The DEM model also provided valuable insight into the cause of the draft force reduction such as the increased peak stresses due to vibration and the increase in particle kinetic energy.

# Uittreksel

## Diskrete Element Modelling van 'n Vibrerende Skeurploeg

J. van der Linde

*Departement Meganiese en Megatroniese Ingenieurswese,  
Universiteit van Stellenbosch,  
Privaatsak X1, 7602 Matieland, Suid Afrika.*

Tesis: MScIng (Meg)

Desember 2007

Om 'n tand implement te vibreer is 'n effektiewe manier om die trekkrag, wat benodig word om dit deur die grond te trek, te verminder. Die graad van krag vermindering is afhanklik van die kombinasie van werks parameters en die grond toestand. Dus is dit nodig om die vibrerende implement te optimeer vir verskillende omstandighede.

Numeriese modulering is meer buigsaam en goedkoper as eksperimentele opstellings en analitiese modelle. Die Diskrete Element Metode (DEM) was spesifiek vir korrelrige materiaal, soos grond, ontwikkel en kan gebruik word vir die modellering van 'n vibrerende implement vir die ontwerp en optimering daarvan. Die doel was dus om die vermoë van DEM om 'n vibrerende skeurploeg te modelleer, te evalueer, en om die oorsaak van die krag vermindering te ondersoek.

Die DEM model was geëvalueer teen data wat verkry is van toetse wat gedoen is met 'n volskaalse vibrerende skeurploeg. Grond toetse was ook gedoen vir materiaal karakterisering en vir die kalibrasie van die DEM materiaal eienskappe.

Die skeurploeg was gesimuleer met 'n komersiële kode, *PFC3D*. Die effek, op simulasië resultate, van partikel deursnee, verskillende bindings modelle en dempings modelle was ondersoek. Die finale simulasië was geëvalueer teen die eksperimentele resultate in terme van trekkrag en materiaal gedrag. Die oorsaak van die trekkrag vermindering as gevolg van die vibrasie was ook ondersoek met behulp van die DEM model.

Vanaf die resultate was dit afgelyk dat DEM gebruik kan word vir die modellering van die vibrerende skeurploeg vir die ontwerp en optimering daarvan. Die DEM



model het ook nuttige inligting verskaf oor die oorsaak van die trekkrag vermindering soos die toeneeming in piek spannings as gevolg van vibrasie en die toename in partikler kinetiese energie.

# Acknowledgements

I would like to express my sincere gratitude to the following people and organizations who have contributed to making this work possible:

- The Government Department of Agriculture at Elsenburg for the use of their land and machinery for the field test.
- Dr. Marius De Wet at the Department of Civil Engineering for the use of their soil testing equipment.
- Dr. Eduart Hoffmann and the laboratory staff of the Department of Soil Science for the soil calcification.
- The technical staff of the Department of Mechanical Engineering for the help with measurement equipment.
- Mr Danie Els as my supervisor

# Contents

<b>Declaration</b>	<b>i</b>
<b>Abstract</b>	<b>ii</b>
<b>Uittreksel</b>	<b>iii</b>
<b>Acknowledgements</b>	<b>v</b>
<b>Contents</b>	<b>vi</b>
<b>List of Figures</b>	<b>x</b>
<b>List of Tables</b>	<b>xii</b>
<b>Nomenclature</b>	<b>xiv</b>
<b>1 Introduction</b>	<b>1</b>
1.1 Background . . . . .	1
1.2 Project Objectives . . . . .	2
1.3 Project Overview . . . . .	3
1.4 Significance . . . . .	4
<b>2 Literature Review</b>	<b>5</b>
2.1 Vibratory Tillage . . . . .	5
2.1.1 Experimental Testing . . . . .	6
2.1.2 Mathematical Models . . . . .	10
2.1.3 Numerical Simulation . . . . .	11
2.2 Tillage Tool Design and Modeling . . . . .	12
2.2.1 Mathematical Models . . . . .	13
2.2.2 Finite Element Method (FEM) . . . . .	14
2.2.3 Discrete Element Method (DEM) . . . . .	15
2.3 Concluding Remarks . . . . .	16

<b>3</b>	<b>Discrete Element Modelling Theory</b>	<b>18</b>
3.1	Calculation Cycle . . . . .	19
3.2	Contact Forces . . . . .	20
3.2.1	Normal Force Model . . . . .	21
3.2.2	Tangential Force Models . . . . .	24
3.2.3	Bonding Models . . . . .	25
3.3	Numerical Methods . . . . .	26
3.4	DEM Software . . . . .	27
3.5	Concluding Remarks . . . . .	29
<b>4</b>	<b>Field Tests</b>	<b>30</b>
4.1	Test Site . . . . .	30
4.2	Soil Tests . . . . .	31
4.3	Test Equipment . . . . .	35
4.3.1	Subsoiler . . . . .	35
4.3.2	Measuring Equipment . . . . .	35
4.4	Test Specifications and Procedure . . . . .	37
4.5	Results and Observation . . . . .	39
4.5.1	Test Results . . . . .	39
4.5.2	Observation . . . . .	41
4.6	Conclusion and Recommendations on Experiments . . . . .	42
4.6.1	Conclusion . . . . .	42
4.6.2	Recommendations . . . . .	44
<b>5</b>	<b>Material Property Calibration</b>	<b>45</b>
5.1	Particle Size and Shape . . . . .	46
5.2	Particle Density . . . . .	46
5.3	Particle Stiffness . . . . .	47
5.4	Internal Friction Angle and Cohesion . . . . .	50
5.5	Soil/Metal Friction Coefficient . . . . .	50
5.6	Damping Constant . . . . .	52
5.7	Conclusion . . . . .	53
<b>6</b>	<b>Simulations Setup</b>	<b>54</b>
6.1	Soil Bin and Subsoiler Tine . . . . .	54
6.2	Simulation Specifics . . . . .	55
6.2.1	Tine Movement . . . . .	55
6.2.2	Parameter Extraction . . . . .	56
6.2.3	Simulation Parameters . . . . .	58

<b>7</b>	<b>Simulation Results</b>	<b>59</b>
7.1	Effect of Particle Diameter . . . . .	59
7.1.1	Effect on Draft Force . . . . .	59
7.1.2	Effect on Material Behaviour . . . . .	60
7.1.3	Conclusion on the Effect of Particle Diameter . . . . .	61
7.2	Effect of Bonding Models . . . . .	61
7.2.1	Contact Bonds . . . . .	61
7.2.2	Parallel Bonds . . . . .	62
7.2.3	Conclusion on Bonding Models . . . . .	62
7.3	Damping Effect . . . . .	63
7.3.1	Global Damping . . . . .	63
7.3.2	No Damping . . . . .	64
7.3.3	Viscous Damping . . . . .	64
7.3.4	Conclusion on Damping Model . . . . .	65
7.4	Final Simulation Results and Observations . . . . .	65
7.4.1	Results . . . . .	65
7.4.2	Observations . . . . .	66
7.5	Discussion . . . . .	67
7.5.1	Draft Forces . . . . .	67
7.5.2	Power Consumption . . . . .	70
7.5.3	Material Behaviour . . . . .	71
7.6	Vibration: Why it Reduces the Draft Force . . . . .	71
<b>8</b>	<b>Conclusion and Recommendations</b>	<b>75</b>
8.1	Conclusion . . . . .	75
8.2	Recommendation . . . . .	76
<b>A</b>	<b>PFC 3D Detail</b>	<b>78</b>
	Nomenclature . . . . .	78
A.1	Notation and Conventions . . . . .	79
A.2	Calculation Cycle . . . . .	80
A.3	Force-Displacement Law . . . . .	80
A.4	Law of Motion . . . . .	85
A.5	Time Step Determination . . . . .	86
A.6	Mechanical Damping . . . . .	88
A.7	Contact Models . . . . .	91
A.7.1	Contact-Stiffness Models . . . . .	91
A.7.2	Slip Model . . . . .	93
A.7.3	Bonding Models . . . . .	93
A.8	Contact Detection . . . . .	97

<b>B Measurement Device Setup and Calibration</b>	<b>98</b>
B.1 Strain Gauge Setup and Calibration . . . . .	98
B.1.1 Setup . . . . .	98
B.1.2 Calibration . . . . .	98
B.2 Shear Box Sensor Calibration . . . . .	101
<b>C Soil Property Testing</b>	<b>105</b>
C.1 Direct Shear Tests . . . . .	105
C.2 Soil/Metal Friction Coefficient . . . . .	106
C.3 Compression Test . . . . .	109
C.4 Particle Size Analysis . . . . .	109
C.5 Bulk Density . . . . .	111
C.6 Moisture Content . . . . .	113
<b>D Experimental Data</b>	<b>114</b>
D.1 Draft Force . . . . .	114
D.2 Soil Profile Measurement . . . . .	115
<b>E Simulation Data</b>	<b>118</b>
E.1 Draft Force . . . . .	118
E.2 Power Requirement . . . . .	120
E.3 Soil Stresses . . . . .	122
<b>List of References</b>	<b>124</b>

# List of Figures

2.1.1	Vibrating angle . . . . .	7
3.2.1	General force model . . . . .	21
3.2.2	Walton-Braun normal force model (Vu-Quoc <i>et al.</i> , 2000) . . . . .	23
4.1.1	Depth profile of soil . . . . .	31
4.2.1	Direct shear apparatus . . . . .	32
4.2.2	Compression test results . . . . .	34
4.3.1	Subsoiler used for testing . . . . .	35
4.3.2	Pin profile meter . . . . .	37
4.5.1	Typical test data set for 12 Hz frequency . . . . .	40
4.5.2	Typical soil profile measurement . . . . .	42
4.5.3	Effect of vibration on clot size . . . . .	43
5.3.1	Typical force vs displacement graph for stiffness calibration . . . . .	48
5.4.1	Shear box for direct shear test simulation (shown at the end of shear cycle) . . . . .	51
5.5.1	Shear box for soil/metal friction calibration (shown at the end of shear cycle) . . . . .	52
6.1.1	Soil bin dimensions . . . . .	55
6.1.2	Front and left view of simulation subsoiler tine . . . . .	56
6.2.1	Tine at beginning of simulation and measurement sphere positions . . . . .	57
7.2.1	Failure surface left by tine, as seen from the rear . . . . .	62
7.2.2	Top view of failure surface left by tine . . . . .	63
7.4.1	Draft reduction obtained from simulations . . . . .	66
7.4.2	Power consumption from simulations . . . . .	67
7.4.3	Top view of parallel bonds after simulation runs . . . . .	68
7.4.4	Cross section view of parallel bonds after simulation runs . . . . .	68
7.4.5	Side view of parallel bonds after simulation run . . . . .	69
7.5.1	Cumulative work done by tine on particles . . . . .	70

7.6.1	Particle kinetic energy . . . . .	72
7.6.2	Maximum shear stress in particle assembly at measurement sphere 4 . . . . .	73
A.2.1	<i>PFC3D</i> calculation cycle . . . . .	81
A.3.1	Ball-ball contact notation . . . . .	82
A.3.2	Ball-wall contact notation . . . . .	83
A.5.1	Multiple mass-spring system . . . . .	87
A.6.1	Viscous damping at contacts . . . . .	90
A.7.1	Parallel bond . . . . .	95
B.1.1	Full bridge wiring diagram . . . . .	99
B.1.2	Calibration setup and load cell connection . . . . .	100
B.1.3	Typical calibration curve (top link) . . . . .	101
B.2.1	Instron calibration device . . . . .	103
B.2.2	Calibration curve for vertical displacement LVDT . . . . .	104
C.1.1	Shear force vs. time for 2kg normal load . . . . .	106
C.1.2	Shear stress vs. normal stress with linear regression line . . . . .	107
C.2.1	Shear stress vs. normal stress for soil/metal friction coefficient with linear regression line . . . . .	108
D.1.1	Horizontal force components for a test run without vibration . . . . .	115
D.1.2	Horizontal force components for a test run with vibration . . . . .	116
E.1.1	Draft force for a simulation run with and without vibration . . . . .	119
E.2.1	Subsoiler crank and pivot layout . . . . .	120
E.2.2	Torque on crank shaft . . . . .	121



# List of Tables

3.4.1	<i>PFC3D</i> Assumptions . . . . .	28
4.2.1	Soil properties . . . . .	32
4.3.1	Sprocket combinations and vibrating frequencies . . . . .	36
4.4.1	Test parameters . . . . .	38
4.5.1	Draft force test results . . . . .	41
5.2.1	Particle densities for bulk density of 1690 kg/m <sup>3</sup> . . . . .	47
5.3.1	Particle stiffness as calibrated . . . . .	49
5.3.2	Particle stiffness used in simulations . . . . .	49
5.4.1	Particle shear test parameters: Contact bonds . . . . .	51
5.4.2	Particle shear test parameters: Parallel bonds . . . . .	51
6.2.1	Subsoiler operating parameters for simulations . . . . .	58
B.1.1	Strain gauge specifications . . . . .	99
B.1.2	Spider™ information . . . . .	100
B.1.3	Calibration constants . . . . .	101
B.2.1	Shear box load cell information . . . . .	102
B.2.2	LVDT information . . . . .	102
B.2.3	Calibration constants for LVDTs . . . . .	103
C.1.1	Shear box dimensions . . . . .	105
C.1.2	Shear test data and results . . . . .	107
C.2.1	Shear test data and results for soil/metal friction coefficient . . . . .	108
C.4.1	Soil fraction percentages . . . . .	111
C.4.2	Average fraction content over depth of soil . . . . .	111
C.5.1	Parameters for density calculation . . . . .	112
C.5.2	Sample densities . . . . .	113
C.5.3	Average densities . . . . .	113
C.6.1	Moisture content . . . . .	113

D.1.1	Draft results for 12,7 Hz test . . . . .	115
D.1.2	Draft results for 16,1 Hz test . . . . .	116
D.2.1	Area loosened for 12,7 Hz frequency . . . . .	117
D.2.2	Area loosened for 16,1 Hz frequency . . . . .	117
E.1.1	Draft force for simulation <i>run</i> 1 (30 mm amplitude) . . . . .	118
E.1.2	Draft force for simulation <i>run</i> 2 (40 mm amplitude) . . . . .	119
E.2.1	Power consumption data for simulation <i>run</i> 1 (30 mm amplitude) . .	122
E.2.2	Power consumption data for simulation <i>run</i> 2 (40 mm amplitude) . .	122

# Nomenclature

This nomenclature refers to the whole report except for Appendix A, which has its own notation, convention and symbols. All symbols in bold with an over line are vectors, for example  $\overline{\mathbf{F}}$  denotes a force vector. Symbols in bold with an over line and underline are matrices or tensors, for example  $\underline{\overline{\mathbf{I}}}$  is a moment of inertia matrix.

## Constants

$g$  Gravitational acceleration:  $g = 9,81 \text{ m/s}^2$

## Variables

$A$  Amplitude of sinusoidal function or area  
 $C_c$  Corrected concentration of soil fraction (equation C.4.1)  
 $D_c$  Concentration Factor (equation C.4.1)  
 $E$  Elastic modulus of particle  
 $F$  Force  
 $I$  Moment of inertia  
 $L$  Distance between tine pivot point and connecting rod pivot  
 $M$  Moment  
 $N_p$  Number of particles (equation E.3.1)  
 $P$  Pressure  
 $R$  Particle radius (chapter 3). Moment arm (equation E.2.2)  
 $V$  Velocity (equation 2.1.1). Volume (pipet volume along with subscript  $p$  in equation C.4.1 and particle volume along with superscript  $p$  in equation E.3.1)

$a$  Velocity ratio  
 $c$  Damping constant except for equation 3.2.14 where it is cohesion  
 $d$  Working depth (section 2.2.1)  
 $e$  Restitution coefficient

$h$	Horizontal distance on soil profile meter (equation (D.2.1))
$k$	Stiffness (chapter 3)
$m$	Mass
$n$	Porosity (equation E.3.1)
$\Delta n$	Relative normal displacement between particles (chapter 3)
$r$	Moment arm of loading frame (equation C.1.1)
$\Delta s$	Relative tangential (shear) displacement between particles (chapter 3)
$t$	Time
$\Delta t$	Length of time step (chapter 3)
$w$	Tine width (section 2.2.1)
$x$	Particle displacement (chapter 3)
$\dot{x}$	Particle velocity (chapter 3)
$\ddot{x}$	Particle acceleration (chapter 3)
$y$	Vertical displacement measured on profile meter (equation (D.2.1))
$\Omega$	Angular velocity of tine (equation 6.2.1)
$\beta$	Critical damping ratio (equation (5.6.1))
$\delta$	Overlap distance (chapter 3)
$\dot{\delta}$	Relative velocity at the contact between particles (chapter 3)
$\phi_\mu$	Particle friction angle (equation 3.2.14)
$\mu$	Friction coefficient (chapter 3)
$\nu$	Particle poisson's ratio (chapter 3)
$\theta$	Angular displacement of particles (chapter 3)
$\dot{\theta}$	Angular velocity of particles (chapter 3)
$\ddot{\theta}$	Angular acceleration of particles (chapter 3)
$\theta_w$	Moisture content (equation 4.2.2 and C.5.2)
$\rho$	Density
$\sigma$	Normal stress (appendix E)
$\tau$	Shear stress (appendix E)
$\omega$	Vibrating frequency in rad/s, or rotational velocity (rad/s) in equation E.2.2

**Superscripts**

$p$  Refers to particle stress and volume (equation E.3.1)

**Subscripts**

$cr$  Refer to connecting rod (equation E.2.1)

$crank$  Refer to crank shaft (equation E.2.2)

$i$  Particle number or index

$j$  Contact number or index (chapter 3)

$n$  Specify normal direction

$ods$  Refer to mass of oven dry soil (equations 4.2.1, 4.2.2, C.5.1 and C.5.2)

$p$  In equation 4.2.1 and C.5.1 it refers to density of wax and in equation C.4.1 it refers to the volume of pipet sample

$pa$  Refers to mass of wax layer in air (equation 4.2.1 and C.5.1)

$s$  Specify tangential or shear direction

$sa$  Refers to mass of soil in air (equation 4.2.1 and C.5.1)

$spw$  Refers to the combined mass of soil and wax layer in water (equation 4.2.1 and C.5.1)

$t$  Refers to time step (chapter 3)

$w$  Refers to density of water (equation 4.2.1 and C.5.1)

$x$  Refers to coordinate direction or tensor index (equation E.3.2)

$y$  Refers to coordinate direction or tensor index (equation E.3.2)

$z$  Refers to coordinate direction or tensor index (equation E.3.2)

**Frequently used terms and abbreviations**

DEM Discrete Element Modeling

FEM Finite Element Modeling

LVDT Linear Variable Differential Transducer

*PFC2D* Particle Flow Code in 2 Dimensions (DEM software)

*PFC3D* Particle Flow Code in 3 Dimensions (DEM software)

PTO Power Take Off. Refers to PTO shaft of tractor

*run 1* Refer to simulations done with an amplitude of 30 mm

*run 2* Refers to simulations done with an amplitude of 40 mm

Spider™ Hotinger Baldwin Messtechnik (HBM) Spider8 electronic measurement system

USDA United States Department of Agriculture

# Chapter 1

## Introduction

### 1.1 Background

In recent years the South African agricultural sector has become ever more pressurized due to lower grain prices and increasing input costs. Environmental concerns have also begun to change conventional agricultural activities. The introduction of conservation farming, in the form of conservation tillage and no-till planting, resulted in a cut in input costs and a reduction in negative soil impact, such as compaction and erosion.

Soil compaction and hardpan reduces the water permeability of the soil and obstructs drainage. It also prevents the proper root development of plants.

In spite of these conservation techniques, deep soil tillage and hardpan shattering are still major contributors to input costs. Conventional tillage is still practiced in large parts of South Africa, especially in the maize growing areas, where subsoiling is done every season to deep-loosen the soil.

As deep tillage operations, such as subsoiling, are associated with large draft forces, they result in large amounts of energy and time consumption. Therefore, a draft force reduction would decrease these high input costs.

It has been proven by various researchers that vibrating a tillage tool is an effective method of reducing the draft force (section 2.1.1). However, it was also found that the overall power requirement increase as a result of the vibration (section 2.1.1). Also found in literature is that the vibration increases the soil brake up and the amount of soil disturbed (section 2.1.1).

The draft force reduction has several advantages including the use of a lighter tractor for less soil compaction and less rolling resistance due to a lower ballasting requirement. Wheel slip is also decreased, which reduces tyre wear, increases true ground speed and overall productivity. Draft force reduction also offers the possibility of using a larger implements for increased area coverage or smaller tractors

for deep tillage where space is limited such as in vineyards and orchards.

The effectiveness of a vibratory subsoiler is highly dependent on operating parameters such as the oscillating frequency, amplitude and forward speed. Soil parameters such as moisture content and soil type also play a significant role. Thus, the optimum operating parameters may differ for different soil types and soil conditions making optimization difficult.

Commercially available tillage tools are being designed from experience and prototype testing, which is an effective way to evaluate different designs. However, optimizing a vibratory tillage tool with prototype testing alone will require more finances and time (compared to a non-vibrating tool), due to the number of parameter combinations influencing its performance.

Various mathematical models (sections 2.1.2 and 2.2.1) exist for the prediction of tillage tool forces and flow patterns. These models were, however, developed from experiments for specific tools in specific circumstances. It can thus not be used for the design and optimization, or the evaluation of the effects of different parameters of a vibratory tillage tool.

Methods such as Finite Element Modelling (FEM) (section 2.2.2) were also used in the analysis of tillage tools. FEM is capable of modelling the effect of tool shape on the draft forces, and even the pressure distribution on a tillage tool. However, FEM is unable to model the large soil displacements during tillage. Furthermore, it cannot model the material flow and failure patterns around the tillage tool and therefore is unable to model the reaction caused by the vibration. It is thus necessary to find another method to model tillage tools and vibratory tillage tools for the optimization and design thereof.

The Discrete Element Method (DEM) is capable of simulating the large displacements involved in soil tillage as well as the behaviour of the soil under vibratory loading. This makes DEM particularly suitable for the modelling of the vibratory subsoiler.

The abilities of DEM have been illustrated in the simulation of earthmoving machinery (section 2.2.3), as well as in two-dimensional simulations of a vibratory subsoiler (section 2.1.3). This thesis is currently the second DEM simulation of a vibratory subsoiler as well as the first three-dimensional DEM simulation of an agricultural tillage tool.

## 1.2 Project Objectives

The main aim of this project was to evaluate the ability of DEM to simulate a vibratory subsoiler. The simulation data was evaluated against experimental data

on the basis of draft forces and material behaviour such as the size and shape of failure patterns, clot formation etc.

The secondary aim of this project was to use the simulation data to help understand why vibration reduces the draft force of a vibratory implement. This information could also facilitate future research into the optimization of vibratory tillage tools.

The time restraint placed on this project did not allow for the optimization of the subsoiler. It also limited the simulation model to a simple rudimentary model; only making use of the built-in functions of the available software *PFC3D* (Itasca, 2003a).

### 1.3 Project Overview

The following steps were followed in order to reach the predetermined goals of this project:

- A literature study on vibrating tillage tools and DEM was done.
- Field tests on the vibratory subsoiler to collect experimental data were carried out.
- Soil samples were taken and material property tests on the soil were done.
- *PFC3D* model material properties were calibrated.
- *PFC3D* model of the vibrating subsoiler was set up and simulations were run.
- Simulation results were compared to the experimental results.
- The cause of draft force reduction was investigated by analyzing simulation models.

The literature study gives background information on vibratory tillage, namely, what has been established in the past as well as the known effects of vibration on the soil. The fundamentals of DEM and the available DEM software, *PFC3D*, was also studied in this section to determine the abilities and limitation of DEM in modeling a vibratory subsoiler.

The literature study is spread across two chapters. While Chapter 2 covers the literature on vibratory tillage, and tillage tool design and analysis, Chapter 3 covers the literature on DEM and describes the basic working of DEM.



Chapter 4 describes the field test of the vibratory subsoiler along with the test results, conclusion and recommendations on the tests. This chapter also covers the soil property testing that was done at the same time as the subsoiler tests.

Chapter 5 describes the calibration process that was followed for the characterization of the simulation material. The material properties determined during the soil test were used to calibrate the material properties of the DEM model.

Chapter 6 describes the subsoiler simulation setup, followed by the simulation results as well as the observations made during the simulations in Chapter 7. The comparison between the simulations and the field test as well as the discussion on 'why the vibration reduces the draft force' are also included in Chapter 7. The effects of different simulation parameters on the results and material behaviour are also depicted.

A final conclusion on the project is made in Chapter 8 along with recommendations for further work in the simulation of tillage tools.

## 1.4 Significance

This project corroborates literature findings by demonstrating that the vibratory subsoiler reduces the draft force and increase soil pulverization. This is shown in the experimental work as well as in the computer simulations.

Further more, this project illustrates the ability of DEM to simulate the vibratory subsoiler as well as its usefulness in the study of the effect of vibration on the soil. Valuable insight into why vibration reduces the draft force was also obtained.

# Chapter 2

## Literature Review

This part of the literature review covers two important aspects of this project, namely vibratory tillage and methods of tillage tool analysis.

The section on vibratory tillage will show that vibration reduces the draft force significantly and that a vibrating implement increases the soil pulverization. Most of the research done on vibratory implements was experimental testing, each with their own set of operating parameters and conditions. The effects of the different operating parameters are also covered along with the benefits of using a vibratory implement. This section will thus emphasize the need for optimization and further research into vibratory tillage tools. It will also discuss the effects of vibration on the soil and the reasons why vibration reduces the draft force. It will also point out the need for computer simulations of tillage tools.

This section is broken up into subsections covering experimental testing, mathematical models and the sole DEM model of vibratory tillage tools, respectively.

The next section deals with the methods of analyzing tillage tools and the interaction of the tool with the soil. It discusses various mathematical models of tillage as well as the use of FEM in tillage tool analysis. The shortcomings of the above mentioned methods are pointed out, highlighting the need for DEM modelling in tillage tool analysis.

### 2.1 Vibratory Tillage

Research into vibrating tillage tools began in the early nineteen fifties and is still researched today. Past research includes papers varying in degrees of significance to this particular thesis. As some of the information in the earlier papers is found obsolete, only the relevant research will be discussed.

A common parameter referred to in vibratory tillage is the velocity ratio. The velocity ratio is defined as the ratio between the peak tool velocity and the velocity

of the tool carrier and can be expressed as follows:

$$a = \frac{A\omega}{V_c} \quad (2.1.1)$$

Where  $A$  is the vibration amplitude in meter,  $\omega$  is the vibrating frequency (rad/s) and  $V_c$  is the carriage velocity (m/s) (constant forward velocity of tool carrier).

Other parameters often used are draft ratio and power ratio. The draft ratio is defined as the ratio of draft force obtained with vibration to the draft force obtained without vibration. The power ratio is defined in the same way by being the ratio between the total power requirement with vibration and the total power requirement without vibration.

## 2.1.1 Experimental Testing

### Draft force reduction

Sakai *et al.* (1993) designed and tested a four shank vibratory subsoiler. This machine was designed to allow a small tractor to do deep soil tillage. The best results obtained were a 60% reduction in draft force (draft ratio of 0,4) with a 2% increase in power requirement. This was achieved with a 50 mm amplitude, 3,4 Hz oscillating frequency, velocity ratio of 2,5 and a vibrating angle of 30°.

This paper introduces an extra parameter, the vibrating angel, and is one of only a few papers to report the effect of the vibrating angle. The vibrating angle is defined as the angle between the horizontal and the tangent line to the movement path of the tine tip as shown in figure 2.1.1.

It was shown in Sakai *et al.* (1993) that an increase in velocity ratio increases the draft reduction up to a point, then it flattens off and decreases slightly. The overall power requirement also increases continuously with an increase in velocity ratio. A larger amplitude, lower frequency vibration, with the same velocity ratio, showed a higher draft reduction with lower power requirement. An increase in the vibrating angle also increases the draft reduction, however, a vibrating angle above 30° made it difficult to control the working depth of the implement.

Further practical importance of this paper is that the use of a multi tine implement, with the tines vibrating out of phase, can be used to minimize the vibration transfer to the tractor and operator.

Similar behavior was observed by Bandalan *et al.* (1999) where an increase in draft reduction occurs as the velocity ratio increases, and the accompanying increase in the power requirement was also observed. This study also showed that a larger amplitude lower frequency vibration resulted in a higher draft reduction and lower power consumption.

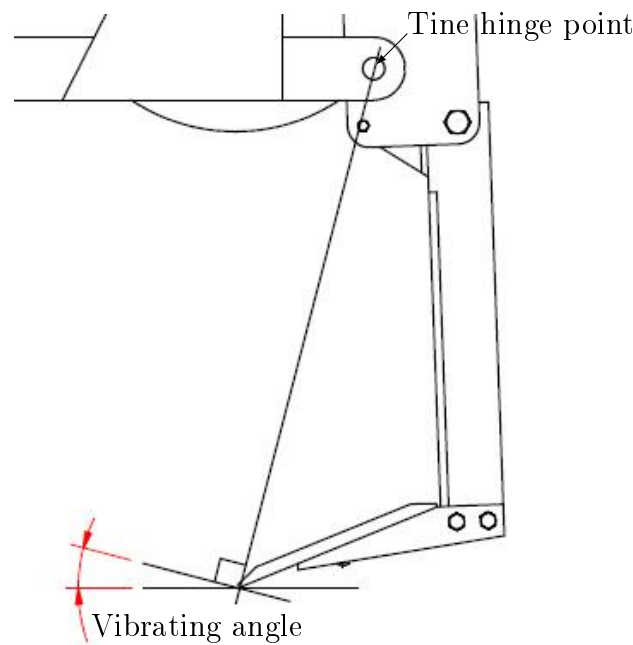


**Figure 2.1.1:** Vibrating angle

Bandalan *et al.* (1999) tested a single tine subsoiler for the braking of hard pan in sugarcane fields. They tested at various frequencies, amplitudes and ground speed to determine an optimum set of parameters. The optimum set was an amplitude of 36,5 mm, 9,48 Hz frequency and a velocity ratio of 3,55. The resultant draft reduction was 67 % (draft ratio of 0,33) with a 24 % increase in power requirement (power ratio of 1,24) .

This paper demonstrates that the vibratory subsoiler allowed a small light weight tractor to do deep soil tillage. In addition the use of the lighter tractor further reduced soil compaction.

Szabo *et al.* (1998) illustrated the effect of soil parameters on a laboratory experimental setup of a vibrating bulldozer blade, chisel and moldboard plough. The tests were conducted over a range of frequencies, from 10 Hz to 70 Hz, and amplitudes from 1 mm to 2,5 mm resulting in velocity ratios between 17 and 49. The draft reduction during these test were as high as 90 % for the vibratory chisel plough.

It was observed that an increase in clay and silt content, bulk density or particle density, increases the draft reduction. A decrease in soil cohesion will also increase the draft reduction. Further more, for cohesive soils, a reduction in moisture content increased draft reduction and for non-cohesive soils the draft reduction increases with an increase in moisture content.

A theory on why vibration reduces the draft force, brings across another impor-

tant aspect of this paper. For dry soils the vibrating tool fractures the soil therefore reducing the cohesiveness. For wet soils stress pulses are transmitted through the soil resulting in burst of hydrodynamic pressures and excess pore water pressure, which reduces the effective stress and thereby the soil strength.

Shahgoli *et al.* (2006) introduced the tine shape as a variable. Straight and bend subsoiler tines were tested to determine the effect of the bent tines on the vibratory subsoiler. The draft reduction for the two tines were very similar, 68 % for the straight tine and 61 % for the bent tine, both at 8,8 Hz, a 67 mm amplitude and a velocity ratio of 4,4. The bent tine, however, loosened a 20,5 % larger cross sectional area of soil compared to the straight tine.

The draft reduction also increased with an increase in frequency. For most frequencies tested at the overall power ratio was below one. The best power requirement reduction was 26,3 % (power ratio of 0,737) for the straight tine at a frequency of 4,3 Hz (2,2 velocity ratio).

### Soil manipulation

Niyamapa and Salokhe (1993) did a study on the soil failure caused by a vibratory implement. They did experiments in a soil bin with sandy loam soil at various frequencies, amplitudes and forward speeds. It was observed that the soil fails in a brittle manner, with radial and transverse cracks in the crescent shaped failure zone. The soil disturbance was more with vibration than without it. The disturbance also increased with higher frequencies. The failure zone was divided in two main zones namely, the deep layer zone and the near surface zone. The deep layer zone showed that the soil fractured into small fragments, while the near surface zone broke into bigger clots.

This particular study highlighted another benefit of vibrating tillage: the increased soil pulverization due to the vibration. Reason being: as the velocity ratio increases, the tool moves faster relative to the constant forward speed and therefore spends more time working in failed soil, thus pulverizing it more.

Szabo *et al.* (1998) also stated that the vibrating tool improves soil brake up and reduces clot sizes. They observed that with an increase in frequency the soil brake up is improved due to increased soil separation.

Niyamapa and Salokhe (2000a) studied the pressure distribution under a vibrating tillage tool. They tested an oscillating tillage tool in a laboratory soil bin at various frequencies, amplitudes and forward speeds. Their results showed a reduction in horizontal as well as vertical force with increasing frequency and amplitude. The peak pressure tends to be higher at larger frequency, amplitude and ground speed which could be due to acceleration forces of soil on the blade. Their results also showed that the average normal soil pressure was higher for non-vibrating cases than for vibrating cases.

Niyamapa and Salokhe (2000*b*) also studied the effect of vibration on soil pulverization with the aid of a vibrating winged subsoiler. During vibration soil cracks were evident on the surface due to lifting of soil clots. During non-vibration tests no cracks were evident and the soil showed signs of flow. Dry bulk density also tended to diminish with increasing frequency. The reduction in bulk density was less for higher amplitudes than for lower amplitudes.

They reported that the lower draft force at high velocities during vibration is due to the rate of increasing pore pressure when stress is applied at a very high loading velocity. Greater pore pressure reduces the effective stress. Non-vibration is also seen as continuous application of load whereas vibration is seen as impact loading.

Slattery and Desbiolles (2003) tested different deep tillage techniques for vineyards with a two tine subsoiler. These methods were compared on the basis of area of soil loosened, power and fuel demand and on the basis of Soil Loosening Energy (SLE). They defined the parameter SLE as the area under the cone index vs. depth curve for a given depth, multiplied by the area of the loosened soil profile to that same depth. The cone index is the pressure required to force a cone penetrometer into the soil.

The vibrating tests were done with a 30° vibration angle, 45 mm amplitude and a velocity ratio of 2. They achieved a soil loosened area increase of between 17% and 40%, working depth increase of 16% and a SLE increase of between 35% and 69%. The optimum setting however, was a horizontal tine angle and an amplitude of 70 mm. At this setting the loosened area was increased by 65% and the SLE increased by 138%. The working depth was also increased by 35%. This setting however, caused severe tractor vibration and operator discomfort, therefore only one test run was done at this setting.

Their results showed that the vibrating tines required more engine power and fuel, nevertheless an increased working depth and loosened area was achieved. The increase in SLE suggested that more of the engine power is transferred directly to the soil, thus a greater efficiency in soil loosening is achieved.

### **Concluding remarks**

From the papers presented in this chapter, it is clear that by vibrating a tillage tool, the draft force can be significantly reduced. In most cases this coincides with an increase in power requirement, however there are numerous benefits of reducing the draft force. As it has been established, the reduction in draft force allows for smaller lighter tractors to do deep soil tillage, which in turn reduces further soil compaction and allow small vineyard tractors to do deep tillage in confined spaces.

Further benefits of the vibratory tillage tool include the ability to increase the soil brake up. This in turn produces a finer tilth and eases secondary tillage op-

erations or even eliminates the need for secondary tillage. A vibrating tillage tool also increases the area loosened by a single tine, thus increasing its soil loosening efficiency.

This chapter also shows that different researchers used different frequencies, amplitudes and forward speed. Thus, there is no definite optimum combination of operating parameters for these implements. It is thus necessary to do further research into the optimization of such a tool in terms of the draft reduction and power requirement.

The effects of the different operating parameters mentioned in this chapter will be used in Chapter 7 to evaluate the simulation model, and the behavior observed during the simulations.

### 2.1.2 Mathematical Models

Kofoed (1969) derived a mathematical model for the power requirement prediction of a vibrating implement. This model was based on the kinematics of a vibrating tine and was a generic model in the sense that it could be used for a tool vibrating in any direction. This model, however, did not incorporate the working depth, soil conditions or tool shape and size in the calculation. Thus, it is not able to give absolute values of the forces or power requirements and cannot be used to study the effect of these parameters on the performance of the tool.

This model was able to model the effects of vibrating direction. It was concluded that a tool vibrating in the direction of forward motion is more effective than for a vertical or sideways vibrating tool.

Smith *et al.* (1972*a*) developed a mathematical model for a vibratory tillage tool to study the effect of vibrating wave forms. The wave forms studied were a simple harmonic, sawtooth and modified square wave. This study was also compared to the experimental data obtained from their laboratory model (Smith *et al.*, 1972*b*).

The mathematical model predicted the draft and power ratios by incorporating the tool velocity, the contact ratio and two parameters that need to be determined experimentally. The contact ratio is the ratio between the time the tool is in contact with the soil during one cycle and the total cycle time. The two experimentally determined parameters would make it possible to incorporate different soil conditions and tool sizes, however an experimental setup is necessary.

The mathematical model showed that the wave form did not have an effect on the draft ratio, although the sawtooth wave did have the lowest power ratio. Compared to experimental results the mathematical model predicted the minimum expected values for the draft and power ratio. The theoretical contact ratio was inaccurate due to the relaxation and compression of the real soil.

Butson and Rackham (1981) developed a mathematical model based on the movement of the tine in the direction of forward motion. In this model the oscil-

lating cycle was divided into five regions:

1. The tool advances through soil that was failed during the previous cycle.
2. While advancing the tool elastically compresses unfailed soil.
3. The tool advances through unfailed soil (fails the soil).
4. Tool retreats, relaxing the elastically compressed soil.
5. The tool retreats through failed soil.

This model is fairly complex and involves numerical integration of equations in each of these five regions, which are then added to give the total draft and power ratios. It also incorporates three soil parameters: a dimensionless spring stiffness; the ratio of the resistance of failed soil to that of unfailed soil; and a dimensionless soil parameter. These soil parameters must be determined experimentally and can be difficult to obtain. This model was also compared to experimental data obtained from Butson and MacIntyre (1981). The draft ratio predicted by the model showed a maximum error of 20% and the power ratio a maximum error of 50%.

The models presented in the above mentioned papers cannot be used to predict tool forces or power requirement in general. The last two papers mentioned (Smith *et al.*, 1972*b*; Butson and Rackham, 1981) are very specific in terms of the experimental setups used, and incorporate parameters that need to be determined experimentally. Thus, they cannot be used to predict design parameters for tool shapes and soil conditions other than for what was respectively used in their experimental setups. These models do, however, provide some insight into the effect of different parameter. They show a decrease in draft ratio and an increase in power ratio as the velocity ratio increases. This coincides with what is generally found to be the case with vibratory tillage tools.

### 2.1.3 Numerical Simulation

Experiments are effective in obtaining results, but it is rather time consuming and expensive to build and test a vibratory implement to evaluate the influence of a number of parameters. The mathematical models can also be used to evaluate the effects of different parameters. However, they were only formulated with very specific problems in mind and therefore do not take into account the different tool shapes, working depths and soil properties (without the need for an experimental setup).

Numerical simulation models, on the other hand, can be more flexible. They can incorporate different soil and tool properties, as well as different operating



parameters. An almost infinite number of frequencies, amplitudes, forward speeds, tool shapes and even soil conditions can be modeled without the capital expenditure of a real implement.

Tanaka *et al.* (2005) modeled a vibratory subsoiler with the Discrete Element Method (DEM) and illustrated the flexibility and usefulness of this method. They created a two dimensional model of a vibratory subsoiler consisting of two curved tines either side of a single straight tine, which vibrated in a vertical plane. The subsoiler was modeled in its width so that the forward motion was in the depth of the model. Only the effect of the vibrating frequency and the angle of the curved tines, on the failure zone was studied.

The model consisted of 13 267 discrete elements with specific material properties as well as bonds between the particle to allow tensile forces between particles (thus simulating cohesive soil). The material properties were calibrated by comparing the failure surfaces obtained from the simulations to those obtained in the experimental work. The failure criteria of the bonds between the particles were adjusted until the right failure surface was obtained.

The effectiveness of the subsoiler was expressed in terms of the amount of bonds broken between the particles during vibration. The energy efficiency of the subsoiler was also evaluated in terms of the number of bonds broken per unit energy. These parameters were evaluated at different frequencies and different tine angles. The evaluation pointed out that an increase in frequency and tine angle, increases the number of broken bonds.

Tanaka *et al.* (2005) illustrates the ability of a numerical model, more specifically a DEM model, to simulate a vibratory subsoiler. It is more flexible than the mathematical models, as it can simulate the effects of different parameters. Numerical models can also be used to study the effect of parameters on different aspects such as draft force, power and even on the soil behavior. This paper specifically illustrates the ability of DEM to model the failure zone created by the tine.

This thesis takes Tanaka *et al.* (2005)'s simulation further by doing a three dimensional modelling of a subsoiler under different conditions. The combinations of amplitude and frequency are investigated as well as the effect of the vibration on the soil and failure surface. The calibration method used by Tanaka *et al.* (2005), however, is insufficient to calibrate the appropriate material parameters, therefore different calibrating techniques will be used.

## 2.2 Tillage Tool Design and Modeling

The ability to predict the draft and vertical forces exerted on a tillage tool as well as the soil manipulation caused by the tool, is essential in the design of tillage

implements. This will allow for a more optimum design of the tool together with its frame, as well as the ability to predict if the tool has the desired soil manipulation effect, before costly prototypes are built and tested. It will also reduce the number of prototypes needed for a trial and error empirical approach.

### 2.2.1 Mathematical Models

The first force prediction model was a two dimensional model with a straight failure surface developed by Coulomb, when he introduced what is known as Coulomb's law of soil friction and cohesion in 1776. This changed to the Mohr-Coulomb failure criteria in 1914 when Mohr introduced what is known today as the Mohr Circle (McKyes, 1985).

Sokolovski (1954) used the Mohr-Coulomb failure criteria in the development of the theory of plasticity. The theory of plasticity, or method of stress characteristics as it is also known, was used to define a failure zone in front of an inclined blade. This failure zone, which is two dimensional, consists of a straight line and a logarithmic spiral. It was the first failure zone that represented reality, but the mathematics is rather complex and can only be solved numerically.

Various three dimensional soil-tool models were developed which included models for wide tines or blades ( $d/w < 0.5$ ), narrow tines ( $1 < d/w < 6$ ) and very narrow tines ( $d/w > 6$ ). Where  $d/w$  is the depth to width ratio, or the aspect ratio. A good overview of some of these models is given by Godwin and O'Dogherty (2006) and Shen and Kushwaha (1998).

These models give some insight into how soil fails due to its interaction with a tillage tool. Wide tines cause the soil to fail in an upward and forward manner with very little sideways failure (almost a two dimensional failure). Narrow tine causes the soil to fail in a completely three dimensional manner with forward, upward and lateral failure (McKyes and Ali, 1977). The failure zone of a very narrow tine is divided into two sections. The section above, what is known as the critical depth, fails as with the narrow tines, and the section below the critical depth fails only laterally in a two dimensional manner (Godwin and Spoor, 1977).

Also given in Godwin and O'Dogherty (2006) is a model on multi tine arrangements and force prediction models for discs and moldboard ploughs, which is not applicable for this study.

Godwin (2006) is another paper of interest and discusses the effects of tool geometry on the soil failure and tool forces. Failure patterns similar to those mentioned above are described here with the inclusion of the effect of tines with wings. Although winged tines cause the draft force to increase; the soil loosening efficiency is increased. What this means is that the draft force per unit area of soil loosened is reduced. Other aspects discussed in this paper are the effect of tine depth, width, rake angle and the effect of speed on the draft and vertical

forces. What is of interest here is that the vertical forces on the tine change from downwards to upward when the rake angle increases beyond  $67,5^\circ$ , and depending on the tine geometry, there is a critical speed which below draft force is unaffected by speed.

All these analytical force prediction models were developed from experimental observations and simplification and thus do predict forces accurately. They were only developed for symmetrical, straight, flat tools and most of them do not include the effect of tool velocity. Although, they give valuable insight into tool behavior and soil failure patterns for simple tools, they cannot be used for the design and analysis of different tool geometries and tool movement such as vibratory implements.

### 2.2.2 Finite Element Method (FEM)

The Finite Element Method (FEM) is also a useful tool when it comes to tillage tool modeling. Various papers have contributed to this subject to illustrate the abilities of FEM to model the soil-tool interaction. These papers also uncovered the limitations of FEM in this application.

Chi and Kushwaha (1991) modeled a flat blade and a triangular blade with three-dimensional finite element model. The draft and vertical forces calculated with the FEM model was relatively accurate compared to experimental results. The FEM model also made it possible to determine the stress distribution on the tillage tools which was used for wear analysis. One of the assumptions that the model was based on, illustrating the limitation of FEM, was the small displacement assumption. The maximum displacement in this FEM model was only 16 mm. It also did not model the soil behavior.

The model by Mouazen and Nemenyi (1999) also showed a good correlation to the experimental results with a over prediction of between 11,76% and 20,04%. Soil distortion was also modeled relatively accurately however the model was also based on the small displacement assumption. The maximum displacement was about 100 mm, which is short compared to the tillage tool length of 500 mm.

Fielke (1999) studied the effect of cutting edge geometry of the tillage tool with two-dimensional FEM. The results on draft and lift forces showed qualitative correlation with experimental results but in most cases over predicted the values. Small displacements were used (maximum 40 mm) but gap elements were introduced between the tool and soil to represent the friction and adhesion forces.

Abo-Elnor *et al.* (2004) simulated soil-blade interaction with the aid of a three-dimensional FEM model, specifically to study the effect of mesh density and blade width. What differentiates this study from the those previously mentioned is that

they used predefined failure surfaces. This allowed for larger displacements and showed more realistic soil distortion patterns.

The above mentioned papers illustrated that FEM cannot model large displacements involved in soil tillage, this is due to the element distortion limit (Abo-Elnor *et al.*, 2004). If larger displacement is to be modelled, remeshing is required, which can be problematic in cases where history dependence is involved (Coetzee, 2000).

FEM is a continuum method that treats the material as a homogenous media and can thus not incorporate the inhomogeneity of the soil or model the complex fracture patterns (Coetzee, 2000). FEM is also not capable of simulating the soil behavior and flow patterns, which are specifically required for the current study.

### 2.2.3 Discrete Element Method (DEM)

As mentioned before, the only paper found on the DEM simulation of a tillage tool is that of Tanaka *et al.* (2005), however other soil cutting machines have been successfully simulated with DEM.

Momozu *et al.* (2003) simulated a pendulum type blade cutting a block of soil. The objective here was to modify a standard DEM simulation by using bonding forces between the simulation particles to represent the cohesion of real soil (contact bonds, section A.7.3). The simulation was validated experimentally and it was found that the simulations showed similar soil failure as the experiments. Energy comparisons were also made and it was found that the simulation showed similar energy consumption to the experimental setup. Thus the modified DEM model was able to simulate the dynamic behavior of soil in appearance and in terms of energy consumption.

Zhang and Li (2006) took it a step further and used parallel bonds (section A.7.3) in a two dimensional simulation of the reaction between a bulldozer blade and a cohesive soil. The parallel bonds were used to represent the capillary and dynamic viscous forces between the particles induced by water between the soil particles. The simulation showed that the soil, bonded into clumps of particles, brake up into smaller clumps and individual particles, similar to what is found with real cohesive soils.

Both these papers illustrated that DEM can be used for the dynamic simulation of cohesive soils by the use of bonding models. Providing valuable insight into the abilities of DEM and how soil cohesion can be modeled along with more complex aspects, such as the capillary forces. It will however be shown (chapter 7) that contact bonds do not represent the cohesive soil realistically, specifically referring to the material behavior of this thesis. The parallel bonds show more realistic soil

behavior; especially in its ability to show clot formation and the representation of the more brittle nature of soil.

Franco *et al.* (2005) simulated a bulldozer with two dimensional DEM and with cohesionless soil. The simulations were done at different blade angles and depths and it was found that the draft force lay within 7,24 % of the value predicted by a mathematical model by McKyes (1985). The vertical blade force was within 1,55 % of the values of the same mathematical model. The failure line of the soil could also be determined from the simulation, which also matched what was predicted by the mathematical model.

Cleary (2000) gave a good overview of some industrial applications of DEM. Among other application was the simulation of dragline buckets. DEM was used to simulate and study the effects of different aspects, such as the particle shape, density and bucket shape on the dynamics of the bucket and its filling process.

Coetzee (2000) also simulated the filling process of a dragline bucket. This was a two dimensional simulation of the filling process and was specifically done to validate the ability of DEM to model the filling and digging process of dragline buckets. Here it was shown that DEM can relatively accurately model the flow into the bucket and can be used to predict draft forces. It also made it possible to visualize the digging process and its different flow zones. The data obtained from Coetzee (2000) was later published in Coetzee *et al.* (2006)

Dymond (2006) simulated a dragline bucket in three dimensions specifically for a dragline bucket manufacturer. The aim was to use a computer model of the dragline bucket to simulate the dynamic behavior of the bucket to gain more insight into the mechanics governing its movement. This numerical model could be used to study the dynamics of the shear zone. It also gave more insight into the dragline behavior than scale model testing could. This enabled designers to design and optimize buckets for specific mining conditions.

These papers illustrated that DEM can be successfully used to simulate and visualize the flow patterns and dynamics of soil engaging machinery. They show that DEM can be used to determine the forces involved in these operations. It also illustrates the usefulness of DEM data in the design and analysis process of these machines. The next chapter will discuss the theory and implementation of DEM.

## 2.3 Concluding Remarks

In this chapter the background of vibratory tillage and tillage tool analysis were discussed.

The first section showed the effect of vibration on the draft force and soil manipulation. It was established that further research is required into vibratory tillage tools, specifically to find a optimum set of parameters and to create a computer simulation model that will aid in the analysis and optimization of such a tool.

The second section dealt with analysis methods for tillage tools. It showed the limitations of both mathematical models as well as that of FEM. It pointed out that DEM is a suitable method for the modeling and analyzing of tillage tools and more importantly the vibratory tillage tool.

# Chapter 3

## Discrete Element Modelling Theory

The Discrete Element Method (DEM) is a numerical method for modeling the bulk behaviour of granular material. The material is represented by finite sized particles which are contained within the boundaries called walls. The bulk behaviour of the material is simulated by monitoring the motion of each particle as it interacts with other particles, or with the walls, at the contact points.

There are two approaches to DEM. The first is the so called hard particle approach, or Event Driven method (ED) (Luding, 1998), where it is assumed that the particles are perfectly rigid and follow an undisturbed path until a collision occurs. In this method collisions are studied by examining the momentum transfer between particles during the collision, and the collisions are considered to be instantaneous. The ED method is mainly used for dissipative granular gasses (Luding, 2004) and is not used for densely packed assemblies such as soils.

The second approach was pioneered by Cundall and Strack (1979) and is called the soft particle approach, or Molecular Dynamics (MD). Here the collisions last a finite time period wherein particles are allowed to overlap or penetrate each other. This overlap causes repulsive forces between the particles (or particles and walls), which are proportional to the overlap. The motion of each particle is modeled by using Newton's law of motion. This method was specifically developed for dense particle assemblies and is thus the method used in this thesis.

The aim of this chapter is to give an overview of DEM and briefly describe the science behind it. It will be confined to the specifics of the Soft Particle Approach. A detail mathematical description of DEM is given in Appendix A where the working of *PFC3D* is covered in detail.

### 3.1 Calculation Cycle

The soft particle approach uses force-displacement models to calculate the contact forces between the overlapping particles and walls. Newton's second law is then used to determine the particle accelerations. The particle accelerations are then integrated to obtain the new particle positions and the new overlaps, the calculation cycle is then repeated.

In order to keep the calculation simple a few assumptions were made:

- The time step taken for each calculation is small enough so that velocities and accelerations are assumed constant over the time step.
- The deformation of each individual particle is small in comparison with the deformation of the granular assembly as a whole. Thus the deformation of the whole assembly is due to rigid body motion of the particles.
- A disturbance cannot propagate further than a single particle during one time step.
- Forces are calculated quasi-statically. Thus, stress waves can traverse the particle many times during one time step so that it does not influence the force calculation.

Particles in contact are allowed to overlap, this overlap causes a normal and tangential (or shear) force proportional to the normal ( $k_n$ ) and shear ( $k_s$ ) stiffness of the particle and the overlap distance ( $\delta$ ) according to equations (3.1.1) and (3.1.2) for the  $j$ -th contact. These contact forces can also involve a damping force ( $\bar{\mathbf{F}}_{d,j}$ ).

$$\bar{\mathbf{F}}_{n,j} = k_n \delta_{n,j} \bar{\mathbf{n}}_j + \bar{\mathbf{F}}_{d,n,j} \quad (3.1.1)$$

$$\bar{\mathbf{F}}_{s,j} = k_s \bar{\boldsymbol{\delta}}_{s,j} + \bar{\mathbf{F}}_{d,s,j} \quad (3.1.2)$$

Here the subscript  $n$  indicates the normal direction and  $s$  the shear direction. The unit normal vector of the contact is given by  $\bar{\mathbf{n}}$ .

The resultant force vector exerted on the particle are then determined by summing all the contact forces on the particle, as follows:

$$\bar{\mathbf{F}}_i = \sum_j \bar{\mathbf{F}}_{n,j} + \sum_j \bar{\mathbf{F}}_{s,j} \quad (3.1.3)$$

where  $i = 1, 2, 3, \dots$  is the particle number. The resultant moment vector exerted on the particle can be determined as follows:



$$\overline{\mathbf{M}}_i = \sum_j \left( \left[ R_i - \frac{\delta_{n,j}}{2} \right] \overline{\mathbf{n}}_j \times \overline{\mathbf{F}}_{s,j} \right) \quad (3.1.4)$$

where  $R$  is the radius of the particle and  $\left[ R_i - \frac{1}{2}\delta_{n,j} \right]$  is the distance from the particle center to the contact point, and  $i = 1, 2, 3, \dots$  is the particle number.

The resultant force and moment are used in Newton's second law to obtain the new acceleration and angular acceleration of the particle as shown in equation (3.1.5) and equation (3.1.6), respectively.

$$\ddot{\mathbf{x}}_i = \frac{\overline{\mathbf{F}}_i}{m_i} \quad (3.1.5)$$

$$\ddot{\boldsymbol{\theta}}_i = \overline{\mathbf{M}}_i (\overline{\mathbf{I}}_i)^{-1} \quad (3.1.6)$$

Here the  $i = 1, 2, 3, \dots$  indicates the particle number,  $m$  is the particle mass and  $\overline{\mathbf{I}}$  is the moment of inertia of the particle.

These acceleration can then be integrated over a time step of  $\Delta t$  to obtain new velocities, angular velocities and ultimately the linear and angular displacements during the time step. The displacements will then be used to determine the new position of the particles which is used to determine the overlap distance between particles. From here the calculation cycle is repeated.

The full three dimensional algorithm includes forces and motions in three dimensions and rotations around the three axis of cartesian coordinate system. The full algorithm is presented in Appendix A.

## 3.2 Contact Forces

The contact forces between particles, or particle and wall, are calculated with a force-displacement model. The overlap and relative tangential displacements are used along with particle stiffness parameters to calculate the contact force.

Here it is assumed that the tangential forces do not influence the normal pressure and contact area (Johnson, 1987). Due to this assumption, normal and tangential forces can be calculated separately and the total effect can then be obtained by the superposition of the forces.

The general force model is shown schematically in figure 3.2.1. It consist of a stiffness element and damping element in the normal and tangential directions as well as a friction element in the tangential direction. The discussions that follows will describe the different force models with reference to these parameters.

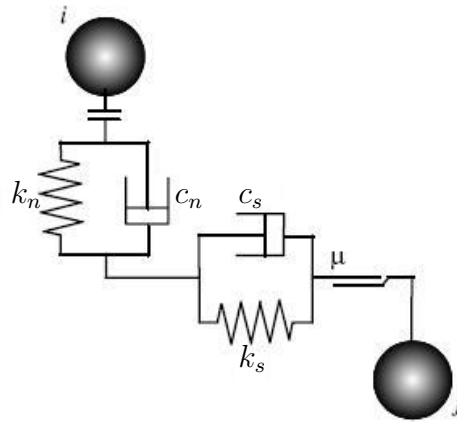


Figure 3.2.1: General force model

### 3.2.1 Normal Force Model

#### Linear spring-dashpot model

This is the simplest contact model and can be stated as follows:

$$F_n = k_n \delta + c_n \dot{\delta}_n \quad (3.2.1)$$

Here  $k_n$  is the stiffness of a linear spring with compression  $\delta$ ,  $c_n$  is the damping constant and  $\dot{\delta}_n$  is the relative velocity at the contact. The advantage of this model is that it has no free parameters and  $k_n$  and  $c_n$  can be chosen so that the material behaviour mimics that what is found experimentally (Schafer *et al.*, 1996).

This model was used by Cundall and Strack (1979) and is widely used due to its simplicity and the fact that it requires less computer resources than the other models. It is also the default contact model in *PFC3D* and will be used in this thesis.

#### Hertz theory of elastic contact

Various contact models include the Hertz theory for normal force calculation. This model only deals with contact forces and no damping is included. The Hertz theory is given in detail in Johnson (1987) and will not be repeated here.

The particle overlap derived in the Hertz theory is stated in equation (3.2.2).

$$\delta = \left( \frac{9F_n^2}{16RE^{*2}} \right)^{(1/3)} \quad (3.2.2)$$

Where  $E^*$  can be calculated by equation (3.2.3) and  $R$  can be obtained from equation (3.2.4).

$$\frac{1}{E^*} = \frac{1 - \nu_1^2}{E_1} + \frac{1 - \nu_2^2}{E_2} \quad (3.2.3)$$

Here  $E_i$  ( $i = 1, 2$ ) is the elastic modulus of the particles in contact and  $\nu_i$  is the Poisson's ratio of the particles.

$$\frac{1}{R} = \frac{1}{R_1} + \frac{1}{R_2} \quad (3.2.4)$$

Where  $R_i$  is the radius of the particles in contact.

By rearranging equation (3.2.2) an equation for the normal force is obtained in terms of a spring stiffness and the overlap. These equations are shown in equations (3.2.5) and (3.2.6).

$$F_n = \tilde{k}_n \delta^{3/2} \quad (3.2.5)$$

$$\tilde{k}_n = \frac{4}{3} E^* \sqrt{R} \quad (3.2.6)$$

The Hertz contact model is available in *PFC3D*, but it does not allow for the use of bonding models, thus it cannot be used in this thesis.

### Expansions of Hertz theory

For inelastic collisions, force theories must consist of two terms including the effect of damping. Various researchers have added different terms to the Hertz model to include damping.

Viscous damping was added to the Hertz force term in an *ad hoc* fashion to obtain:

$$F_n = \tilde{k}_n \delta^{3/2} + c_n \dot{\delta}_n \quad (3.2.7)$$

where  $c_n$  is the normal damping constant and  $\dot{\delta}$  is the relative normal velocity at the contact point. However this force leads to collisions that become more elastic as the impact velocity increases and more plastic as the impact velocity decreases (Schafer *et al.*, 1996). This is exactly opposite of what happens in practice.

Brilliantov *et al.* (1996) assumed that the material was visco-elastic and extended the Hertz Theory as follows:

$$F_n = \tilde{k}_n \delta^{3/2} + \tilde{c}_n \delta^{(1/2)} \dot{\delta}_n \quad (3.2.8)$$

Here  $\tilde{c}_n$  is a function of the material bulk viscosity. This equation gives material behaviour that agrees with experimental results, however the material viscosity is not generally available and is difficult to obtain experimentally.

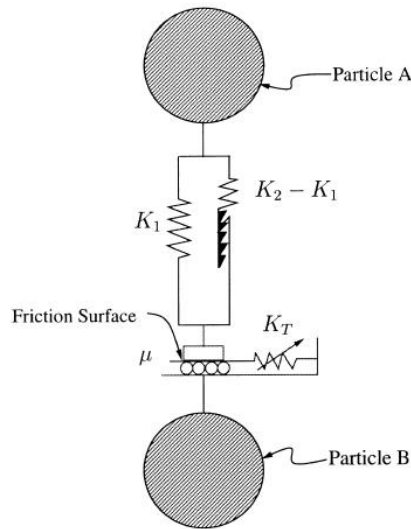


Figure 3.2.2: Walton-Braun normal force model (Vu-Quoc *et al.*, 2000)

### Walton-Braun model

Walton and Braun (1986) proposed a simple model that accounts for plastic deformation. This model used different spring constants for loading and unloading. The working of this model can be explained by looking at the partially latching spring model shown in figure 3.2.2.

During loading, or when the particles are forced together, only the one spring,  $k_1$  is active. During unloading, or when the particles move away from each other the latching system activates the other spring with stiffness  $(k_2 - k_1)$ , and the overall stiffness is  $k_2$ . This action gives rise to an expression for normal force of the form shown in equation (3.2.9).

$$F_n = \begin{cases} k_1 \delta_n & v_n \geq 0 \text{ loading,} \\ k_2 (\delta_n - \delta_{n0}) & v_n < 0 \text{ unloading.} \end{cases} \quad (3.2.9)$$

Here  $\delta_{n0}$  is the value where the unloading curve goes to zero (residual displacement), and  $\delta_n$  is the relative normal displacement. The stiffness parameters  $k_1$  and  $k_2$  represent the slope of the loading and unloading curves, respectively.

The Walton-Braun contact model is not available in *PFC3D* and also does not allow for the use of bonding models.

### 3.2.2 Tangential Force Models

Generally tangential forces are related to the normal forces via the Coulombs' law of friction. Both static and dynamic friction exists simultaneously during contact. According to the Hertz theory, during contact of two convex particles, the normal force increases from the outer part of the contact area toward the center. Thus dynamic friction occurs on the outer parts of the contact area where the forces are small, and static friction occurs towards the center of the contact area, where large forces are present. This results in an annulus where micro slip occurs around an inner region where there is no slip (surfaces stick to each other). This sticking of the surfaces can store and restore kinetic energy so that complete reversion of tangential velocity can occur in certain circumstances (Schafer *et al.*, 1996).

Various shear force models have been introduced. A very simple model just incorporates the Coulomb law of dynamic friction:

$$F_s = \mu \cdot |F_n| \cdot \text{sign}(\dot{\delta}_s) \quad (3.2.10)$$

Here  $\dot{\delta}_s$  is the tangential relative velocity,  $\mu$  is the dynamic friction coefficient and  $F_n$  is the normal force. The subscript  $s$  indicates that it is in the tangential (or shear) direction. This model can only slow the tangential velocity to zero and can not cause a reversal of tangential velocity. It is also discontinuous when the tangential velocity is zero and suggests that there is no shear force when there is no relative tangential velocity.

Another simple model is where viscous friction is used.

$$F_s = c_s \dot{\delta}_s \quad (3.2.11)$$

Where  $c_s$  is the shear damping constant which has no physical interpretation. This model also does not provide for the reversal of tangential velocity and gives results that are not physically possible when nearly normal and nearly grazing impact occurs. To this end, the case where pure rolling occurs (no relative tangential velocity) is never reached, and since it is independent of the normal force it does not vanish during grazing contact (Schafer *et al.*, 1996).

A combination of these two models can get rid of the discontinuity in the first case but still does not account for tangential elasticity. Another disadvantage of these models is that it is unstable for static and quasi-static cases.

#### Cundall and Strack model

Cundall and Strack (1979) introduced tangential elasticity into the shear force model. First they integrate the relative tangential velocity with respect to time to obtain the incremental relative tangential displacement,  $\Delta s$ , for the specific time step. This incremental displacement is then used in the force displacement law

to calculate the shear force. This force law take the form of a spring constant multiplied with the incremental displacement to give an incremental force and is stated as follows:

$$\Delta F_s = k_s \Delta s \quad (3.2.12)$$

To get the total force exerted on the particles, this incremental force is added to the sum of the force increments of the previous time steps:

$$(F_s)_t = (F_s)_{t-\Delta t} + \Delta F_s \quad (3.2.13)$$

The subscript  $t$  just points to the current time step and  $t - \Delta t$  to the previous time step.

This total shear force is tested against a maximum possible value determined by a Coulomb-type friction law.

$$(F_s)_{max} = F_n \mu + c \quad (3.2.14)$$

where  $\mu$  is the smaller of the interparticle friction coefficients of the two particles in contact, and  $c$  is the smaller of the cohesions. If the absolute value of the shear force is found to be larger than the possible maximum it is set equal to this maximum.

The Cundall and Strack tangential force model is used in *PFC3D* along with the linear normal contact model.

### Walton-Braun model

Walton and Braun (1986) introduced a simplified version of the Mindlin and Deresiewicz (1953) contact theory for the tangential forces. This is also an incremental model, as with the Cundall and Strack (1979) model. This model, however, does account for plastic deformation by reducing the tangential stiffness when plastic deformation occurs.

The Walton-Braun model is not available in *PFC3D* and will thus not be discussed in detail.

### 3.2.3 Bonding Models

For the modeling of cohesive materials, bonding models can be used. This allows tensile forces to occur between particles. For the software used in this Thesis, *PFC3D*, there are two available bonding models: contact bonds and parallel bonds.

The contact bonds can be seen as a pair of elastic springs at the contact point, one working in the normal and the other in the shear direction. The normal strength of the contact bond allows tensile forces to be exerted between particles when they

separate. If the normal or shear strength is exceeded the bond breaks and is deleted, the contact force is then set to zero. The bond stiffness is the stiffness assigned to the particles involved. Contact bonds can only exert tensile normal forces and tangential forces between particles.

Parallel bonds can exert normal and tangential forces as well as moments between particles. They can be seen as a set of elastic springs distributed over a specified circular area in the contact plane. Parallel bonds must be assigned normal and shear stiffness and strength, which allows them to model more complex particle interaction than the contact bonds. When the bond strength (normal or shear) is exceeded the bonds break and are deleted.

The effects of these two bonding models on the simulation results and material behaviour are discussed in Chapter 7. More detail on the bonding models are given in Appendix A.

### 3.3 Numerical Methods

The numerical methods used in DEM are time step integration methods to integrate the equation of motion of the particles to obtain a new velocity and displacement of the particles.

DEM is in general a time consuming method due the requirement of a small time step, where the computation time increases as the number of particles increase. It is thus highly desirable to employ an efficient contact detection and integration algorithm.

Integration of the equation of motion can be done by various numerical methods, such as Euler's method or Runge-Kutta, just to name a few. Although these methods are widely used in general dynamic analysis, the finite difference methods is preferred in DEM.

The leap-frog scheme is a very basic step-by-step integration procedure that is employed by Cundall and Strack (1979) and Vu-Quoc *et al.* (2000). This method is based on the fact that the time step is taken to be so small that the disturbances cannot propagate from a particle further than its immediate neighbor. Thus the resultant forces working in a particle are only determined by the particle's interaction with the particles it is in contact with. The time step is also taken small enough that the velocity and acceleration of the particles are assumed to be constant over the time step.

The procedure is as follows: Firstly the acceleration of the particle is determined by Newton's second law as shown in equation (3.1.5) and equation (3.1.6). These accelerations are then used to calculate the velocity at the next half time step as follows:

$$\dot{x}_{i,(t+\frac{1}{2}\Delta t)} = \dot{x}_{i,(t-\frac{1}{2}\Delta t)} + \ddot{x}_{i,t}\Delta t \quad (3.3.1)$$

$$\dot{\theta}_{i,(t+\frac{1}{2}\Delta t)} = \dot{\theta}_{i,(t-\frac{1}{2}\Delta t)} + \ddot{\theta}_{i,t}\Delta t \quad (3.3.2)$$

Here the subscript  $(t + \frac{1}{2}\Delta t)$  indicate the velocities at the next half time step. The subscript  $(t - \frac{1}{2}\Delta t)$  indicate the velocities at the previous half time step. These velocities can be used to calculate the new positions for the particles at the next time step:

$$x_{i,(t+\Delta t)} = x_{i,t} + \dot{x}_{i,(t+\frac{1}{2}\Delta t)}\Delta t \quad (3.3.3)$$

$$\theta_{i,(t+\Delta t)} = \theta_{i,t} + \dot{\theta}_{i,(t+\frac{1}{2}\Delta t)}\Delta t \quad (3.3.4)$$

If damping is used, the forces used to calculate the acceleration of the particles in equations (3.1.5) and (3.1.6), are dependent on the particle velocity at the current time step  $(t)$ . This velocity can be determined for the next time step  $(t + \Delta t)$  by extrapolation as follows:

$$\dot{x}_{i,(t+\Delta t)} = \frac{3}{2}\dot{x}_{i,(t+\frac{1}{2}\Delta t)} - \frac{1}{2}\dot{x}_{i,(t-\frac{1}{2}\Delta t)} \quad (3.3.5)$$

### 3.4 DEM Software

There are only a few commercially available software packages that incorporates Discrete Element Methods. The reason for this is that DEM is a computationally expensive algorithm and recent advances in computer technology has made the use of the DEM algorithms more practical than before.

The DEM software that is commercially available include *PFC2D* and *PFC3D* from Itasca and *EDEM* which is distributed by Msc.Software. *EDEM*, however, is not as versatile as *PFC* and is not available for the current study, thus *PFC3D* will be used for this project.

*PFC3D* (Particle Flow Code in three dimensions) is a discontinuum code that is used for discrete element modeling especially where large strain and fractures occur. It was not designed for a specific problem and is thus very flexible and versatile, and can be used to model any dynamic particulate system. *PFC3D* can also be used to analyze solid objects with specified boundary and initial conditions. This can be done by approximating the system as a compacted assembly of small particles.

The solution algorithms are based on the soft particle approach under the assumptions listed in table 3.4.1, and various contact models are build into the software. The main contact models available are the linear contact model and the



**Table 3.4.1:** *PFC3D* Assumptions

---

<ol style="list-style-type: none"> <li>1. The particles are treated as rigid bodies.</li> <li>2. The contacts occur over a vanishingly small area (i.e., at a point).</li> <li>3. Behaviour at the contacts uses a soft-contact approach wherein the rigid particles are allowed to overlap one another at contact points.</li> <li>4. The magnitude of the overlap is related to the contact force via the force-displacement law, and all overlaps are small in relation to particle sizes.</li> <li>5. Bonds can exist at contacts between particles.</li> <li>6. All particles are spherical; however, the clump logic supports the creation of super-particles of arbitrary shape. Each clump consists of a set of overlapping particles that acts as a rigid body with a deformable boundary.</li> </ol>
--

---

Hetz-Mindlin contact models. The linear contact model is similar to what was described in section 3.2.1 for the normal direction and for the shear direction, it is similar to the Cundall and Strack model as described in section 3.2.2. The Hetz-Mindlin contact model is based on the Hertz contact theory for the normal direction and a simplified version of the Mindlin and Deresiewicz (1953) tangential contact model.

The *PFC3D* model consists of spherical particles called 'balls', that are assumed to be rigid with a vanishing contact area (i.e. a contact point). The particles are usually contained by boundaries called 'walls'. The walls allow the user to contain the balls in a specified geometry or apply initial conditions and boundary conditions. The particles only interact with each other and the walls at the contact point, where they are allowed to overlap for force calculation as described in previous sections. Newton's second law dictates the motion of the particles.

Non-spherical particles can also be created by using clumps of spheres with bonding between them at the contact. This bonding allows the analysis of more complex behaviour such as cohesion effects between particles.

Two types of bonding models are available in *PFC3D*: contact-bonds and parallel-bonds. Both can be visualized as a kind of glue joining two particles in contact. The contact-bond glue is of vanishingly small size, and only works in on the contact point, where as the parallel-bond glue is of finite size and acts over a circular cross-section between the particles.

More detail of *PFC3D* are given in Appendix A. Here the calculation cycle, contact, damping and bonding models as well as contact detection are discussed in detail.

### 3.5 Concluding Remarks

This chapter presented the basic working of DEM, including different contact models that are used in DEM. Most of these contact models are however computationally expensive and are not generally available in commercial DEM code. Most of these models also do not allow for tensile forces between the particles and can thus not be used to model cohesive material. The only models that can be used along with bonding models are the simple linear contact model and the Cundall and Strack tangential contact model.

The current project requires the modelling of cohesive soil, thus bonding between particles are necessary. For this reason only the simple linear contact model and Cundall and Strack model will be used along with bonding models and damping.

# Chapter 4

## Field Tests

Field tests were done with a vibratory subsoiler in order to validate the DEM model. The subsoiler used in these tests was a single tine implement designed specifically for research purposes by Van der Linde (2005) in a previous project. The tests were conducted on a government owned farm of the Department of Agriculture at Elsenburg, where a tractor was supplied for testing purposes as well.

Soil property tests were conducted in order to determine the condition of the soil. The soil tests were conducted during the same time period as the subsoiler tests, in order to capture the soil properties at the time of testing, which would minimize the effect of the property change over time and environmental changes. The soil property tests were conducted in both a laboratory at the Civil Engineering department as well as at the Department of Soil Science (university of Stellenbosch). The data obtained from the tests were used for the material property calibration of the DEM model.

This chapter discusses the equipment and procedure that was used for the field test and soil testing. It includes a discussion on the hardware that was used and the procedures followed during the tests. The test results are also presented and a conclusion is made accordingly.

### 4.1 Test Site

The field that was available for testing was a harvested wheat field, with no after-harvest stubble cultivation done. Only minimum tillage and no-till planting was done on this field, with no deep soil tillage done since 1998. The field is situated on a slope and showed some spatial variation in the soil type and conditions. Never the less, the soil showed no variation in its depth, up to a depth of 500 mm as depicted in figure 4.1.1.



Figure 4.1.1: Depth profile of soil

## 4.2 Soil Tests

Soil samples were taken for various laboratory tests including direct shear tests, compression test, particle size analysis as well as bulk density and moisture content measurement.

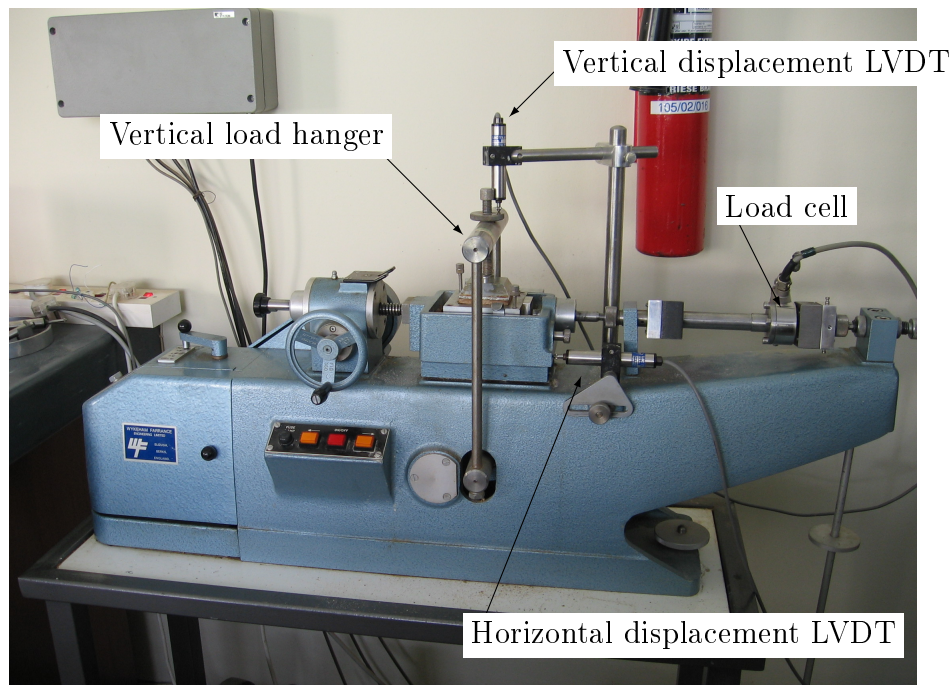
The soil was sampled from a profile hole in three layers: a top layer 0 mm to 180 mm, middle layer 180 mm to 360 mm and a bottom layer 360 mm to 500 mm. Blocks of soil were broken from the profile hole and placed in plastic bags in order to retain its moisture. Soil samples were then prepared from these blocks for the laboratory testing. The texture and brittleness of the soil made it very difficult to extract and transport the blocks and prepare the samples.

Due to time constraints, only one profile hole was made for soil analysis. The soil properties, at the position of the profile hole, are given in table 4.2.1. More details of the soil tests, including sample calculations, are given in Appendix C.

**Direct shear tests** were done with the direct shear apparatus shown in figure 4.2.1, which has a shear box area of 60 mm×60 mm. The original machine was upgraded so that data could be recorded with a Spider™ connected to a laptop computer. The original dial gauge displacement meters, for measuring horizontal and vertical displacement, were replaced with Linear Variable Differential Transducer

**Table 4.2.1:** Soil properties

Average bulk density:	1690 kg/m <sup>3</sup>
Average moisture content:	5 % weight
Internal friction angle:	35°
Cohesion:	23,6 kPa
Soil/steel friction angle:	38°
Soil/steel adhesion:	0,8 kPa
% Clay	6,15 %
% Silt	19,84 %
% Sand	68,76 %

**Figure 4.2.1:** Direct shear apparatus

(LVDT) displacement meters, and the proving ring was replaced with a load cell to measure the shear force. The LVDT's were calibrated with the aid of an Instron extension meter calibration set as described in Appendix B.

The shear tests were done on undisturbed soil samples according to the *BS 1377 – 7 : 1990* standard for dry soil above water table. Three shear tests were done for each soil layer at different normal loads. The maximum shear stress

from each test was plotted against the accompanying normal stress in order to resemble points on Mohr circles. A straight line was fitted through these points to determine the internal friction angle and cohesion. The slope of the fitted line is the internal friction angle and the intersection with the vertical axis is the cohesion. The three layers showed very similar behaviour and their average values are shown in table 4.2.1.

**The soil/steel friction coefficient** between soil and a steel surface, was determined with a similar test to the shear test. In stead of filling both halves of the shear box with soil, the bottom half was covered with a mild steel plate and only the top half filled with soil. From there on out the same test and data analysis procedure was followed as for the shear tests. The soil/metal friction angle determined here are slightly higher than the internal friction angle of the soil. However, the shear forces are lower between the soil and steel than internally in the soil, which is what is expected since the frictional forces between soil and metal are smaller than the internal frictional forces of the soil. This can be explained with regard to the small adhesion between the soil and steel (0,8 kPa) compared the cohesion of the soil (23,6 kPa).

**Compression tests** were done to determine the stiffness of the soil. The tests were conducted in the shear apparatus by using its vertical loading device and the vertical displacement meter. The load was applied in increments from zero to a maximum load and then reduced in the same increments back to zero. The displacement was recorded for each increment after it reached a steady value. This loading cycle was repeated four times and the average slope of the four loading curves (force vs. displacement) was used as the stiffness of the soil. Figure 4.2.2 shows the force vs. displacement curve for one test.

**Particle size analysis** of the soil was done with the aid of the pipette method based on what is given in Black *et al.* (1965). The soil was classified according to the US Department of Agriculture (USDA) classification system. The steps followed during the particle size analysis are discussed in detail in Appendix C. The soil classification was based on the average sand, silt and clay content across the entire depth up to 500 mm and was classified as a sandy-loam soil.

**Bulk density** of the soil was determined with the clot-method as described by Black *et al.* (1965). A soil clot is weighed in air then dipped in paraffin wax to make it waterproof. The wax covered clot is then reweighed in air and then weighed while submerged in water. The density of the soil is then determined by equation (4.2.1), which was derived from the Archimedes principle.

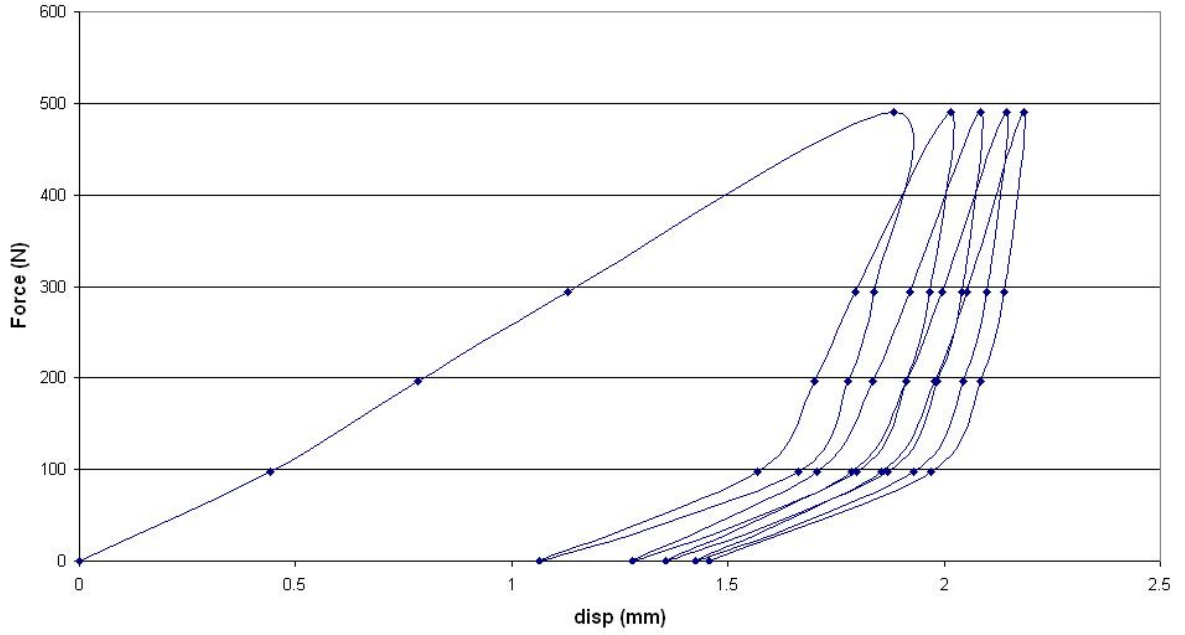


**Figure 4.2.2:** Compression test results

$$\rho_b = \frac{\rho_w m_{ods}}{m_{sa} - m_{spw} + m_{pa} - (m_{pa} \rho_w / \rho_p)} \quad (4.2.1)$$

Where  $\rho_w$  is the density of water at the temperature of determination,  $m_{ods}$  the oven dry mass of the clot,  $m_{sa}$  the net mass of the clot in air,  $m_{spw}$  the net mass of soil plus wax in water,  $m_{pa}$  the mass of wax coating in air, and  $\rho_p$  the density of wax.

If the clot was not oven dried before the test the oven dry mass can then be determined as follows:

$$m_{ods} = \frac{m_{sa}}{1 + \theta_w} \quad (4.2.2)$$

where  $\theta_w$  is the moisture content of the clot in g/g and  $m_{sa}$  is the net weight of clot in air at original moisture content.

Two samples were tested for each soil layer and the average was determined.

**Moisture content** of the soil was determined as described by Liu and Evett (2003). A clot of each soil layer was weighed and then dried in an oven at 105°C



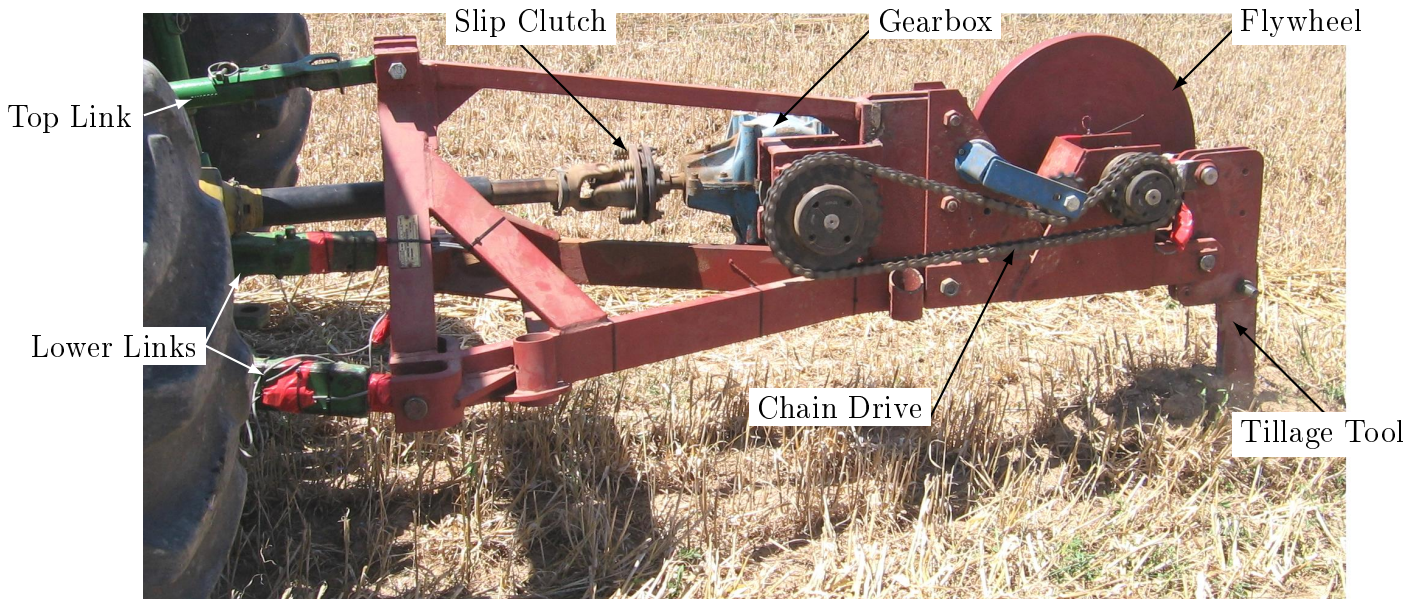


**Figure 4.3.1:** Subsoiler used for testing

until a constant weight was achieved (72 h). The clots was weighed again and the difference between the dry weight and the original weight was taken as the mass of water in the original sample.

## 4.3 Test Equipment

### 4.3.1 Subsoiler

The subsoiler used for the tests was a single tine subsoiler shown in figure 4.3.1. The tine is vibrated by a crank mechanism that is driven from the tractor PTO (Power Take Off) via a reduction gearbox (gear ratio of 19/31) and chain drive. The chain drive makes it possible to vary the vibrational frequency by using different sprocket size combinations, while the PTO speed is kept constant at 540 rpm. The sprocket combinations used and the frequencies obtained are shown in table 4.3.1.

A fly wheel is attached to the crank shaft to absorb torsional fluctuations in order to protect the drive train. The drive train is further protected from excessive torque by a slip clutch on the PTO shaft.

### 4.3.2 Measuring Equipment

Various measurements were taken during these experiments which include the draft force of the implement, the force on the connecting rod between the crank and the



**Table 4.3.1:** Sprocket combinations and vibrating frequencies

Driver gear	Driven gear	Freq (Hz)
30	19	8.71
30	13	12.7
38	13	16.1

tine, and the position of the crank. These measurement were recorded in real time during the experiments. The ground speed of the tractor and the PTO speed were also measured for control purposes. Furthermore, the soil profile measurements were done after cultivation for comparative purposes.

**Draft force** was measured by strain gauges bonded to the lower links and top link of the tractor. These measurements along with the angles of the links were used to determine the total draft force (horizontal) on the tractor. The strain gauges were bonded in a full-bridge Poisson configuration and the links were calibrated for force measurement against a load cell, by tensioning it with a mobile crane. Appendix B describes the calibration in more detail and gives the specifications and setup of the strain gauges.

**The connecting rod** force was measured in the same way as the forces on the lift linkage. The connecting rod comprises of two flat bars connected by a cross brace, thus the full bridge was split between the two flat bars to obtain the total force on the rod. This configuration also eliminated the effect of bending on the force measurement.

**The position of the crank shaft** was determined with a magnetic speed pickup. The sensor was mounted on the bearing housing of the crank shaft so that it could be exited by a metal plate mounted on the flywheel. Each time the plate passes the sensor it induces an ac voltage in the form of a sine wave with a length of one period. Each time this voltage is induced, it is an indication that the shaft is in the position where the moment arm around the crank is a maximum. A sine curve can then be fitted to this data so that the maximum amplitude coincides with the voltage pulses. The real-time measurement of the connecting rod force along with the moment arm length could then be used to calculate the torque on the crank shaft.

**Force measurements** on the linkage and connecting rod, and the speed sensor readings were recorded with the aid of a Spider<sup>TM</sup> and laptop mounted on the tractor.



**Figure 4.3.2:** Pin profile meter

The PTO speed and tractor ground speed were measured by the onboard sensors of the tractor and were only noted for control purposes.

**The soil profile** left by the tillage tool was measured with a pin profile meter. The profile meter consists of 46 rods, spaced 20 mm apart. These rods slide in-between two slotted plywood boards that are clamped together to regulate the movement of the rods; allowing the rods to slide out freely to follow the profile of the soil, or to remain in a fixed position for transportation purposes. The profile meter is shown in figure 4.3.2

These soil profile measurements were used to compare the area loosened by the tillage tool with vibration to the area loosened without vibration. These measurements were also used to evaluate the ability of the numerical model to simulate the soil disturbance effect of the tillage tool.

## 4.4 Test Specifications and Procedure

- The only parameter that was varied during the tests was the frequency of vibration. Parameters that were kept at constant values are listed in table 4.4.1 along with their values.

**Table 4.4.1:** Test parameters

Ground speed	3,2 km/h
PTO speed	540 rpm
Working depth	$\pm 300$ mm
Amplitude of vibration	30,6 mm (at the share) 7,5 mm (on crank)
Vibrating angle	16,7°
Frequency	Velocity ratio
8,71 Hz	1.85
12,7 Hz	2.69
16,1 Hz	3.41

- The ground speed was kept constant by working in a specific gear ratio at a specific engine speed. This engine speed coincided with the 540 rpm PTO speed.
- The vibrational amplitude was chosen during the design of the implement and was determined by the eccentric position of the crank.
- The depth of the implement was controlled by using the position control of the tractor linkage so that the draft control would not vary the depth due to change in soil condition. As the implement tine is situated quite far behind the hitch point, the slight play in the top link pin caused the depth to vary as the soil condition changed.
- The position of the lower links and top link were measured (by hand) at the working position to determine the angles at which the forces are exerted, in order to calculate the total draft force.
- The experiments were done over a period of several days. Before each day's tests were done, the implement was placed on stands in order to remove its weight from the tractor. The zero readings of the measuring devices were taken and all measurements were then made relative to these values.
- The procedure followed during the tests is as follows:
  1. Data recordings began with the implement in the raised position.
  2. The implement was lowered and the tractor brought up to the desired ground speed. Thus, a test run without vibration was done.

3. At the end of the run the implement was raised and recordings stopped and saved.
  4. The tractor was turned around and lined up parallel to the previous test run (a tractor-width away).
  5. Data recordings, once again, began with the implement in the raised position.
  6. This time the PTO was engaged, the implement lowered and the tractor brought up to the correct ground speed in order to perform a test run with vibration.
  7. At the end of the run the implement was again raised and the recordings stopped and saved.
- This procedure was repeated twice or three times for each frequency. By comparing the draft force measured in adjacent test runs, the effect of soil variation was minimized.
  - The soil profile measurements were made by excavating the loose soil by hand then lowering the rods of the profile meter until they touched the soil surface. The distance that they were lowered was measured from a zero reference line with a measuring tape. These values were recorded on paper and later entered into a spreadsheet to plot the profile.
  - Two samples were taken for each test run and samples for adjacent runs were taken at the same position in the length of the field. In this way the area of disturbed soil for the adjacent samples could be compared.

## 4.5 Results and Observation

### 4.5.1 Test Results

The data obtained from the experiments were analyzed in a spreadsheet. Here the calibration constants and the no-load readings were incorporated to obtain the true force values from the data. The angles of the lower and top link were also brought into the calculations to obtain the horizontal (draft) force component in each linkage.

#### **Draft force results**

To obtain the total draft force required by the tractor, the horizontal component from the top link was added to that of the lower links. Since the top link is in

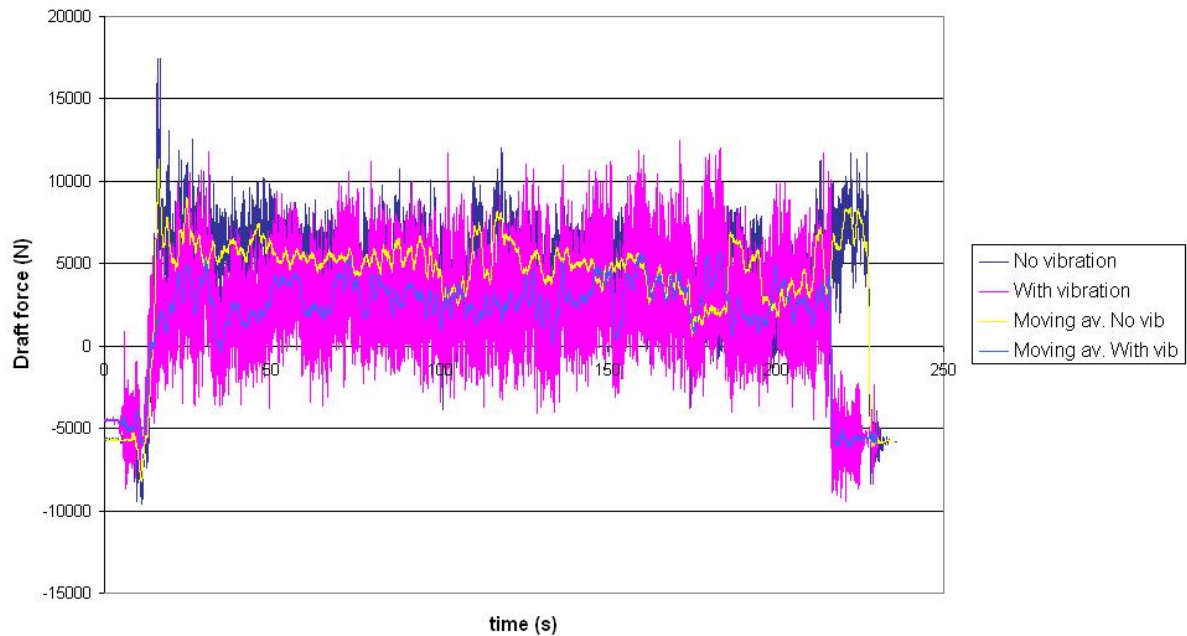


**Figure 4.5.1:** Typical test data set for 12 Hz frequency

compression (negative force) during cultivation, its horizontal force component was effectively subtracted from that of the lower links. A plot of a typical data set is shown in figure 4.5.1. This figure shows the test data from test runs with and without vibration along with their 50-point moving average.

The beginning and end of each data set shows the forces on the links when the implement is in the raised position. Since the linkage angles are different in the raised position than in the lowered position, the values of these forces are not accurate. Therefore the beginning and end of each data set was not used during the calculation of the average draft force.

To obtain the difference in the draft force with and without vibration, the average draft force during each test run (with vibration) was calculated and compared to the average draft force of the accompanying test run adjacent to it (without vibration).

The results obtained for the 16,1 Hz and 12,7 Hz frequencies are shown in table 4.5.1.

**Table 4.5.1:** Draft force test results

Frequency	Average draft reduction
12,7 Hz	66 %
16,1 Hz	50,6 %

### Torque measurements

Due to sensor malfunctions and data acquisition problems encountered during the field tests, no useable data could be obtained for the crank position. Thus no torque calculations could be made in order to determine the total power. And therefore no conclusion could be drawn regarding the overall power consumption of the tillage tool.

### Soil profile results

A typical soil profile measurement is shown in figure 4.5.2, where the profile for a non-vibrating and vibrating test run is compared. The area of the disturbed soil was calculated by means of the trapezium method and it was found that the vibration seems to increase the area of disturbed soil. The data shows an average area increase of 9 % to 13 %, however, large surface clots made it difficult to measure the profile accurately. In some cases the vibration increased the working depth, as is the case shown in figure 4.5.2.

## 4.5.2 Observation

During the tests it was observed that the test runs done without vibration broke larger surface clots than those runs done with vibration as shown in figure 4.5.3. In areas of the field where the soil was softer and easier to work, the soil surface texture for both the vibration and non-vibration test runs were similar. However, in harder areas the vibration runs produced smaller clot sizes. Although clot sizes were not physically measured, repeated observation across adjacent test runs showed that vibration reduced the clot size.

The disturbed soil also showed a profile similar to that of narrow tines that is above or at the critical depth (figure 4.5.2), as described in Godwin and O'Dogherty (2006) and Godwin (2006).

Vibration transfer to the tractor was minimal for the lower two frequencies, however for the 16,1 Hz frequency more severe vibration transfer occurred. A high degree of operator discomfort was also encountered along with a high rate of shear bolt brakeage (compared to the other tests done). In total, shear bolts broke

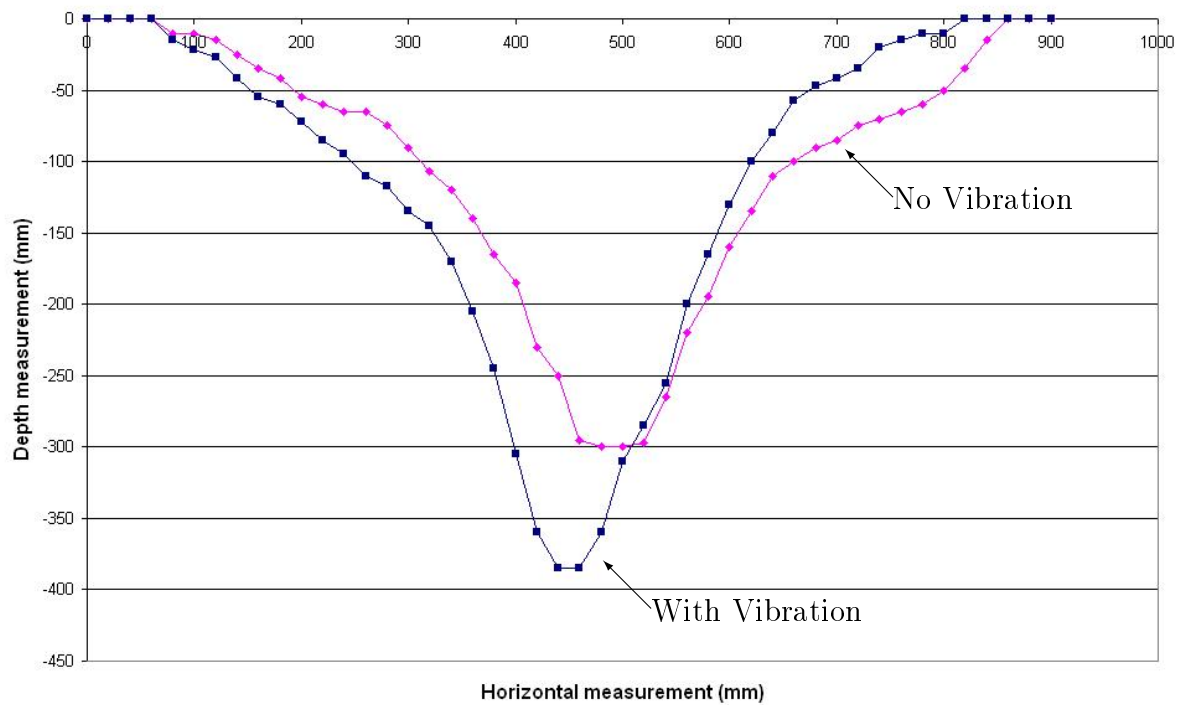


Figure 4.5.2: Typical soil profile measurement

faster during test with vibration than during tests without vibration, and broke particularly quick during the 16,1 Hz tests.

## 4.6 Conclusion and Recommendations on Experiments

### 4.6.1 Conclusion

The test results corroborate what was found in literature, by confirming that a vibratory tillage tool reduces the draft force significantly. Although the test conditions made it difficult to determine the effect of frequency on the draft force, it was clear that for the 8,71 Hz (velocity ratio 1.85) frequency tests the draft reduction was not that significant.

In observation of the soil surface after cultivation, it is clear that the vibration decreased the clot size. This re-iterates the results found by Niyamapa and Salokhe (1993) during laboratory experiments.

The vibratory tillage showed an increase in the area of the soil disturbed, and





**Figure 4.5.3:** Effect of vibration on clot size

in some cases an increased working depth. The amount of energy used per area of soil disturbed could also be reduced.

Benefits that can be derived from the reduction of draft force are:

- A lighter tractor can be used for cultivation, thus reducing the soil compaction caused by heavy tractors. The weight of the tractor can be reduced by reducing the wheel ballasting (less wheel weight and water in wheels) and thus also reducing the rolling resistance.
- The reduction in draft force also reduces the soil compaction which is caused by the traction forces between the tires and the soil.
- A reduction in draft force greatly reduces the wheel slip encountered during deep cultivation, which allows the true ground speed to be increased. This means that a greater area can be covered in a particular time, reducing the cost per area worked. A reduction in wheel slip also means less tire wear and less soil impact.
- Smaller tractors can be used for deep tillage in confined spaces such as in vineyards and orchards.



## 4.6.2 Recommendations

Further research into vibratory tillage implements is necessary. Some recommendations for further testing are:

- The torque measurement taken in these experiments was not as effective and accurate as what is required. For further testing with this machine the torque must be measured on the PTO shaft of the implement to determine true input torque, and the total power requirement.
- A redesign of the tillage tool attachment is necessary to eliminate or reduce the down time and damage caused by the frequent shear bolt breakages.
- Vibration transfer is also a major concern due to the fact that it causes severe operator discomfort and causes measuring difficulties. For the current single tine implement the vibration must be balanced or damped out in some way for further testing. For new implements the vibration can effectively be balanced out by using multiple tines vibrating out of phase.
- A further concern is the effect of the vibration on draft control devices on tractors, specifically mechanical draft control devices. This should be investigated, but the use of a multi tine implement should minimize any damaging effects.
- The effect of the vibration on the tine wear should also be investigated.
- A very important aspect that should be investigated is the affect of the vibration on the soil it self. Any negative or positive effects on the soil structure, organism life, crop yield etc. should be investigated.

# Chapter 5

## Material Property Calibration

In DEM the behaviour of particles is dependent on the micro parameters of the particles and contacts, such as the particle stiffness and friction coefficient. The micro parameters are required as input parameters, to simulate the bulk (macro) behaviour of a material.

In the case of real soil it is impossible to measure these micro parameters directly, as the real material particles are physically too small to measure these parameters. Further more, the simulation particles are not the same size and shape as the real particles due to the runtime and memory constraints of the simulation software and computers. Thus the micro parameters of the simulation particles need to be calibrated so as to give the same bulk behaviour as the real material.

Itasca (2003*b*) suggests that physical material property tests should be done on the real material and then modeled with DEM. The micro material parameters of the simulation material must then be adjusted so that the simulation material shows the same bulk material behaviour as the real material.

Physical material tests used to calibrate micro parameters include in-situ tests such as cone penetration and bar penetration tests, and laboratory tests such as direct shear, triaxial compression and confined compression tests. Asaf *et al.* (2006) used the in-situ tests for DEM micro parameter calibration whereas Franco *et al.* (2005) only used the direct shear test. These papers include calculation algorithms as part of the calibration process, however these algorithms are only applicable to cohesion-less materials without bonding between particles. Coetzee (2000) went for a more common approach and used the direct shear test as well as the confined compression test for DEM micro parameter calibration of cohesion-less materials. This procedure can also be applied to cohesive materials.

The insight obtained from literature as well as the availability of test equipment led to the decision to use direct shear tests and confined compression tests for the parameter calibration. The confined compression test was used to calibrate the particle stiffness and the shear test was used to calibrate the friction and cohesion

parameters.

The parameters that needed to be calibrated included: particle density and stiffness, particle friction coefficient, soil/metal friction coefficient and the damping or dissipation constant. Since the soil is a cohesive material and the cohesion needed to be incorporated, bonding models were used (section A.7.3), thus the contact bond strength along with the parallel bond strength and stiffness needed to be calibrated as well.

This chapter describes how the strength properties of the simulation particles were calibrated by simulating the physical material tests as described in Chapter 4. The calibration started with the density calibration since it does not depend on particle stiffness or friction coefficient. This was followed by the stiffness calibration, as it does not depend on the friction coefficient, and lastly the shear test simulations were done (identical to Coetzee, 2000).

## 5.1 Particle Size and Shape

The size of the simulation particles is limited by the computing power. The simulation time is directly proportional to the number of particles used in a particle assembly, thus it would be impossible to generate a particle assembly with the same particle size as the real soil. Particle size analysis was done on the real soil in section 4.2, where it was found that 68% of the particles sizes were between  $53\ \mu\text{m}$  and  $500\ \mu\text{m}$  with the other 32% smaller than  $53\ \mu\text{m}$ .

For reasonable simulation time with a single processor (weeks instead of months), the particle assembly size was limited to a maximum of around 100 000 particles, for the current simulation setup. This limited the particle radius to a uniform distribution between 10 mm and 15 mm, which accumulated to a total of 102 121 particles in the final simulation setup.

*PFC3D* uses spherical particles as default, however other particle shapes can be created by clusters of spheres. To minimize simulation time it was decided to use spherical particles, and since all particles are bonded together (by parallel or contact bonds, section A.7.3), the use of clumps or clusters of particles were unnecessary.

## 5.2 Particle Density

The density calibration of the simulation particles was done by measuring the mass of a specified volume of particles and adjusting the particle density until the bulk density equalled the real soil's determined density (section 4.2).

The particles were created in a square split box (the same as what was used for shear test simulation and stiffness calibration) and allowed to stabilize under the

**Table 5.2.1:** Particle densities for bulk density of 1690 kg/m<sup>3</sup>

Particle radius	Particle density kg/m <sup>3</sup>
15 mm	3000
10 mm to 15 mm	2960

force of gravity. It was then pre-compressed to 10 kPa, the pressure was released slowly and the particles allowed to stabilize. The particles above a certain height were deleted so as to leave a specified volume filled with particles.

The vertical force on the bottom wall was measured to determine the mass of the particles in the volume. By dividing the mass of the particle assembly by the volume, the bulk density could be obtained.

A loop was used to adjust the particle density until the bulk density of the particle assembly was at the required value. After every time that the particle density was altered, the particles were allowed to reach equilibrium before the mass measurement was taken.

The calibration was done for two different particle sizes: the first an assembly of homogenous particle with a radius of 15 mm, and the second a uniform distribution of particle radii between 10 mm and 15 mm. The particle densities for these particle assemblies are shown in table 5.2.1.

### 5.3 Particle Stiffness

The simulation particle stiffness was calibrated by simulating the confined compression test. The particle stiffness was adjusted until a similar gradient on the force/displacement diagram, to that found in the physical soil test (section 4.2), was obtained.

Due to the large size of the simulation particles used, the simulation model of the soil tests needed to be scaled up. The simulation model was a 10× (1:10) scale of the physical test. This ensured that at least 20 particles (in the case of the 15 mm radius) would fit in the width of the simulation box. By doing this the particle size did not influence the bulk properties of the particle assembly significantly.

The simulation box size was 600 mm long, 600 mm wide and 200 mm deep (the same box used for the shear test simulations and density calibration).

The loading force also had to be increased and was increased 100× to obtain the same applied pressure on the particle assembly as on the real soil sample. Thus the simulation forces were cycled between 0 kN and 50 kN. This allowed for a maximum

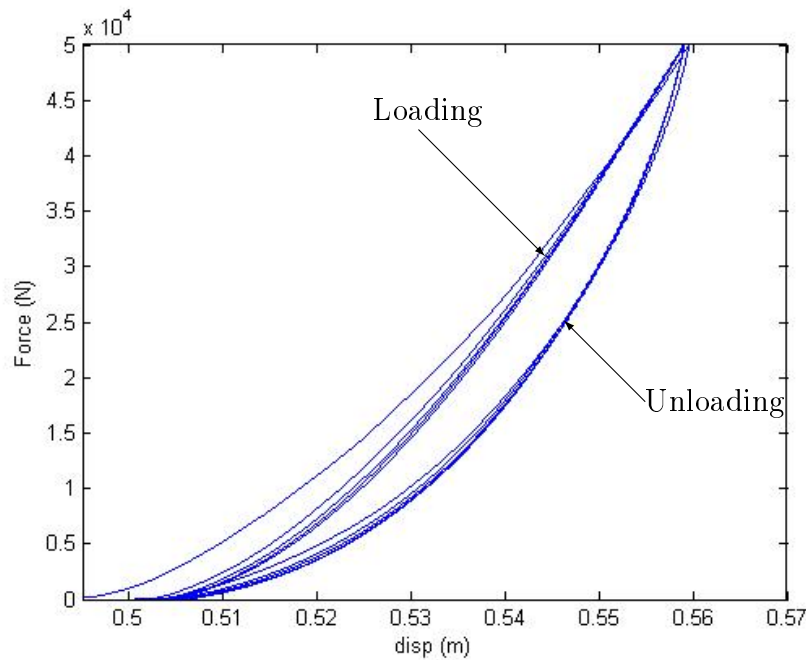


**Figure 5.3.1:** Typical force vs displacement graph for stiffness calibration

stress of 138,89 kPa compared to the maximum of 137,62 kPa used during the soil tests.

The force was increased slowly and continuously until the maximum force was reached and then it was slowly decreased back to zero. This loading cycle was repeated four times. The relevant resultant force displacement curve is shown in figure 5.3.1.

For the calibration, only the slopes of the loading part of the curve were compared to that of the curves obtained from the soil tests (section 4.2). The slope was taken as the slope of a straight line that runs through points on the loading part of the curve, coinciding with forces of 15 kN and 45 kN. For the soil test (graph shown in figure 4.2.2) the slope was determined between points coinciding with 150 N and 450 N (equal pressures).

The four slopes determined from one simulation were used to calculate an average and was compared to the average slope of the physical test. The simulation particle stiffness was changed and simulations repeated until the average slope of the curve was similar to that of the physical soil test. The particle stiffness obtained from this calibration is tabulated in table 5.3.1.

However, the particle stiffness that was determined here was not adequate to induce sufficient shear forces during shear test simulations. During these shear tests the maximum friction angle obtained was  $15^\circ$ . Any further increase in the

**Table 5.3.1:** Particle stiffness as calibrated

Particle radius	Particle stiffness N/m	Assembly stiffness N/m
15 mm	$3,7 \times 10^4$	$1,15 \times 10^6$
10 to 15 mm	$3,2 \times 10^4$	$1,16 \times 10^6$
Required stiffness		$1,12 \times 10^6$

**Table 5.3.2:** Particle stiffness used in simulations

Particle radius	Particle stiffness N/m	Assembly stiffness N/m
15 mm	$3,7 \times 10^5$	$5,69 \times 10^6$
10 to 15 mm	$3,2 \times 10^5$	$8,02 \times 10^6$

simulation particle friction coefficient had no effect on the friction angle (the required friction angle was  $35^\circ$ ). A possible explanation for this is particle distortion, which violates the assumptions that *PFC3D* is based on (table 3.4.1). In this case the simulation particle overlap could be large enough that the particles would simply move through each other without developing a large enough force to resist the externally applied load.

The maximum average contact force extracted from the simulations with the simulation particle stiffness shown in table 5.3.1 (for the 10 mm to 15 mm particle radius), was 34,24 N. If this force is divided by this stiffness, the particle overlap would be 10 % of the smallest particle radius.

To rectify this problem the particle stiffness was increased  $10\times$ . This resulted in a maximum average contact force of 82,43 N and a particle overlap of only 2,6 % of the smallest particle radius. With the increased stiffness the particle overlap (deformation) is just under 25 % of that with the calibrated stiffness.

With the increased stiffness of the simulation particles, sufficient shear forces were induced in the shear test simulations to allow for the calibration of the friction and bonding parameters.

The particle stiffness used in the simulation is tabulated in table 5.3.2.

## 5.4 Internal Friction Angle and Cohesion

The internal friction angle and cohesion of the simulation particles were calibrated by simulating direct shear tests. The model shear box consisted of a top and bottom half each 100 mm high as shown in figure 5.4.1. The motion of the lid of the top half-box was controlled so that a constant vertical force could be applied to the particle assembly throughout the simulation. The vertical forces on the particle assembly was hundred times that of the soil test, so that the same stresses could be achieved (as in the physical soil tests) for the increased box size. The vertical applied stresses used were 27,5 kPa, 55,3 kPa and 82,6 kPa, respectively.

The bottom half-box was moved at a constant velocity of 1,5 mm/s to shear the particle assembly. The velocity of the physical shear test was also scaled up ten times, however the long simulation times at this velocity resulted in the use of the velocity mentioned above, which was  $100\times$  the test velocity.

During the physical shear tests on the soil, the shear velocity needs to be slow enough to allow any pore water in saturated soil to drain. This ensures that the pore pressure due to the moisture in the soil, does not influence the shear tests results. In the simulations, however, there is no moisture that can influence the results, thus a higher shear velocity can be used without influencing the integrity of the simulation results. The shear velocity used during the simulations was still slow enough so that dynamic forces would not influence the simulation results.

The forces resulting from the shear action on the bottom half-box were measured to determine the maximum shear stress in the particle assembly. The particle friction coefficient and bond strength was adjusted to obtain a similar friction angle and cohesion to that obtained in the soil tests. In the case where parallel bonds were used, the bond stiffness was also adjusted, but the bond radius factor was kept constant. (See section A.7.3 for explanation on the bonds). The bond radius factor was kept constant to reduce the number of variables to calibrate and the effect of the bond radius was not studied. The size of the radius factor was chosen so that it would be in the middle of the range of possible sizes to ensure that the parallel bonds does not approach a contact bond (radius factor= 0) or that the bond becomes too big (radius factor= 1).

The particle properties are tabulated in table 5.4.1 for contact bonds and in table 5.4.2 for parallel bonds.

## 5.5 Soil/Metal Friction Coefficient

To determine the soil/metal friction coefficient the test done on the soil described in Chapter 4, was simulated. It was very similar to the shear test simulation, except that the bottom half of the shear box was replaced by a wall so as to form a bottom

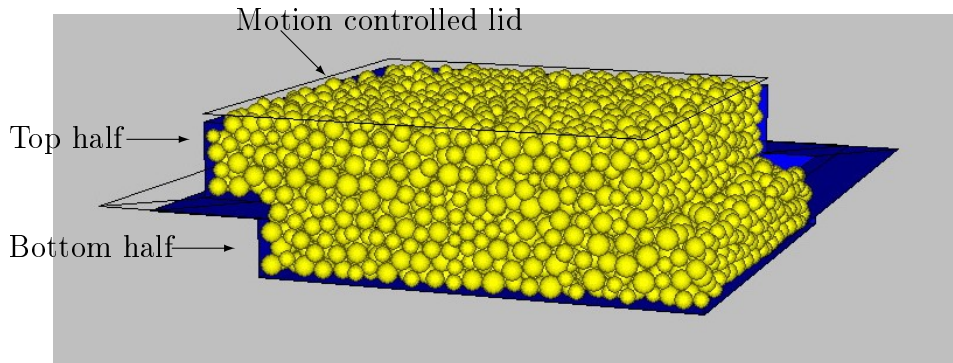


**Figure 5.4.1:** Shear box for direct shear test simulation (shown at the end of shear cycle)

**Table 5.4.1:** Particle shear test parameters: Contact bonds

Particle radius	Friction coefficient	Bond strength	
		Normal (N)	Shear (N)
15 mm	1,5	47	47
10 mm to 15 mm	1,2	35	35

**Table 5.4.2:** Particle shear test parameters: Parallel bonds

Particle radius	Friction coefficient	Bond strength Normal and Shear (Pa)	Bond Stiffness Normal and Shear (Pa/m)	Bond radius
				factor
15 mm	1,8	$115 \times 10^3$	$5 \times 10^7$	0,5
10 mm to 15 mm	1,3	$130 \times 10^3$	$5 \times 10^7$	0,5



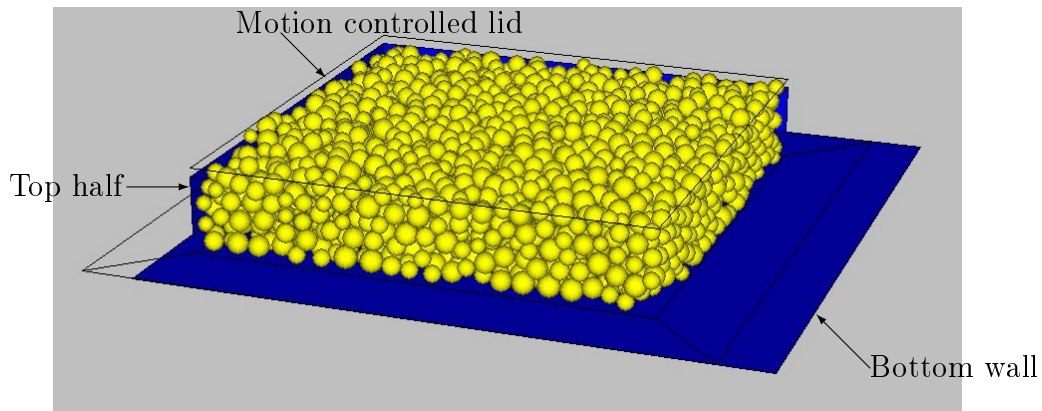


**Figure 5.5.1:** Shear box for soil/metal friction calibration (shown at the end of shear cycle)

for the top box as shown in figure 5.5.1.

In this simulation the wall friction coefficient was adjusted until the same soil/metal friction angle was obtained as in the physical test. In the simulations, however, no bonding force can exist between walls and balls, thus the soil/metal adhesion could not be calibrated. The resultant wall friction coefficient was 1,5.

## 5.6 Damping Constant

The default global damping of *PFC3D* was used to stabilize the particle assembly during the particle generation process and the subsequent simulations were done with viscous damping. Viscous damping is the only alternative damping model available in *PFC3D*.

Vu-Quoc and Zhang (1999) stated that the material stiffness is higher when the particles move away from each other than the initial stiffness, this is due to plastic deformation occurring during real contacts. The linear contact model along with the viscous damping model in *PFC3D* does not incorporate the plastic deformation and the particle stiffness stays constant. More realistic models would be that of Brilliantov *et al.* (1996) (equation 3.2.8) and Walton and Braun (1986) (equation 3.2.9), but these models are not available in *PFC3D*.

Unfortunately the damping effect of the real soil could not be tested for this project, thus the simulation damping constant could not be calibrated. A damping constant of 0,5 was chosen on the basis that it provided sufficient damping and that the calibration time was less than for a higher damping constant.

This damping constant specified in *PFC3D* is strictly speaking the critical damping ratio (see section A.6). According to Mishra (2003), the critical damping

ratio can be expressed in terms of the restitution coefficient ( $e$ ) as follows:

$$\beta(e) = \frac{-\ln(e)}{\sqrt{(\ln(e))^2 + \pi^2}} \quad (5.6.1)$$

If a restitution coefficient of  $e = 0,16$  is inserted in this equation, a critical damping ratio of 0,5 is obtained. This suggests that with a critical damping ratio of 0,5 a high degree of damping (or energy dissipation) is achieved. If  $e = 0$ , all the energy is absorbed during a collision and if  $e = 1$  no energy is absorbed. This is relevant as real soil has a high degree of damping.

## 5.7 Conclusion

The calibration methods used here were chosen to be identical to the physical tests. The shear tests and compression tests are the norm for calibrating simulation particle micro parameters and for determining material properties of real soils in practice. These tests are however, of a static nature and may not be able to capture the more dynamic behaviour and parameters of real soil, ultimately necessary for tillage simulations.

The inability to calibrate the damping constant and the incapacity to accurately calibrate the stiffness of the material, is a concern and must be addressed in future work. The particle stiffness does have a major effect on the material strength (Franco *et al.*, 2005) and needs to be calibrated more accurately. What can be deduced from section 5.3 is that the confined compression test simulation is influenced by the scaling of the simulation and of the simulation particles. The correct bulk particle assembly stiffness can be obtained, but due to the scaled up particles, the particle stiffness is not sufficient. The damping constant may also prove to have a larger effect on the subsoiler simulation results as what was observed in this project.

The calibration methods used here were found to be time consuming. Over 5600 h of processor time was required to determine the material properties (over 5200 h were spent on shear test simulations alone). This calibration time excludes the preliminary subsoiler simulations done to test the effects of the parameters. More efficient methods of calibrating DEM material properties would be beneficial for any DEM simulation.

# Chapter 6

## Simulations Setup

### 6.1 Soil Bin and Subsoiler Tine

The simulation of the vibratory subsoiler was done in *PFC3D* where the entire model was created using the build-in wall logic of the software.

The container holding the simulation particles, called a box or soil bin, is shown with its accompanying dimensions in figure 6.1.1. It comprises of six stationary walls with wall normal and shear stiffness of  $1 \times 10^8$  N/m and friction coefficient of 1. This stiffness was chosen so that the box would contain the particles throughout the simulation without the particles being forced through a wall due to large forces and/or insufficient wall stiffness. The friction coefficient was added to the wall properties to ensure stability at the boundaries.

The choice of dimensions for the box was a compromise between maximum number of particles and the 'edge effect'. If the box is too small, forces, or stresses, would propagate back and forth through the particles, bouncing off the boundaries (edge effect). This would most definitely influence the simulation results. The edge effect could be minimized by increasing the size of the box, however, this would increase the number of simulation particle to an extent that the simulation times would be impractically long. The chosen dimensions along with an adequate damping constant resulted in a good compromise between the number of particles and the size of the box.

The tine, as will be explained in the next section, was placed outside the soil bin and allowed to move into and through the bin. The length of the box was chosen so that the tine would pass through the transition period, as it moves into the bin, and still have sufficient travelling distance to reach steady state force values.

The subsoiler tine used in the simulations was a simplified version of the real tine. The general geometry and dimensions were the same, but the shear was represented by a single flat wall instead of the multi plane geometry of the real

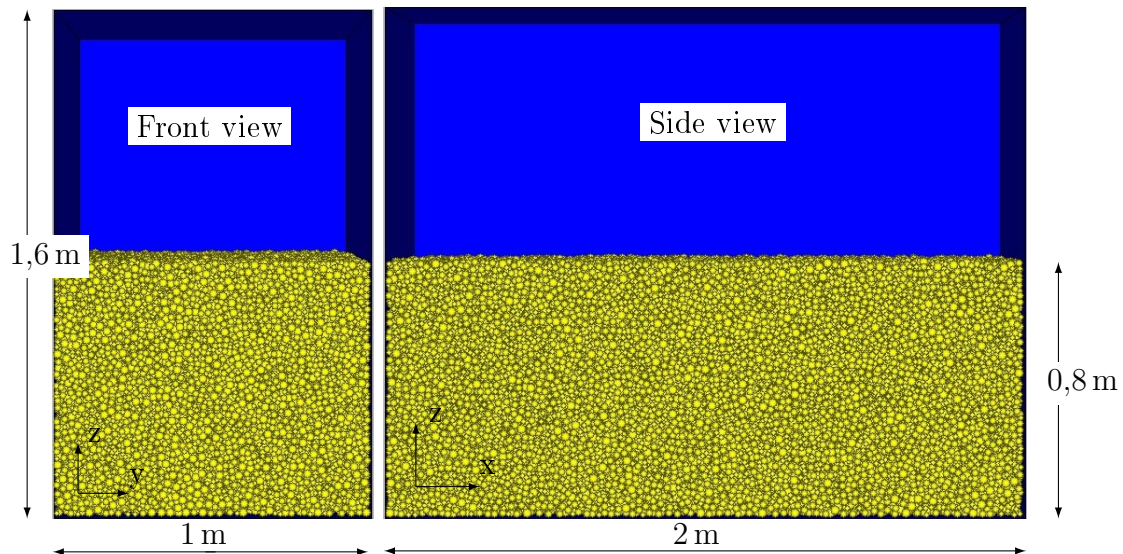


Figure 6.1.1: Soil bin dimensions

shear. Figure 6.1.2 shows the front and left view of the subsoiler tine geometry that was used in the simulation.

## 6.2 Simulation Specifics

### 6.2.1 Tine Movement

The tine movement was described by specifying the required velocity of the tine. For the non-vibratory case, the tine was given a constant translational velocity at the beginning of the simulation. For the vibratory cases the tine was given a constant translational velocity as well as an angular velocity around a point representing the pivot point of the physical tine. This angular velocity was a sinusoidal time varying function given by equation 6.2.1. It was derived from the geometry and movement of the physical subsoiler used in the experiments.

$$\Omega = A\omega \cos(\omega t) \quad (6.2.1)$$

Here  $\Omega$  is the angular velocity of the tine (rad/s),  $A$  is the amplitude of the angular displacement of the tine (rad), both around the pivot point,  $\omega$  is the frequency of vibration (rad/sec) and  $t$  is the time in seconds.

At the beginning of the simulation, the tine is placed outside the soil bin at the rear, lined up with the centre of the bin as shown in figure 6.2.1. The physical equivalent of this is a tine lowered into a hole and then moved forward into the soil. When the simulation is started the tine moves at its required velocity into the bin and continue down the centre line of the bin in the positive  $x$  direction.

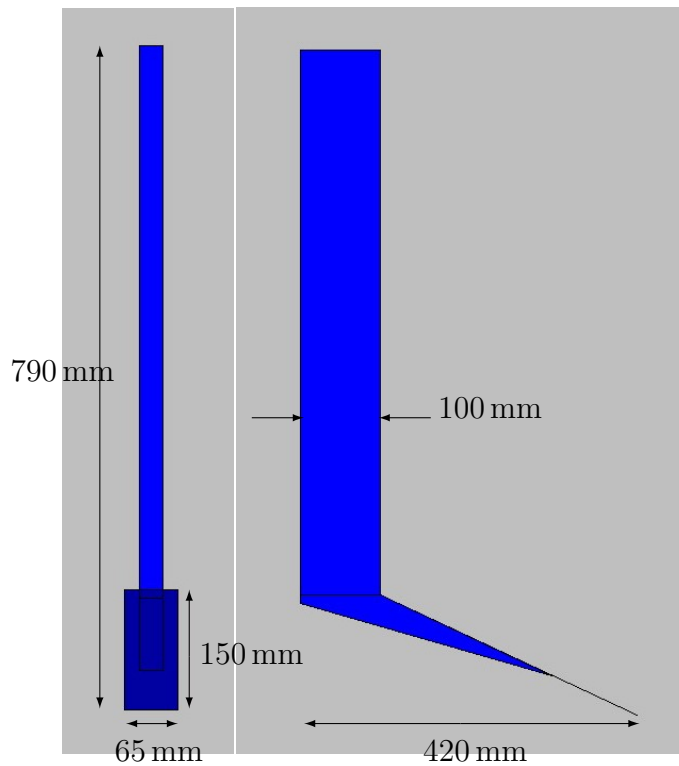


**Figure 6.1.2:** Front and left view of simulation subsoiler tine

The working depth was set at 300 mm and the constant translation speed was set at 0,889 m/s (3,2 km/h).

### 6.2.2 Parameter Extraction

Various parameters were calculated, or extracted, from the simulation. The force parameters that can be calculated directly from the contact and motion data through built in *Fish* functions include:

- horizontal tine force ( $x$  direction)
- vertical tine force ( $z$  direction)
- moment of forces on the tine about the pivot point of the tine
- work done by the tine on particles
- friction energy dissipated at the contacts
- kinetic energy of the particles

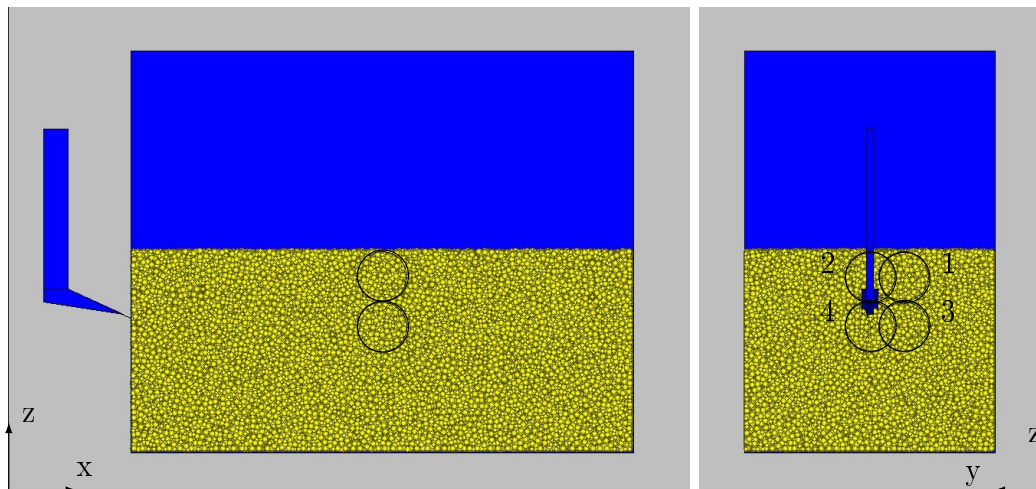


**Figure 6.2.1:** Tine at beginning of simulation and measurement sphere positions

The energy parameters were extracted to try and understand the effect of the vibration on the soil itself. To further identify the effects, the stresses and strain rates of the soil (referring to the simulation particles) were extracted at four points in the particle assembly.

Because DEM is a discontinuous, or discrete, modelling technique, stress (a continuum quantity) does not exist at each point in the particle assembly. The contact forces and particle displacements, that are monitored in DEM, cannot be directly transferred to a continuum model for stress calculation. Averaging procedures must be used to transfer the micro-scale properties (contact forces and particle movements) to a continuum model for stress calculation.

In *PFC3D* the stresses and strain rates are calculated by applying the averaging techniques to a specified volume of particles contained in a measurement sphere (Itasca, 2003a). The size and location of these spheres are specified by the user along with the parameters that must be extracted (stress, strain rate, porosity etc.).

For this simulation the stresses and strain rates were measured at four points within the particle assembly. The locations are shown as circles in figure 6.2.1. All the spheres have a diameter of 200 mm and were placed in the middle of the bin with respect to its length. The centres of spheres 1 and 2 were 100 mm below the surface and that of spheres 3 and 4 were 300 mm below the surface. Spheres 2 and 4 were placed right in front of the tine, so that the tine would effectively move through the spheres. Spheres 1 and 3 were placed 175 mm away from the middle of the bin (with respect to its width) so that the tine would not go through these spheres.

The size of the measurement sphere is a compromise. On the one side the sphere needs to contain enough particles so that an accurate average can be determined.

**Table 6.2.1:** Subsoiler operating parameters for simulations

	Run 1	Run 2
Amplitude	30 mm	40 mm
Frequencies		
@ velocity ratio 1,85	8,71 Hz	6,53 Hz
2,69	12,7 Hz	9,53 Hz
3,41	16,1 Hz	12,08 Hz
4,24	20 Hz	15 Hz
5,09	24 Hz	18 Hz

On the other had, if the sphere is too big, the averaging process will hide any stress gradients and the local stress values at the specified point will not be well represented. For the 200 mm measurement sphere diameter used here, at least 7 15 mm radius particles can fit in the diameter of the measurement sphere.

### 6.2.3 Simulation Parameters

Two sets of simulations were done: the first set, *run 1*, was done at the same amplitude and frequencies as the experimental work plus two higher frequencies. The second set, *run 2*, was done with a larger amplitude but the frequencies were reduces so as to keep the velocity ratios (equation 2.1.1) the same, as in *run 1*. *Run 2* was done to illustrate the effect of using a larger amplitude and smaller frequency at the same velocity ratio. Table 6.2.1 shows the different amplitudes and frequencies.

The simulations were run to simulate a total time of 2s, which allowed the tine to travel a sufficient distance to reach steady state force values.

# Chapter 7

## Simulation Results

During the course of the property calibration, preliminary subsoiler simulations were done to evaluate the effect of different parameters on the draft forces and material behaviour. These effects along with the final simulation results will be discussed in this chapter. Furthermore the reason why vibration reduces the draft force of the subsoiler will also be described.

### 7.1 Effect of Particle Diameter

#### 7.1.1 Effect on Draft Force

The analysis showed the following tendencies when the particle diameters were changed:

- *Contact bonds, keeping material properties constant while changing particle diameter:* The draft force increases with a reduction in particle diameter. Changing the particle radius from 20 mm to a uniform distribution between 10 mm and 20 mm increases the draft force by 66 %. Further reducing the particle radii to a distribution of between 10 mm and 15 mm further increases the draft force by 27 %. It should be noted that this last comparison was made with reduced bonds strength from the previous comparison as well as a smaller damping constant.
- *Contact bonds, material properties calibrated for particle size:* Changing the particle radius from 15 mm to a distribution between 10 mm and 15 mm, shows no change in the draft force. This shows that the calibration of the properties to give similar shear test results, allows the different particle assemblies to give the same resistance to the subsoiler. The change in particle diameter may also not be sufficient to test the effect of different particle radii.



- *Parallel bonds, keeping material properties constant while changing particle diameter:* No effect on the draft force was noted. This can be explained by the fact that the bond radius is a fraction of the smallest ball at a contact. Thus reducing the ball radius, reduces the bond radius, which in turn reduces its strength. Reducing the particle radius, increases the number of particles and thus, the number of bonds per volume, but also reduces the bond strength.

In contrast, the contact bonds maintain their strength while the density of the bonds increase and thus increase the overall soil strength.

To determine the effect of particle diameter on the draft force with parallel bonds, the properties of the different diameters particles need to be calibrated to eliminate the property variability.

- *Parallel bonds, material properties calibrated for particle size:* Reducing the particle radius from 15 mm to a distribution between 10 mm and 15 mm, shows an increase in draft force by 11 %. A further reduction in the particle diameter could increase the draft further so that it could tend towards the experimental values. However the time limitation of this project did not allow the recalibration of a smaller set of particles to study this effect further.

### 7.1.2 Effect on Material Behaviour

- *Contact bonds, keeping material properties constant while changing particle diameter:* With a reduction in particle radius the failure surface around the tine reduces in size and the material seems more cohesive and ductile. The particles seem to flow around the tine without braking their bonds. This contrasts with what is found in practice.
- *Contact bonds, material properties calibrated for particle size:* This cohesive ductile behaviour was also observed when the calibrated values were used for the different radii. There is no real difference in the material behaviour for the different particle radii.
- *Parallel bonds, keeping material properties constant while changing particle diameter:* A decrease in particle diameter decreases the size of the failure patterns. It also seem to increase the size of the clots forming on the surface which is a closer representation of what was found in the experiments (field/soil tests).
- *Parallel bonds, material properties calibrated for particle size:* Similar behaviour was observed as with the constant material properties. With a reduction in particle diameter the failure surface reduces in size and approaches

what was found in the experiments. The clot size also increases and approaches more realistic sizes.

The above mentioned behaviour observed with the parallel bonds, occurs due to an increase in bond density as the particle diameter is reduced. This allows the whole assembly to behave more like the real soil, as observed in the experiments.

### 7.1.3 Conclusion on the Effect of Particle Diameter

Changing the particle diameter has different effects on simulation results, which also depends on the bonding model and parameter changes. To simulate reality, changing the particle diameter must coincide with a change in material properties so that the same bulk material behaviour is achieved.

This is evident from what was discussed in this section with regards to the parallel bonds. The reduction in particle diameter increases the draft force so that it could tend towards the experimental results. Changing the particle diameter also influences the material behaviour. A reduction in the particle diameter resulted in a more realistic material behaviour compared to the experimental observations.

What can be seen from this section is that the particle diameter has an effect on the simulation results with regards to draft force as well as material behaviour. If the particle diameter could be reduced further the simulation results could tend towards the experimental results.

## 7.2 Effect of Bonding Models

To illustrate the effect of different bonding models, two simulation runs were compared, one with contact bonds and one with parallel bonds. Both these runs were done with the same range of particle radii (10mm to 15mm) and both sets of material properties were calibrated to give the same shear test results.

### 7.2.1 Contact Bonds

The contact bond simulation showed a 21% higher draft force than the parallel bond simulation.

There is however, a bigger difference, in the material behaviour. The contact bond simulation shows a very ductile flow type material behaviour. The particles lift up, move around the tine and drops back in the furrow left by the tine without braking the bonds. The failure pattern left by the tine is only slightly larger than the tine itself and does not represent the failure surface found in the experiments (figure 7.2.1).

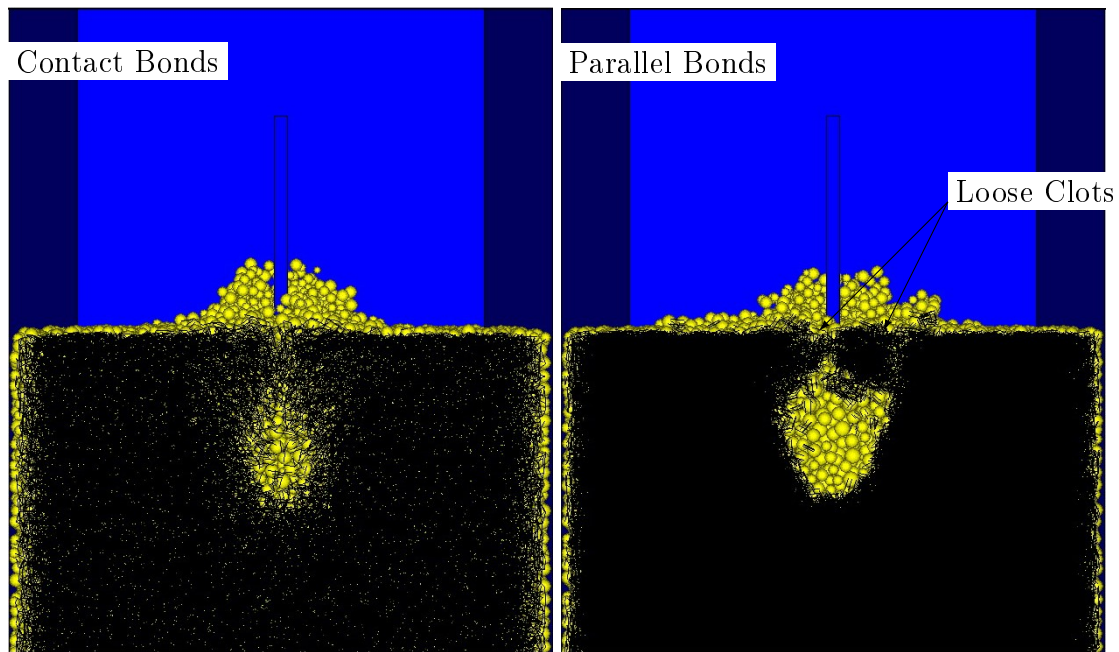


**Figure 7.2.1:** Failure surface left by tine, as seen from the rear

This happens due to the fact that one can only assign a bond strength parameter in *PFC3D*. The bond therefore has the same stiffness in tension as the particle has in compression. Thus the brittleness of the soil in tension cannot be represented with contact bonds.

## 7.2.2 Parallel Bonds

The parallel bonds are better suited to simulate the brittle behaviour of the soil. It clearly shows clot formation on the surface and a more realistic failure pattern left by the tine (figures 7.2.1 and 7.2.2). The ability of the parallel bond to model the brittle behaviour is related to its ability to assign a bond stiffness and a bond radius (in *PFC3D*). This gives the user more freedom in modelling different types of material behaviours and characteristics.

## 7.2.3 Conclusion on Bonding Models

Figure 7.2.1 clearly shows the difference between the failure patterns left by the tine and figure 7.2.2 shows the clot formation with the parallel bonds.

From these figures it is clear that the parallel bonds represent the experimental material behaviour much better than the contact bonds, thus the final simulation runs were done with parallel bonds.

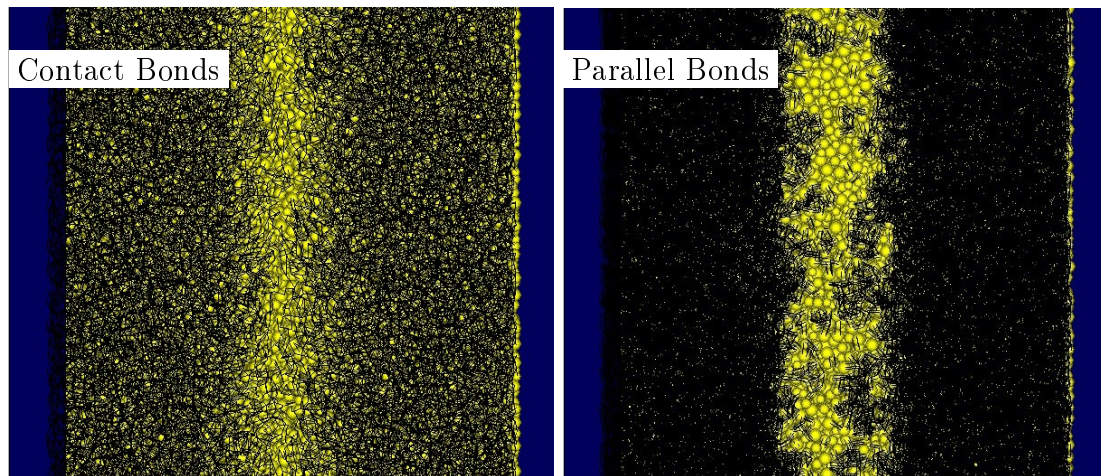


Figure 7.2.2: Top view of failure surface left by tine

The bonding model used plays a major role in the material behaviour. The contact bonds can clearly not model soil behaviour as realistically as the parallel bonds can. The parallel bonds can incorporate the brittleness of the soil and can show the clot formation on the surface. The calibration of the parallel bond parameters take longer as there are more parameters to consider and more possible combinations. When it comes to the simulation of brittle soil, parallel bonds were found to be the bonding model of choice even though it increases the simulation time.

## 7.3 Damping Effect

### 7.3.1 Global Damping

Preliminary simulations were done with the default global damping of *PFC3D* on the default damping constant of 0,7. The draft force obtained with this damping was in the same range as was found experimentally. However, the simulations with vibration showed an increased draft force compared to the non vibration runs. This is clearly in contrast to what is found in practice.

The reason for this can be explained by looking at the working of the global damping. It can be explained by looking at equation 7.3.1 (repeat of equation A.6.3). The detail of global damping, also called local nonviscous damping, are explained in Appendix A.6.

$$F_{(i)}^d = -\alpha |\mathcal{F}_{(i)}| \text{sign} (\mathcal{V}_{(i)}) \quad (7.3.1)$$

This equation shows that the damping force is equal to a fraction ( $\alpha$ ) of the

unbalance force working on a particle, in the opposite direction to the direction of motion. Thus with a damping constant of 0,7, the damping force is 70 % of the unbalance force working in on the particle. The effect will cause the simulation done with vibration, which has higher peak forces, to show a larger resistance from the particles.

This damping model does not give a realistic representation of forces exerted on the particles and can thus not be used for dynamic simulation which makes it unsuitable for the simulation of a vibratory tillage tool. It is more suitable for stabilizing particles during particle generation and for static applications.

### 7.3.2 No Damping

Further simulations were run without using damping. The draft forces obtained from these simulations were an order of magnitude less than the simulations with global damping. The vibration runs did, however, show a reduction of draft force of over 25 %. With no damping there is no form of energy dissipation, besides friction, which causes the particles to be overly active during vibration runs. Some particles would bounce around the whole soil bin. This behaviour is also not realistic.

### 7.3.3 Viscous Damping

It was decided to use viscous damping since it is the only alternative damping model available in *PFC3D*. The viscous damping force is a function of the damping constant and the relative velocity between particles at the contact point between the particles. Thus, it damps the contact and not the global particle motion (refer to Appendix A.6).

Simulations were run with damping constants of 0,5 and 1. The draft force obtained with damping constants, 0,5 and 1 were almost identical and showed a draft increase of up to 50 % over that without damping.

A damping constant of 1 requires that the restitution coefficient be zero (as  $e$  in equation (5.6.1) approaches zero,  $\beta$  approaches one in the limit). Thus the collisions between particles are completely inelastic and dissipates all energy. As explained in section 5.6 a damping constant of 0,5 has a high degree of damping ( $e = 0.16$ ) and dissipates most of the energy in the collision. Thus the reason why the draft forces associated with these two damping constants are similar, is that both damping constants provide similar energy dissipations.

With viscous damping the upheaval of the particles in front of the tine looks more realistic than without damping. Moreover the particles do not bounce around the soil bin when vibration is applied, as is the case without damping. The failure patterns left by the tine also seem more realistic in size and do not differ for the different damping constants.

Looking at the boundary and kinetic energy, there is almost no difference between the simulations done with different damping constants. This comparison was made with 20 mm radius particles and all runs were done with the same material properties except for the damping constant. The behaviour observed here was found with both contact and parallel bonds and for smaller ball radii.

### 7.3.4 Conclusion on Damping Model

It was found in these simulations that the damping model used in a simulation, has a large effect on the draft force. While the global damping gave draft forces in the same region as the experiments did, it also gave unrealistic forces during the vibration runs. This makes the damping model unsuitable for dynamic simulations.

The viscous damping model gives more realistic results regarding the draft reduction, however the forces are not as high as the experimental values. The viscous damping model is better suited for dynamic soil tillage applications such as the vibratory subsoiler.

## 7.4 Final Simulation Results and Observations

### 7.4.1 Results

The final simulations were done with a particle radius distribution of 10 mm to 15 mm and with parallel bonds. The particle and bond properties used in the simulations are as stated in tables 5.2.1 and 5.4.2, and with a stiffness as stated in table 5.3.2, as described in Chapter 5. More detail about the data analysis of the simulations are given in Appendix E.

The final simulation runs took around 2000 processing hours to complete. The vibration simulations took an average of 125 h per simulation (a total of 16 were done) where as the simulations without vibration took an average of 28 h per simulation (only 2 simulations were done).

The average draft force of each vibration run was calculated and compared to the average of the non vibration run. As was found in the field tests, the vibration reduces the draft force of the tine. The draft force reduction that was obtained is shown in figure 7.4.1 for both *run 1* and *run 2*, as well as the experimental values. It should be mentioned that only the steady state part of the data was used for the calculations.

The overall power requirement was also calculated for the simulations. The moment of the tine around its pivot point was directly extracted for the simulation. This along with the geometry of the tine allowed for the calculation of the torque

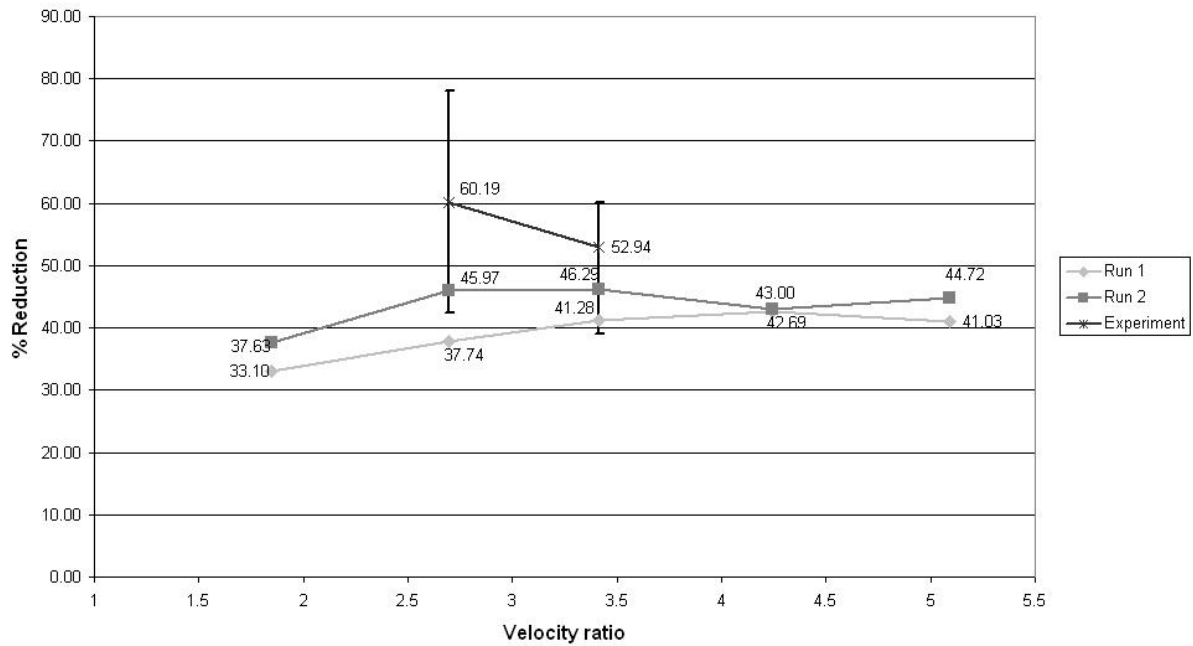


Figure 7.4.1: Draft reduction obtained from simulations

around the crank shaft as it would be for the physical machine (refer to figure E.2.1). Along with the rotational speed of the crank shaft, the torque on the crank shaft was used to calculate the crank power.

The total power requirement was obtained by adding the crank power to the draft power, which was determined by multiplying the average draft force with the constant forward velocity. The power ratios for the simulation runs are shown in figure 7.4.2. The power ratio is the ratio between the total power with vibration to the total power without vibration.

## 7.4.2 Observations

From figures 7.4.1 and 7.4.2 it can be seen that a larger amplitude and lower frequency results in a larger draft reduction with lower or similar power consumption as the larger frequency and lower amplitude. Similar behaviour was observed by Sakai *et al.* (1993) and Bandalan *et al.* (1999), where the largest amplitude gave the largest draft reduction and the lowest power ratio at the same velocity ratio.

As was found in the field tests, the simulation runs done with vibration pulverized the soil more than the simulations without vibration. Looking at a plot

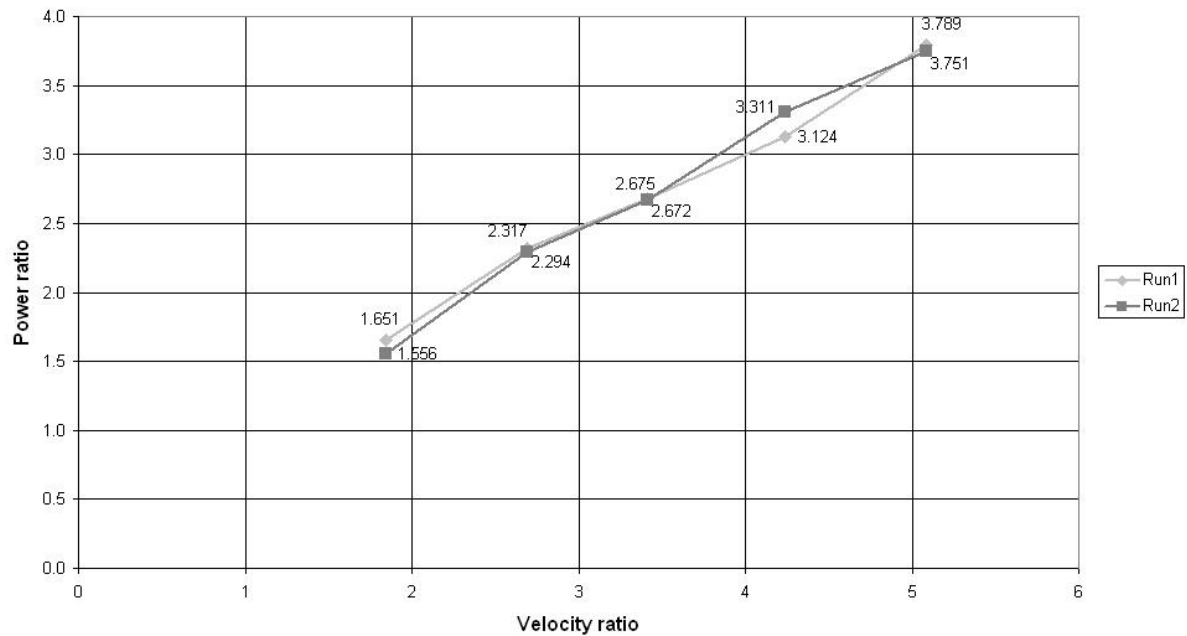


**Figure 7.4.2:** Power consumption from simulations

of the parallel bonds after the completion of a simulation run (figure 7.4.3) one can see that the non-vibration simulation shows larger and more conglomerates of unbroken parallel bonds. This suggest that the simulations done with vibration brakes more bonds and brakes smaller pieces or "clots".

Also seen form figure 7.4.3 is that the path left by the tine during a vibration simulation is wider than that left by the non-vibration simulation. A cross section view of the soil bin (figure 7.4.4) also show that with vibration the failure profile of the soil is larger than without vibration. Figure 7.4.5 shows a side view of the forward failure zone illustrating that with vibration the parallel bonds brake a distance further in front of the tine with vibration than without vibration. These three figures show that with vibration more soil is disturbed than without vibration.

## 7.5 Discussion

### 7.5.1 Draft Forces

As was found in the experiments, and in literature, the simulation shows a significant reduction in draft force due to the vibration. *Run 1* shows a steady increase



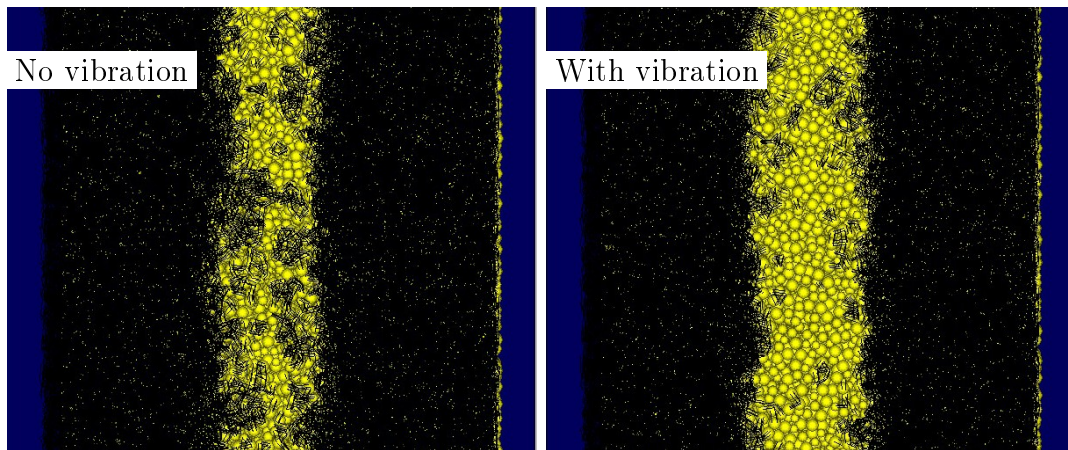


**Figure 7.4.3:** Top view of parallel bonds after simulation runs

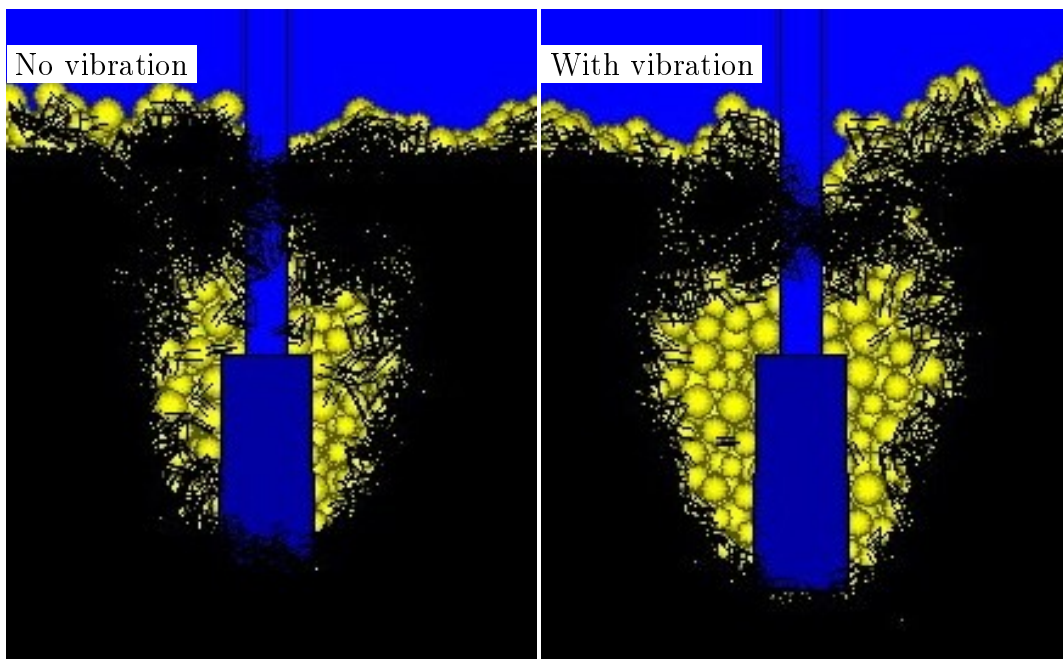


**Figure 7.4.4:** Cross section view of parallel bonds after simulation runs

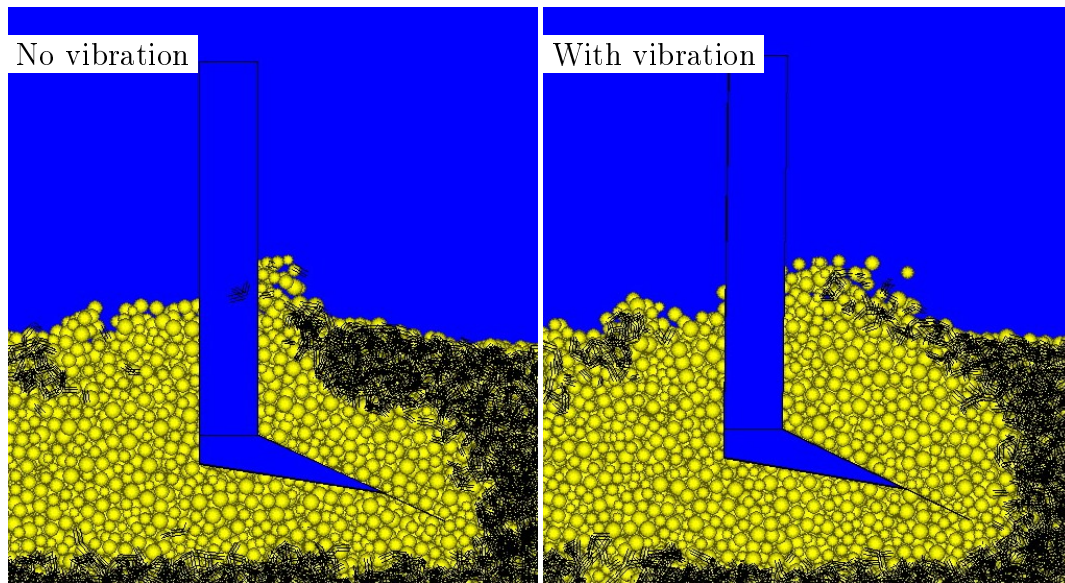


**Figure 7.4.5:** Side view of parallel bonds after simulation run

in the reduction with an increase in velocity ratio and then reduces, whereas *run 2* shows an increase, flattens off and then decreases as the velocity ratio increases. This does not correlate that well with the experimental results, however the experimental results did show a high degree of variation as is shown by the error bars in figure 7.4.1. These error bars shows the maximum and minimum reduction at each velocity ratio.

The draft reduction observed here does however correlate with what is found in literature. Both Sakai *et al.* (1993) and Bandalan *et al.* (1999) reported that the draft reduction increases as the velocity ratio increases and then reduces slightly again as the velocity ratio reaches values above 3 and 4 respectively.

The absolute values of the draft forces obtained during the simulation are up to six times smaller than that obtained in the experiments. The major cause of this is the fact that the simulation material does not represent the real soil accurately enough, thus it does not behave entirely as the real soil does. The particle diameter has a large influence here. For the real soil 70% of the particle diameters lie between  $53\ \mu\text{m}$  and  $500\ \mu\text{m}$ , compared to the simulation materials particles with diameters between 20 mm and 30 mm. As explained in section 7.1, a reduction in simulation particle diameter causes the draft force to show an increasing tendency.

The simulation material may give the same shear test results as the real soil but the dynamic behaviour of the material is not entirely accurate. Further influencing the dynamic behaviour of the material is the damping, which could not be calibrated for these simulations.

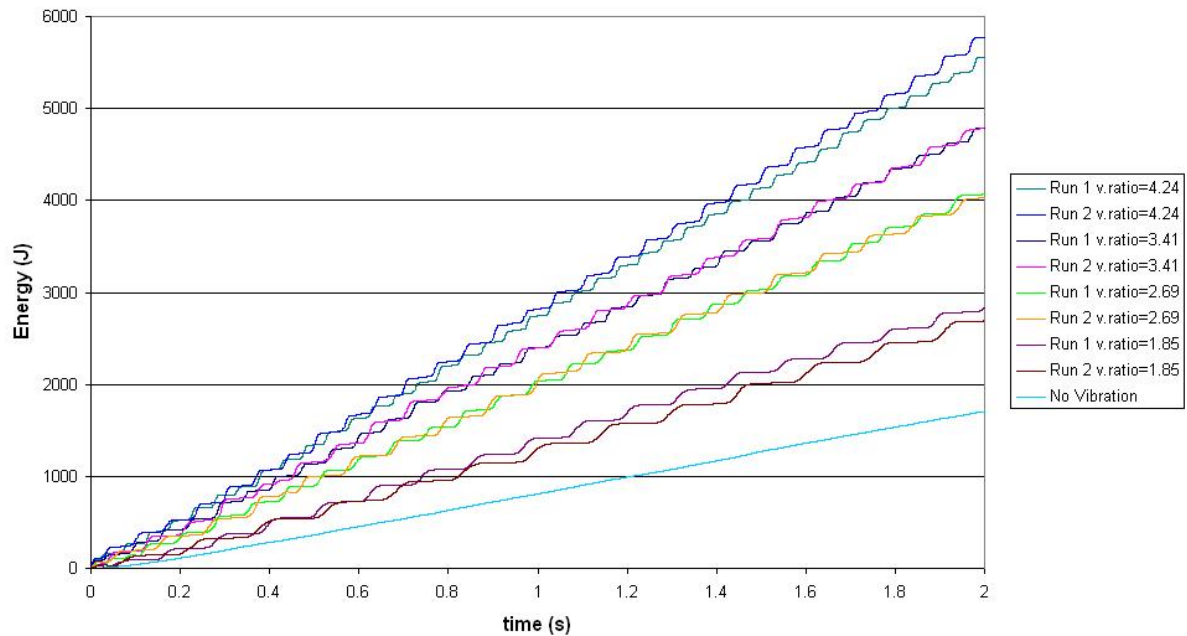


Figure 7.5.1: Cumulative work done by tine on particles

## 7.5.2 Power Consumption

Figure 7.4.2 show that the power consumption of the subsoiler increases as the velocity ratio increases. This also correlates with what is found in literature (Butson and MacIntyre, 1981; Sakai *et al.*, 1993; Bandalan *et al.*, 1999; Slattery and Desbiolles, 2003; Shahgoli *et al.*, 2006). The absolute values of the power ratio cannot be directly compared to what is found in the literature since it varies in each case. No power consumption data is available for the field tests, thus no comparison can be made.

Figure 7.5.1 is a plot of the work done by the tine on the particles cumulated over the simulation time. It shows a similar behaviour to the power consumption. The work increases as the velocity ratio increases suggesting that more work is being done on the soil as the velocity ratio increases. It also shows that for velocity ratio of 1,85 the work for *run 2* is less than for *run 1*, for the 2,69 and 3,41 velocity ratios the boundary work is almost the same, and for the 4,24 velocity ratio the boundary work for *run 2* is more. This can also be seen in the power ratio curve of figure 7.4.2.

### 7.5.3 Material Behaviour

The material behaviour observed during the simulation shows similarities with what was found in the field tests. These similarities include the bigger failure profile left by the vibration runs as well as the increased soil pulverization due to the vibration. The clot formation and soil upheaval in front of the tine shown in the simulations are also similar to what is found in practice.

Some factors that are however not similar to what was found in the field tests, was the shape of the failure profile left by the tine. Figure 4.5.2 shows that the real failure pattern follows a convex line from the the bottom of the tine to the surface whereas figure 7.4.4 shows that in the simulation the failure pattern follows a more concave line. This dissimilarity can be due to the large simulation particle diameters used.

## 7.6 Vibration: Why it Reduces the Draft Force

Form figure 7.5.1 it can be seen that with vibration more work is done on the soil. More energy is transferred directly into the soil resulting in an increased kinetic energy of the particles as seen in figure 7.6.1.

Figure 7.6.1 shows the kinetic energy of a non vibration simulation run and a vibration run. The kinetic energy referred to here is the average kinetic energy of all the particles in the particle assembly. It shows that the kinetic energy with vibration can peak up to five times that without vibration. The frequency does have an effect on the average kinetic energy but it is not clearly visible on this figure, thus only the kinetic energy of one vibration run is shown.

A higher kinetic energy suggests that the particles are in a higher state of energy due to increased velocities. The higher state of energy can suggest that the soil, or simulation particles, are in a quasi-fluidic state, thus reducing the soil (or particle assembly) strength. The theory of the strength reduction due to the quasi-fluidic state was introduced by Panagiotopoulos (1962) where it was observed that the soil is more active (there is more visible movement) close to a vibrating tine than to a rigid tine.

Higher kinetic energy, and thus particle velocities, can also show that there is more relative motion between particles, thus more bonds are broken and more frictional sliding takes place.

The major effect of vibration is visible in the stresses in the particle assembly. Figure 7.6.2 shows the maximum shear stress for a vibration simulation run (*run 1*), 12 Hz) as well as a non vibration simulation, calculated within measurement sphere number 4 (figure 6.2.1).

Looking at the simulation without vibration, it can be seen that the stress

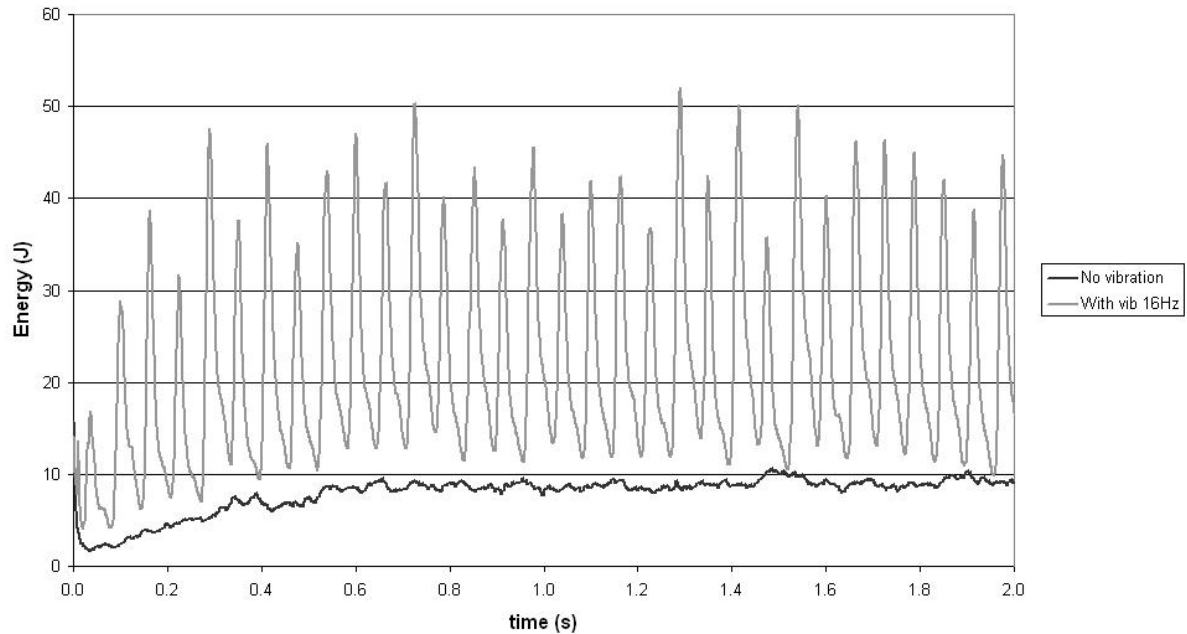


**Figure 7.6.1:** Particle kinetic energy

stays relatively constant until about 0,75 sec, where the stress increases as the tine approach the measurement sphere. After reaching a maximum value as the tine passes through, it falls back to a constant value as the tine moves away form the sphere.

Looking at the stresses for the vibration simulation one can clearly see that the particles are under a highly variable load and that the peak values of the stress increases as the tine approaches the sphere. After the tine moved through the measurement sphere the stresses fall back to a much lower value.

According to Koolen and Kuipers (1983) fatigue failure can occur in soils (as it would in steel or concrete) under repeated loading. The number of cycles required for failure decreases as the average stress increases, the cyclic amplitude increases and the difference between the maximum and minimum principle stresses increases.

The vibrating subsoiler clearly places the soil under a highly variable loading. For the physical soil this can cause a fatigue type failure of the soil, braking inter particle bonds, thus reducing the soil strength.

The variable loading also generates stress or pressure pulses that are transmitted through the particles (or real soil) causing the stresses to raise to a level where the non vibration run only reaches at a later point in time. For example, in figure 7.6.2

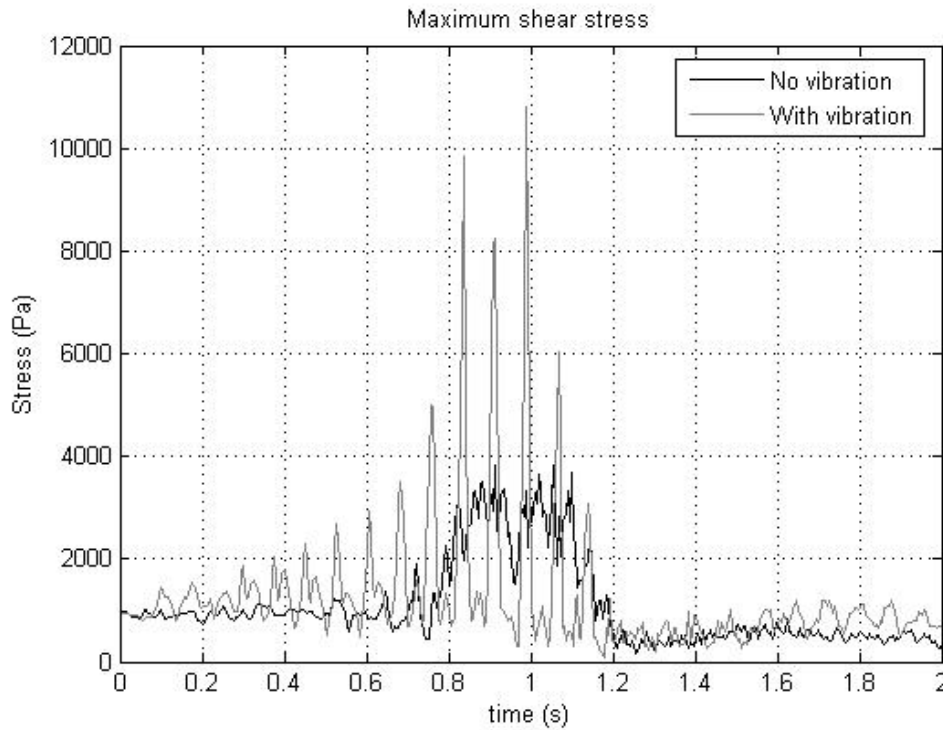


**Figure 7.6.2:** Maximum shear stress in particle assembly at measurement sphere 4

the vibration simulation reaches a stress level of 2,943 kPa at 0,606 s whereas the simulation without vibration reaches a similar stress level only at 0,818 s. This can be interpreted that the soil may fail a distance further in front of the tine compared to the non vibration run. This causes the tine to work in already partly failed soil, resulting in a lower average draft force.

For dry soils the stress pulses caused by the vibration can also create and propagate cracks and thereby weakening the soil as suggested by Szabo *et al.* (1998). Szabo *et al.* (1998) also suggested that for wet soils the stress pulses causes small bursts of hydrodynamic pressure and excess pore water pressure which reduces the soil strength by reducing the effective stress. For the simulation the stress pulses cause the parallel bonds to brake further in front of the tine reducing the particle assembly strength, causing the tine to work in a weakened particle assembly.

With vibration the peak stresses in the particle assembly can be up to three time larger than without vibration. These high stresses causes more damage to the material, reducing the material strength by creating more cracks and propagating them faster through the particle assembly. Creating more cracks also causes the particle assembly, and real soil, to brake up into finer pieces, leaving a more pulverized surface.

The back and forth movement of the tine during vibration also causes the tine to work the soil more than once, further adding to the increased pulverization (Niyamapa and Salokhe, 2000*b*). Niyamapa and Salokhe (2000*b*) also suggested that with vibration the soil is loaded by impact, as opposed to a continuous application of load without vibration. The impact loading can clearly be seen in the stress pulses shown in figure 7.6.2.

# Chapter 8

## Conclusion and Recommendations

### 8.1 Conclusion

The purpose of this project was to develop a three dimensional Discrete Element Model of an existing physical vibratory subsoiler that was developed during a previous study. The objective was to determine why the vibration reduces the draft force and what DEM parameters influence the simulation results. This information along with the simulation model can be used in the design and optimization of a future vibratory subsoiler.

The field test done with the existing subsoiler corroborates what was found in literature. Firstly it showed that the vibratory subsoiler significantly reduces the draft force. Secondly it showed that the vibratory subsoiler pulverizes the soil more than a rigid tillage tool, thus leaving a finer tilth. Thirdly it showed that the vibratory tool increases the amount of soil disturbed by the tine compared to a rigid tool.

The material property calibration was the most time consuming part of this project (5600 h). The direct shear test and confined compression test are the standard methods used to determine soil properties and for the calibration of DEM parameters. However, some difficulties were encountered in the calibration of the particle stiffness and the damping constant could not be calibrated. Due to these shortcomings and large time requirement, more efficient calibration methods are necessary for future research.

In spite of the difficulties encountered during the calibration, good correlations were found between the simulations and the experimental results. The simulations showed a significant reduction in draft force due to the vibrations as was found in the experiments and in literature. For similar velocity ratios the draft reduction of simulations fell within the variation range of the experimental values. The power consumption determined by the simulation also showed similar trends to what is



found in literature.

The simulations also showed very realistic material behaviour. It showed surface clot formation and similar sized failure patterns left by the tine. Vibration runs showed an increased pulverization with less and smaller surface clots compared to runs without vibration. The size of the failure patterns are also increased with vibration.

The ability of *PFC3D* to extract the stresses in the particle assembly and to determine the particle energies made it possible to study the effect of the vibration on the particles. This made it possible to determine why the vibration reduces the draft force. The main reasons why the vibration reduces the draft force can be summarized as follows:

- More work is being done on the soil increasing its kinetic energy causing the particle to be in a quasi-fluidic state with reduced strength.
- The increased peak stresses due to vibration causes the soil to fail further in front of the tine causing the tine to work in already failed soil.
- The highly variable loading of the soil causes a fatigue type failure of soil, weakening the structure.

Overall this project illustrated that the Discrete Element Method is capable of modelling the vibratory subsoiler. DEM is capable of replicating the draft force reduction due to vibration as well as the material behaviour and failure patterns. It also give the ability to study the effect of vibration on the soil in a bid to understand why vibration reduces the draft force.

However, the absolute values of the draft forces were not comparable to the experimental results. This is due to inability to accurately characterize the real soil, and due to the simplicity of the model.

With a refinement of the model and reduction in particle radii along with more accurate calibration methods, DEM could be able to simulate reality more accurately.

DEM can be used, even with the coarse model developed here, for design and optimization of agricultural tillage tools, especially to compare concepts against each other.

## 8.2 Recommendation

A major problem in DEM as a whole is the material property calibration, specifically where dynamic effects are more prominent. The material property tests done in this project would be sufficient to calibrate the simulation particle properties

for quasi static simulations relatively accurately. However, as pointed out in this project, the dynamic behaviour of the material could not be represented accurately. There is thus a shortcoming in the accurate calibration of material properties that would enable the accurate simulation of the dynamic behaviour of the material.

It is thus recommended that further research is done on calibration methods for dynamic DEM models. It is also recommended that more efficient, less time consuming methods are developed.

Further simulations of the vibratory subsoiler with different operating parameters and material properties are recommended. This must be done to study the effect of the different parameters on the draft force results and material behaviour.

A refinement of the current DEM model is also required for future studies. Smaller particles, a larger soil bin and a detail representation of the tine is recommended to simulate the experimental situation better. With increased processing power, or with parallel processing, smaller and more particles can be used in the simulation.

# Appendix A

## PFC 3D Detail

This Appendix describes the theory behind *PFC3D* in more detail. The discussion will start with the calculation cycle followed by the force-displacement law and the law of motion followed by discussions on the time step determination, damping, contact models etc. The discussion is an abstract of what is given in Itasca (2003*a*).

### Nomenclature

$A$	Area of parallel bond disk
$\mathcal{A}$	Generalized acceleration
$C$	Damping constant
$D$	Damping force
$F$	Force
$\mathcal{F}$	Generalized force
$G$	Shear modulus
$\dot{H}$	Angular momentum of particle
$I$	Moment of inertia
$J$	Polar moment of inertia
$K$	Stiffness (total or secant stiffness)
$M$	Moment
$\mathcal{M}$	Generalized mass
$R$	Particle radius
$U$	Overlap distance
$V$	Relative velocity at contact
$\mathcal{V}$	Generalized velocity

$c$	Critical damping constant
$d$	Distance between ball centers
$e$	Permutation symbol
$g$	Body force, normally gravity
$k$	Stiffness (incremental)
$m$	Mass
$n$	Normal vector
$t$	Time
$x_i$	Position vector
$\dot{x}_i$	Translational velocity
$\ddot{x}_i$	Translational acceleration
$\alpha$	Damping factor or safety factor
$\beta$	Critical damping ratio
$\Delta$	Indicates incremental value
$\delta$	Kronecker delta
$\mu$	Friction coefficient
$\nu$	Poisson's ratio
$\sigma$	Normal stress
$\tau$	Shear stress
$\omega$	Angular velocity
$\dot{\omega}$	Angular acceleration

### Superscripts

$n$	Indicate normal direction
$s$	Indicate tangential or shear direction

[ ] Refers to entity index eg:  $[A]$  refers to ball number  $A$ ,  $[b]$  refers to ball,  $[C]$  refers to contact,  $[w]$  refers to wall etc.

## A.1 Notation and Conventions

All vectors and tensor quantities are expressed using indicial notation with respect to a fixed right-handed cartesian coordinate system. Thus a position vector is given by  $x_i$ , and a stress tensor by  $\sigma_{ij}$ , where all indices range over the set  $\{1, 2, 3\}$ . The

Einstein summation convention is employed; thus the repetition of an index in a term denotes a summation with respect to that index over its range. Vertical braces denote the magnitude of a vector or the absolute value of a scalar. A dot over a variable denote a derivative with respect to time.

The Kronecker delta and permutation symbol are used. The Kronecker delta is defined as:

$$\delta_{i,j} = \begin{cases} 1, & \text{if } i = j \\ 0, & \text{otherwise} \end{cases} \quad (\text{A.1.1})$$

The permutation symbol is defined as:

$$e_{ijk} = \begin{cases} 0, & \text{if 2 indices coincide} \\ +1, & \text{if } i, j, k \text{ permute like } 1, 2, 3 \\ -1, & \text{otherwise} \end{cases} \quad (\text{A.1.2})$$

The Kronecker delta and the permutation symbol are related by the identity

$$e_{ijk}e_{ist} = \delta_{js}\delta_{kt} - \delta_{jt}\delta_{ks} \quad (\text{A.1.3})$$

The cross-product operation between two vectors  $\mathbf{a}$  and  $\mathbf{b}$  produces a vector  $\mathbf{c}$  that is perpendicular to both  $\mathbf{a}$  and  $\mathbf{b}$  and can be written using the permutation symbol as

$$\mathbf{a} \times \mathbf{b} = c_i = e_{ijk}a_jb_k \quad (\text{A.1.4})$$

## A.2 Calculation Cycle

The *PFC3D* calculation cycle is a time stepping algorithm where the law of motion for each particle, the force displacement law for each contact and the position update of the walls are continuously applied. The cycle starts with a update of contacts followed by the force displacement law where the resultant forces and moments on the particles are calculated based on the current position and velocities. The law of motion is then applied to update the particle velocity and displacement due to the application of the resultant forces and moments. Figure A.2.1 illustrates this calculation cycle.

## A.3 Force-Displacement Law

The force-displacement law as described here only includes the forces arising from contacts at a point. These forces work in at a contact point,  $x_i^{[C]}$ , which lays on

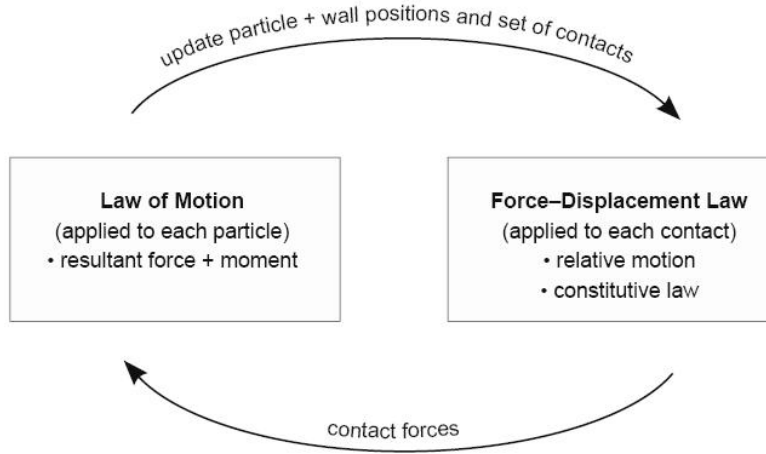


**Figure A.2.1:** *PFC3D* calculation cycle

a plane defined by a normal vector,  $n_i$ . Since the soft particle approach is used here, this contact point is within the interpenetration volume of the two entities in contact.

The normal vector for a ball-ball contact is directed along a line connecting the center points of the two particles. For two particles (A, and B) in contact (figure A.3.1), the normal vector is given as:

$$n_i = \frac{x_i^{[B]} - x_i^{[A]}}{d} \quad (\text{A.3.1})$$

where  $x_i^{[B]}$  and  $x_i^{[A]}$  are the position vectors of the ball centers and  $d$  is the distance between the ball centers and is given by:

$$d = |x_i^{[B]} - x_i^{[A]}| = \sqrt{(x_i^{[B]} - x_i^{[A]}) \cdot (x_i^{[B]} - x_i^{[A]})} \quad (\text{A.3.2})$$

For a ball-wall contact (figure A.3.2) the normal vector is directed along the line of the shortest distance between the wall and ball center. The shortest distance between the wall and the ball is either normal to the specific wall face or a vector connecting the wall end to the ball center.

The soft particle approach relies on the overlap between entities to calculate the contact forces. This overlap can be expressed as follows for a ball-ball and ball-wall contact:

$$U^n = \begin{cases} R^{[A]} + R^{[B]} - d & , (\text{ball} - \text{ball}) \\ R^{[b]} - d & , (\text{ball} - \text{wall}) \end{cases} \quad (\text{A.3.3})$$

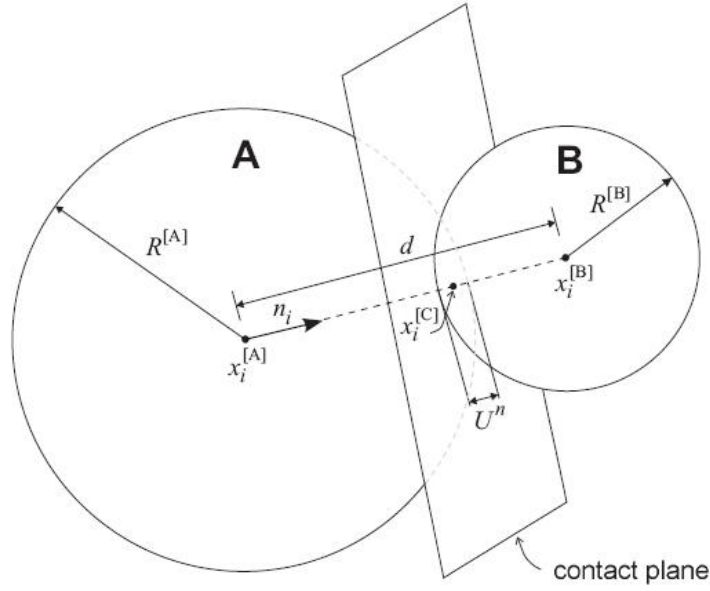


**Figure A.3.1:** Ball-ball contact notation

Here  $R^{[A]}$ ,  $R^{[B]}$  and  $R^{[b]}$  denotes the particle radii.

The position of the contact point can then be calculated as follows:

$$x_i^{[C]} = \begin{cases} x_i^{[A]} + (R^{[A]} - \frac{1}{2}U^n) n_i & , (ball - ball) \\ x_i^{[b]} + (R^{[b]} - \frac{1}{2}U^n) n_i & , (ball - wall) \end{cases} \quad (\text{A.3.4})$$

The contact force that develops at this contact can be resolved into two components; a normal force and a shear force with respect to the contact plane as given in equation (A.3.5).

$$F_i = F_i^n + F_i^s \quad (\text{A.3.5})$$

Here  $F_i^n$  is the normal force and  $F_i^s$  is the shear force.

In *PFC3D* the normal force can be expressed as given in equation (A.3.6) where the normal stiffness ( $K^n$ ) is a secant stiffness which relates total displacement to total force. On the other hand, the shear stiffness ( $k^s$ ) is a tangent modulus and relates shear incremental displacement to incremental shear force. Both the normal and shear stiffness are dependent on the contact model used and will be discussed later.

$$F_i^n = K^n U^n n_i \quad (\text{A.3.6})$$

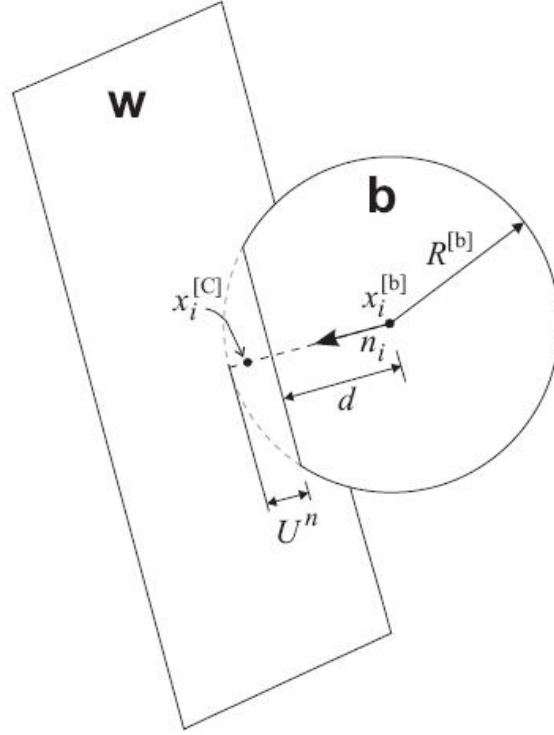


**Figure A.3.2:** Ball-wall contact notation

Unlike the normal force, the shear force is an incremental force and not only depends on the relative shear displacement but on the motion of the contact as well. At the formation of the contact the total shear force is set to zero and any further relative shear displacement increment results in an increment of shear force to be added to the current value. Thus the total shear force must be updated every time step along with the contact position and contact plane normal.

In order to update the shear force it is rotated about a line common to the old and new contact plane and about the new normal direction. The first rotation is given by:

$$\{F_i^s\}_{rot.1} = F_j^s (\delta_{i,j} - e_{ijk} e_{kmn} n_m^{[old]} n_n) \quad (\text{A.3.7})$$

Here  $n_m^{[old]}$  is the old contact plane normal. The second rotation is given by:

$$\{F_i^s\}_{rot.2} = \{F_i^s\}_{rot.1} (\delta_{i,j} - e_{ijk} \langle \omega_k \rangle \Delta t) \quad (\text{A.3.8})$$

where  $\langle \omega_k \rangle$  is the average angular velocity of the contacting entities about the new normal direction which is given by:



$$\langle \omega_k \rangle = \frac{1}{2} \left( \omega_j^{[\Phi^1]} + \omega_j^{[\Phi^2]} \right) n_j n_i \quad (\text{A.3.9})$$

Here  $\omega_i^{[\Phi^j]}$  is the rotational velocity of entity  $\Phi^j$ , given by:

$$\{\Phi^1, \Phi^2\} = \begin{cases} \{A, B\} & , (ball - ball) \\ \{b, w\} & , (ball - wall) \end{cases} \quad (\text{A.3.10})$$

The contact velocity,  $V_i$ , is defined as the velocity of ball B relative to ball A, or the velocity of the wall relative to the ball, at the contact point. It is given as follows:

$$V_i = \left( \dot{x}_i^{[\Phi^2]} + e_{ijk} \omega_j^{[\Phi^2]} \left( x_k^{[C]} - x_k^{[\Phi^2]} \right) \right) - \left( \dot{x}_i^{[\Phi^1]} + e_{ijk} \omega_j^{[\Phi^1]} \left( x_k^{[C]} - x_k^{[\Phi^1]} \right) \right) \quad (\text{A.3.11})$$

Here  $\dot{x}_i^{[\Phi^j]}$  is the translational velocity of entity  $\Phi_j$ , and in the case of ball-wall contact,  $\omega_i^{[w]}$  is the rotational velocity of the wall with respect to its center of rotation.

This contact velocity can be resolved into a normal and shear components in the contact plane and the shear velocity can be given as:

$$V_i^s = V_i - V_i^n = V_i - V_j n_j n_i \quad (\text{A.3.12})$$

The relative shear displacement can now be calculated over the time step  $\Delta t$ :

$$\Delta U_i^s = V_i^s \Delta t \quad (\text{A.3.13})$$

The shear force increment can then be calculated as:

$$\Delta F_i^s = -k^s \Delta U_i^s \quad (\text{A.3.14})$$

To obtain the new shear force vector, the incremental shear force vector is added to the old shear force vector as follows:

$$F_i^s = \{F_i^s\}_{rot.2} + \Delta F_i^s \quad (\text{A.3.15})$$

The total force vectors are then determined as in equation (A.3.5) and the resultant forces and moments on the entities are then determined as follows:

$$F_i^{[\Phi^1]} \leftarrow F_i^{[\Phi^1]} - F_i \quad (\text{A.3.16})$$

$$F_i^{[\Phi^2]} \leftarrow F_i^{[\Phi^2]} + F_i \quad (\text{A.3.17})$$

$$M_i^{[\Phi^1]} \leftarrow M_i^{[\Phi^1]} - e_{ijk} \left( x_j^{[C]} - x_j^{[\Phi^1]} \right) F_k \quad (\text{A.3.18})$$

$$M_i^{[\Phi^2]} \leftarrow M_i^{[\Phi^2]} + e_{ijk} \left( x_j^{[C]} - x_j^{[\Phi^2]} \right) F_k \quad (\text{A.3.19})$$

## A.4 Law of Motion

The resultant forces and moments determined as described above, are used in Newton's second law to derive an equation of motion for the particles. The motion of the particle is defined by a translational motion with displacement  $x_i$ , velocity  $\dot{x}_i$  and acceleration  $\ddot{x}_i$ , and a rotational motion with angular velocity  $\omega_i$  and angular acceleration  $\dot{\omega}_i$ .

The translational and rotational motion can be calculated separately with the translation vector equation given by equation (A.4.1) and the rotational motion given by equation (A.4.2).

$$F_i = m (\ddot{x}_i - g_i) \quad (\text{A.4.1})$$

Here  $F_i$  is the resultant force,  $m$  is the total mass of the particle and  $g_i$  is the body force acceleration vector which is normally the gravitational acceleration.

$$M_i = \dot{H}_i \quad (\text{A.4.2})$$

Here  $M_i$  is the resultant moments that work in on the particle and  $\dot{H}_i$  is the angular momentum of the particle. This equation is relative to a local coordinate system that is located at the center of mass of the particle. If this coordinate system is aligned with the principle axes of inertia of the particle then equation (A.4.2) become:

$$M_1 = I_1 \dot{\omega}_1 + (I_3 - I_2) \omega_3 \omega_2 \quad (\text{A.4.3})$$

$$M_2 = I_2 \dot{\omega}_2 + (I_1 - I_3) \omega_1 \omega_3 \quad (\text{A.4.4})$$

$$M_3 = I_3 \dot{\omega}_3 + (I_2 - I_1) \omega_2 \omega_1 \quad (\text{A.4.5})$$

Here  $I_1$ ,  $I_2$  and  $I_3$  are the principle moments of inertia,  $\dot{\omega}_1$ ,  $\dot{\omega}_2$  and  $\dot{\omega}_3$  are the angular accelerations about the principle axes, and  $M_1$ ,  $M_2$  and  $M_3$  are the components of the resultant moment resolved around the principle axes.

Since any local axis system through the mass center of a spherical particle with a uniformly distributed mass, is a principle axes, the three principle moments of

inertia are equal. Thus for a spherical particle with radius  $R$ , the rotational motion can be expressed as follows:

$$M_i = I\dot{\omega}_i = \left(\frac{2}{5}mR^2\right)\dot{\omega}_i \quad (\text{A.4.6})$$

Equations (A.4.1) and (A.4.6) can be integrated using a centered finite difference procedure with time step  $\Delta t$ . The translational and rotational velocities,  $\dot{x}_i$  and  $\dot{\omega}_i$  are calculated at the mid-intervals of  $t \pm n\Delta t/2$  while  $x_i$ ,  $\ddot{x}_i$ ,  $\dot{\omega}_i$ ,  $F_i$  and  $M_i$  are computed at the primary intervals of  $t \pm n\Delta t$ .

The translational and rotational acceleration at time  $t$  can be determined from the velocities computed at the previous and next mid time steps as follows:

$$\ddot{x}_i^{(t)} = \frac{1}{\Delta t} \left( \dot{x}_i^{(t+\Delta t/2)} - \dot{x}_i^{(t-\Delta t/2)} \right) \quad (\text{A.4.7})$$

$$\ddot{\omega}_i^{(t)} = \frac{1}{\Delta t} \left( \dot{\omega}_i^{(t+\Delta t/2)} - \dot{\omega}_i^{(t-\Delta t/2)} \right) \quad (\text{A.4.8})$$

By rearranging equations (A.4.7) and (A.4.8) and inserting equations (A.4.1) and (A.4.6), the velocities for the next mid time step can be determined.

$$\dot{x}_i^{(t+\Delta t/2)} = \dot{x}_i^{(t-\Delta t/2)} + \left( \frac{F_i^{(t)}}{m} + g_i \right) \Delta t \quad (\text{A.4.9})$$

$$\dot{\omega}_i^{(t+\Delta t/2)} = \dot{\omega}_i^{(t-\Delta t/2)} + \left( \frac{M_i^{(t)}}{I} \right) \Delta t \quad (\text{A.4.10})$$

The position for the particle center can now be updated as follows:

$$x_i^{(t+\Delta t)} = x_i^{(t)} + \dot{x}_i^{(t+\Delta t/2)} \Delta t \quad (\text{A.4.11})$$

The motion calculation can be summarized as follows: with the values of  $\dot{x}_i^{(t-\Delta t/2)}$ ,  $\dot{\omega}_i^{(t-\Delta t/2)}$ ,  $x_i^{(t)}$ ,  $F_i^{(t)}$  and  $M_i^{(t)}$  known, equations (A.4.9) and (A.4.10) can be used to obtain  $\dot{x}_i^{(t+\Delta t/2)}$  and  $\dot{\omega}_i^{(t+\Delta t/2)}$ . Then equation (A.4.11) can be used to obtain  $x_i^{(t+\Delta t)}$ . From this new position,  $F_i^{(t+\Delta t)}$  and  $M_i^{(t+\Delta t)}$  can be obtained from the force-displacement law.

## A.5 Time Step Determination

For the finite difference integration scheme used with the motion calculation a small enough time step must be used to ensure stability. The time step used in *PFC3D* is a fraction of this critical time step which is estimated as will be discussed below.

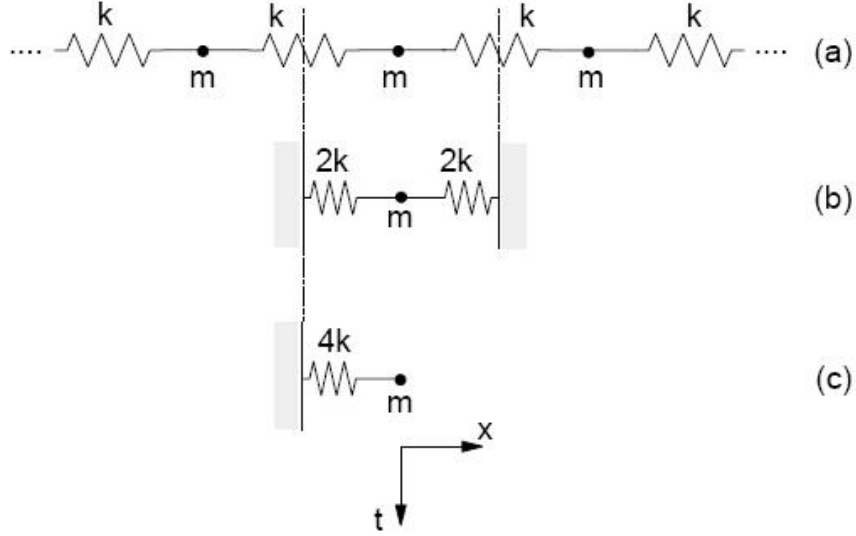


**Figure A.5.1:** Multiple mass-spring system

For an infinite number of point masses and springs (figure A.5.1), the shortest period of vibration will occur when the masses are moving in synchronized opposing motion. This motion causes that the center of the springs are stationary so that the motion of a single point mass can be described as shown in figure A.5.1(b) and (c). The critical time step is then:

$$t_{crit} = 2\sqrt{\frac{m}{4k}} = \sqrt{\frac{m}{k}} \quad (\text{A.5.1})$$

where  $k$  is the stiffness of each spring and  $m$  is the point mass.

The same argument can be made for rotational motion but with  $m$  replaced with  $I$ , the moment of inertia. For a generalized multi mass-spring system the critical time step can be given by:

$$t_{crit} = \begin{cases} \sqrt{\frac{m}{k^{trans}}}, & (\text{translational}) \\ \sqrt{\frac{I}{k^{rot}}}, & (\text{rotational}) \end{cases} \quad (\text{A.5.2})$$

A three-dimensional system, such as what is modeled in *PFC3D* contains many particles with different mass and stiffness. By applying equation (A.5.2) separately to each degree of freedom of each particle, a critical time step is determined for each particle. The final critical time step for the system of particles is taken to be the minimum of all the critical time steps calculated for all the particles.

The translational and rotational stiffness of the particles can be expressed as follows:

$$k_{(i)}^{trans} \approx \bar{k}_{(ii)} = [(k^n - k^s) n_{(i)}^2] + [A \{(\bar{k}^n - \bar{k}^s) n_{(i)}^2 + \bar{k}^s\}] \quad (\text{A.5.3})$$

$$k_{(i)}^{rot} \approx \hat{k}_{ii} = [R^2 k^s (1 - n_{(i)}^2)] + [A \{R^2 \bar{k}^s (1 - n_{(i)}^2)\}] + (J\bar{k}^s - I\bar{k}^n) n_{(i)}^2 + I\bar{k}^n \quad (\text{A.5.4})$$

Here the second term on the right is only present if parallel bonds are used between particles, if there is no parallel bond these terms are omitted. The subscripts inclosed in braces indicate that this is not a vector relation and Einstein summation convention does not apply to repeated indices.

A differential density scaling for the time step is also available. This time scaling involves the modification of the inertial mass of each particle so that the critical time step becomes unity. This can be used to reduce the total amount of cycles required. However it can only be used to obtain steady state solutions where there is no particle acceleration and any non-steady state data extracted will be inaccurate.

## A.6 Mechanical Damping

In order to reach a steady state solution with in a reasonable amount of cycles damping is employed to dissipate energy along with the friction. In *PFC3D* three types of damping are available: local nonviscous damping, combined damping and viscous damping.

### Local nonviscous damping

For this damping a damping force is added to the equation of motion as follows:

$$\mathcal{F}_i + F_{(i)}^d = \mathcal{M}_{(i)} \mathcal{A}_{(i)} \quad (\text{A.6.1})$$

for  $i = 1..6$ . Here  $\mathcal{F}_{(i)}$ ,  $\mathcal{M}_{(i)}$ , and  $\mathcal{A}_{(i)}$  are generalized force (which includes gravity), mass and acceleration given by:

$$\mathcal{M}_{(i)} \mathcal{A}_{(i)} = \begin{cases} m\ddot{x}_{(i)}, & i = 1..3 \\ I\dot{\omega}_{(i-3)}, & i = 4..6 \end{cases} \quad (\text{A.6.2})$$

The damping force can given as follows:

$$F_{(i)}^d = -\alpha |\mathcal{F}_{(i)}| \text{sign}(\mathcal{V}_{(i)}) \quad (\text{A.6.3})$$

where  $\mathcal{V}_{(i)}$  is the generalized velocity given by equation (A.6.4) and the *sign* function is given by equation (A.6.5).

$$\mathcal{V}^{(i)} = \begin{cases} \dot{x}^{(i)}, & i = 1...3 \\ \omega_{(i-3)}, & i = 4...6 \end{cases} \quad (\text{A.6.4})$$

$$\text{sign}(y) = \begin{cases} +1, & y > 0 \\ -1, & y < 0 \\ 0, & y = 0 \end{cases} \quad (\text{A.6.5})$$

From equation (A.6.3) it can be seen that the magnitude of the damping force is a fraction ( $\alpha$ , default= 0.7) of the resultant force that work in on the particle. Its direction is in the opposite direction of motion.

This local damping force only damps accelerated motion and not steady state motion where the resultant force is zero. Other advantages of the local damping is that the damping constant,  $\alpha$ , is dimensionless and that the damping is frequency independent.

### Combined damping

Local damping is dependent on the fact that the velocity must change sign. Thus in a situation where significant rigid body motion occur along with oscillatory motion, there may be insignificant damping. An alternative damping can be derived by realizing that the derivative of the unbalance force is proportional to the minus of the velocity. Thus for a single degree of freedom system in harmonic motion the velocity is given by:

$$v = a \sin(\omega t) \quad (\text{A.6.6})$$

then the derivative of the unbalance force is:

$$\frac{dF}{dt} = \frac{d^2v}{dt^2} = -a\omega^2 \sin(\omega t) \quad (\text{A.6.7})$$

Thus, the derivative of the unbalance force is proportional to the velocity but, the mean value of  $dF/dt$  is zero even if the mean of the velocity is not. In *PFC3D* a combined damping is available that combine the damping forces of the local damping as well as that from  $dF/dt$ . However this type of damping is less efficient than the local damping and should thus only be used when significant rigid-body motion occurs along with oscillation.

### Viscous damping

A viscous damping option is also available in *PFC3D* where a viscous damping force is added to the equation of motion. Figure A.6.1 shows how the viscous damping is implemented at the contacts as normal and shear dashpots.

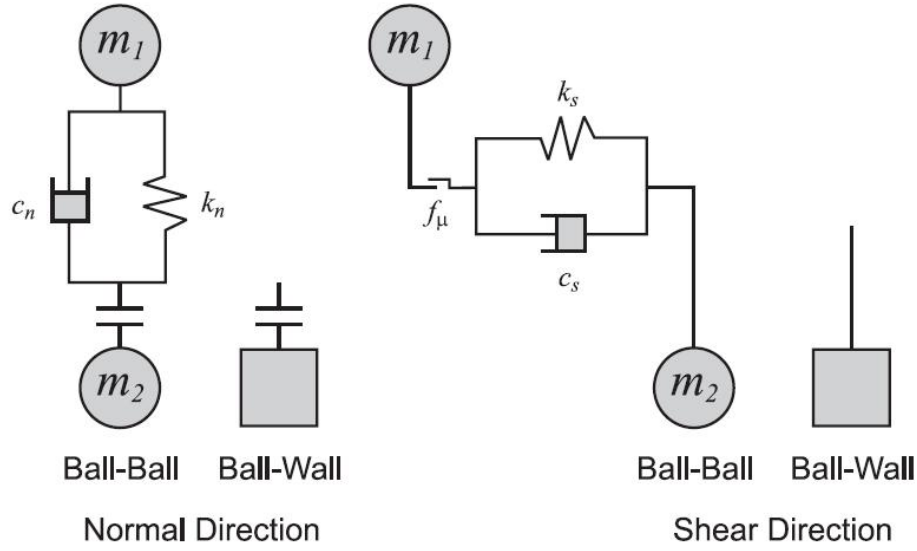


Figure A.6.1: Viscous damping at contacts

The damping force can be given as:

$$D_i = C_i |V_i| \quad (\text{A.6.8})$$

where  $C_i$  is the damping constant and  $V_i$  is the relative velocity at the contact. Here  $i = n$  for the normal direction and  $i = s$  for the shear direction, this also holds for the equations to follow.

In *PFC3D* the damping constant is not specified but the damping ratio,  $\beta_i$  is specified so that the damping constant becomes:

$$C_i = \beta_i C_i^{crit} \quad (\text{A.6.9})$$

where the critical damping constant is given by:

$$C_i^{crit} = 2m\omega_i = 2\sqrt{mk_i} \quad (\text{A.6.10})$$

Here  $\omega_i$  is the natural frequency of undamped oscillation,  $k_i$  is the contact tangent stiffness and  $m$  is the effective system mass. For a ball-ball contact the  $m$  is taken as the average mass of the balls in contact and for ball-wall contact  $m$  is taken as the ball mass.

For a damping ratio of unity the system is said to be critically damped, for  $\beta_i < 1$  the system is underdamped and for  $\beta_i > 1$  the system is over damped.

Viscous damping unfortunately reduces the time step for the calculations. The new apparent stiffness with the inclusion of viscous damping can be calculated as follows:

$$k'_i = \alpha \frac{k_i}{\left(\sqrt{1 + \lambda_i^2} - \lambda_i\right)^2} \quad (\text{A.6.11})$$

where  $k_i$  is the contact stiffness without damping,  $\alpha$  is the safety factor, and  $\lambda_i$  is given as:

$$\lambda_i = \frac{c_i}{2k_i\Delta t_0} \quad (\text{A.6.12})$$

Here  $c_i$  is the critical damping constant and  $\Delta t_0$  is the time step without viscous damping.

When viscous damping is used, the damping force can also create a tensile force between particles if they move away from each other. This effect can however be deactivated at the user's request.

## A.7 Contact Models

The contact constitutive models are made up of three different models: the stiffness model which relates displacement to contact force, a slip model that forms a relation between normal and shear contact forces and a bonding model that limits the total contact forces. This section will cover the most widely used contact models such as the linear and Hertz contact laws along with the built in slip model and the two bonding models available. Some less frequently used models will also be covered under alternative models.

### A.7.1 Contact-Stiffness Models

The contact stiffness models relate the relative displacement at the contact to the contact force according to equations (A.3.6) and (A.3.14). The contact stiffness in these equations is calculated according to the chosen contact model. The two models that are used most often are the linear contact model and the Hertz-Mindlin contact models.

#### Linear contact model

For the linear model each entity is given a constant normal and shear stiffness so that there is a linear relationship between the force and displacement. The total stiffness at the contact can then be calculated by assuming the individual stiffnesses work in series. The normal secant stiffness can be calculated as:



$$K^n = \frac{k_n^{[A]} k_n^{[B]}}{k_n^{[A]} + k_n^{[B]}} \quad (\text{A.7.1})$$

The shear tangent contact stiffness can be calculated as follows:

$$k^s = \frac{k_s^{[A]} k_s^{[B]}}{k_s^{[A]} + k_s^{[B]}} \quad (\text{A.7.2})$$

For both these equations  $A$  and  $B$  denote the two entities in contact.

### Hertz-Mindlin contact model

The Hertz-Mindlin contact model are one of the built-in options and are based on the model by Mindlin and Deresiewicz (1953). The only two input parameters are the shear modulus,  $G$ , and the poisson's ratio,  $\nu$ , of the particles in contact. The normal and shear stiffness as used by *PFC3D* are shown in equation (A.7.3) and (A.7.4), respectively.

$$K^n = \left( \frac{2G\sqrt{2\tilde{R}}}{3(1-\nu)} \right) \sqrt{U^n} \quad (\text{A.7.3})$$

$$k_s = \left( \frac{2 \left( G^2 3(1-\nu) \tilde{R} \right)^{1/3}}{2-\nu} \right) |F_i^n|^{1/3} \quad (\text{A.7.4})$$

Here  $F^n$  and  $U^n$  are the normal force and particle overlap as defined before, respectively. For ball-to-ball contact the following definitions apply:

$$\tilde{R} = \frac{2R^{[A]}R^{[B]}}{R^{[A]} + R^{[B]}} \quad (\text{A.7.5})$$

$$G = \frac{1}{2} (G^{[A]} + G^{[B]}) \quad (\text{A.7.6})$$

$$\nu = \frac{1}{2} (\nu^{[A]} + \nu^{[B]}) \quad (\text{A.7.7})$$

The superscripts  $A$  and  $B$  refer to the two particles in contact. For ball-to-wall contact this definition are as follows:

$$\tilde{R} = R^{[ball]} \quad (\text{A.7.8})$$

$$G = G^{[ball]} \quad (\text{A.7.9})$$

$$\nu = \nu^{[ball]} \quad (\text{A.7.10})$$

In these equation  $G$  is the shear modulus,  $\nu$  is the Poisson's ratio and  $R$  is the particle radius.

### A.7.2 Slip Model

The slip model limits the shear force by allowing slip to occur and provides normal tensile strength. This model is always active unless contact bonds are used. The bonding models will be discussed in the next section, but when a contact bond is used its behaviour supersedes that of the slip model. With the use of parallel bonds, however, the slip model is active.

The contact friction is incorporated with the slip model and the friction coefficient is given by  $\mu$ . For friction calculation  $\mu$  is taken as the minimum friction coefficient of the entities in contact.

Slip is induced by limiting the maximum shear force at the contact according to:

$$F_{max}^s = \mu |F_i^n| \quad (\text{A.7.11})$$

If the shear force calculated by the relative shear displacement and shear stiffness exceeds  $F_{max}^s$ , then slip is allowed to occur and the shear force is set equal to  $F_{max}^s$ .

### A.7.3 Bonding Models

The bonding models in *PFC3D* allow particles to be bonded at the contact points. Two bonding models available are contact bonds, which can be seen as glue joining of particles over a vanishingly small area, and parallel bonds that can be seen as a glue bonding of finite circular cross-section. The contact bonds can only transmit force between particles where as the parallel bonds can transmit moment as well.

As mentioned before, the slip model is deactivated when the contact bond model is used, but contact bonds and parallel bonds can be used together. Once a bond is formed between particles, the contact remains until the bond strength is exceeded and the bond brakes. When the bond strength is exceeded the contact is deleted, and in the case where contact bonds are deleted, the slip model is reactivated for that specific particles.

#### Contact-bond model

The contact bonds is specified by a normal contact bond strength  $F_c^n$  (force), and a shear contact bond strength  $F_c^s$ . The contact bond can be seen as a pair of

elastic springs with the above mentioned strengths working in a normal and shear direction.

Contact bonds overrides the slip model and the maximum shear force is limited by the shear bond strength and not as in equation (A.7.11). Once this strength is exceeded the bond brakes and slip is allowed where the shear force is then limited as with the slip model.

The normal strength of the contact bond allows tensile forces to be developed between particles if the overlap becomes negative (ie. when the particles separate). If the normal strength of the bond is exceeded the bond brakes and the normal contact force is set to zero.

Both the normal and shear stiffness used for the contact bond is that which is assigned to the particle itself.

### Parallel-bond model

The parallel bonds can be seen as a set of springs with constant normal and shear stiffness that is uniformly distributed over a circular disk laying in the contact plane. These springs work in parallel with any contact point springs such as the particle stiffness, contact bonds or slip model. Relative motion at the contact causes the parallel bond to transmit normal and shear forces as well as moments between particles in contact. These transmitted forces is limited by the parallel bond normal and shear strength, if this strength is exceeded the bonds will brake and will be deleted.

The parallel bond is specified by the normal and shear stiffness,  $\bar{k}^n$  and  $\bar{k}^s$  (stress/displacement), normal and shear strength,  $\bar{\sigma}_c$  and  $\bar{\tau}_c$  (stress), and the bond disk radius,  $\bar{R}$ . Figure A.7.1 shows a representation of the parallel bond along with the shear and normal force and moments that it transmits. The total force and moment transmitted by the parallel bond is given as:

$$\bar{F}_i = \bar{F}_i^n + \bar{F}_i^s \quad (\text{A.7.12})$$

$$\bar{M}_i = \bar{M}_i^n + \bar{M}_i^s \quad (\text{A.7.13})$$

The total force and moment exerted by the parallel bond is determined in an incremental fashion. When contact is formed,  $\bar{F}_i$  and  $\bar{M}_i$  is set to zero and any relative displacement or rotation increment will cause a incremental force or moment to develop. The incremental normal and shear forces are calculated as:

$$\Delta \bar{F}_i^n = (-\bar{k}^n A \Delta U_i^n) n_i \quad (\text{A.7.14})$$

$$\Delta \bar{F}_i^s = -\bar{k}^s A \Delta U_i^s \quad (\text{A.7.15})$$

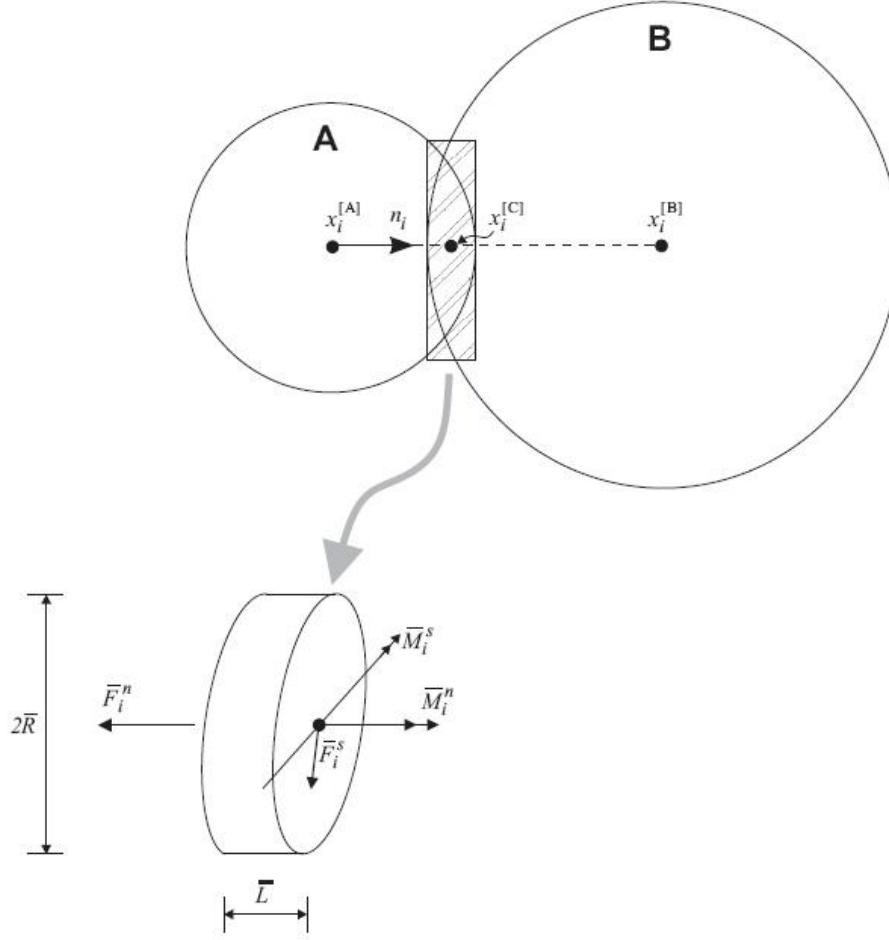


Figure A.7.1: Parallel bond

The moment increments are given by:

$$\Delta \bar{M}_i^n = (-\bar{k}^s J \Delta \theta^n) n_i \quad (\text{A.7.16})$$

$$\Delta \bar{M}_i^s = -\bar{k}^n I \Delta \theta_i^s \quad (\text{A.7.17})$$

where  $\Delta \theta_i = (\omega_i^{[B]} - \omega_i^{[A]}) \Delta t$ .

The area of the bond disc is given by  $A = \pi \bar{R}^2$ . The polar moment of inertia of the disc cross-section by  $J = \frac{1}{2} \pi \bar{R}^2$ . The moment of inertia of the disc cross-section about an axis through the contact point in the direction of  $\Delta \theta_i^s$  is given by  $I = \frac{1}{4} \pi \bar{R}^4$ .

The total contact forces exerted by the parallel bond can be calculated in a similar manner as was done with the contact forces before. This calculation include the rotation of the shear force vector as was done before. The total force equations become:

$$\bar{F}_i^n \leftarrow \bar{F}^n n_i + \Delta \bar{F}_i^n \quad (\text{A.7.18})$$

$$\bar{F}_i^s \leftarrow \{\bar{F}_i^s\}_{rot.2} + \Delta \bar{F}_i^s \quad (\text{A.7.19})$$

The moment vector can also be calculated as follows:

$$\bar{M}_i^n \leftarrow \bar{M}^n n_i + \Delta \bar{M}_i^n \quad (\text{A.7.20})$$

$$\bar{M}_i^s \leftarrow \{\bar{M}_i^s\}_{rot.2} + \Delta \bar{M}_i^s \quad (\text{A.7.21})$$

With the aid of beam theory, the stresses acting on the parallel bond can be calculated:

$$\sigma_{max} = \frac{-\bar{F}^n}{A} + \frac{|\bar{M}_i^s|}{I} \bar{R} \quad (\text{A.7.22})$$

$$\tau_{max} = \frac{|\bar{F}_i^s|}{A} + \frac{|\bar{M}^n|}{J} \bar{R} \quad (\text{A.7.23})$$

If either of these stresses exceed the bond normal or shear strength, the bond will break.

If the bonds stay intact, their contribution to the resultant force and moment on the two particles Can be calculated as follows:

$$F_i^{[A]} \leftarrow F_i^{[A]} - \bar{F}_i \quad (\text{A.7.24})$$

$$F_i^{[B]} \leftarrow F_i^{[B]} + \bar{F}_i \quad (\text{A.7.25})$$

$$M_i^{[A]} \leftarrow M_i^{[A]} - e_{ijk} \left( x_j^{[C]} - x_j^{[A]} \right) \bar{F}_k - \bar{M}_i \quad (\text{A.7.26})$$

$$M_i^{[B]} \leftarrow M_i^{[B]} + e_{ijk} \left( x_j^{[C]} - x_j^{[B]} \right) \bar{F}_k - \bar{M}_i \quad (\text{A.7.27})$$

Where  $F_i^{[\Phi]}$  and  $M_i^{[\Phi]}$  are the force and moment sums of sphere  $\Phi$ , and  $\bar{F}_i$  and  $\bar{M}_i$  are given by equations (A.7.12) and (A.7.13).

## A.8 Contact Detection

In *PFC3D* entities such as the balls, walls and contacts, are represented by data elements. These elements are C++ data structures linked in a list of the data structure by pointers (memory addresses). Each entity is assigned a single data element that contains geometrical and mechanical data along with a pointer to the next element in the linked list of similar elements. Balls contain an extra pointer to the list of its contacts and contacts contain two extra pointer to the two entities in contact.

During contact detection it is impossible to check all possible pairs of elements for contact at each time step because search time increase quadratically with the number of entities. *PFC3D* uses a neighbor list for detection, which takes less search time.

The volume containing the model (consisting of balls, walls and contacts) are divided into a matrix of rectangular cells. Each entity (ball, wall or contact) is mapped into a cell (or cells) that it occupies. Each cell stores the addresses of each entity that map into it and from here it is easy to identify the neighbors of a given entity.

The computer time necessary for the map and search operation is not dependent on the number of entities in the system but on its size and shape, thus the computer time for neighbor detection is directly proportional to the number of entities (and not quadratic).

Another technique used to reduce the computation time is to form "virtual contact" between balls or balls and walls that are not in contact but within a certain distance from each other. In this way all contacts or potential contact can be tracked without running the contact detection algorithm every time step. Remapping, however, needs to be done every time an entity leaves or enters the volume of a cell.

# Appendix B

## Measurement Device Setup and Calibration

This appendix describes the measurements sensors, their setup and calibration for the field tests as well as for the direct shear apparatus.

### B.1 Strain Gauge Setup and Calibration

#### B.1.1 Setup

The strain gauges used for force measurement during the field test were all coupled in a full bridge configuration, this includes the gauges on the tractor lower links, top link and the connecting rod.

Figure B.1.1 shows the wire connections for the full bridge along with the colors for the lead wires running to the Spider™ and the numbers of the pins on the 15 point plugs that was used. The wires marked "bridge" are part of a sensing circuit of the Spider™ that can be used to compensate for voltage drop when long lead wires are used. These were not used for this setup and were bridged out on the plug.

The strain gauges were bonded in a Poisson's configuration, thus gauges 1 and 3 were aligned with the loading direction, and 2 and 4 were bonded perpendicular to the loading direction. Gauges 2 and 4 were only used to complete the full bridge in order to increase measurement sensitivity. They also provided temperature correction. The strain gauge specifications are tabulated in table B.1.1.

#### B.1.2 Calibration

The lower links and top link were calibrated by tensioning it by a mobile crane and calibrating it against a load cell. Figure B.1.2 shows the calibration setup for

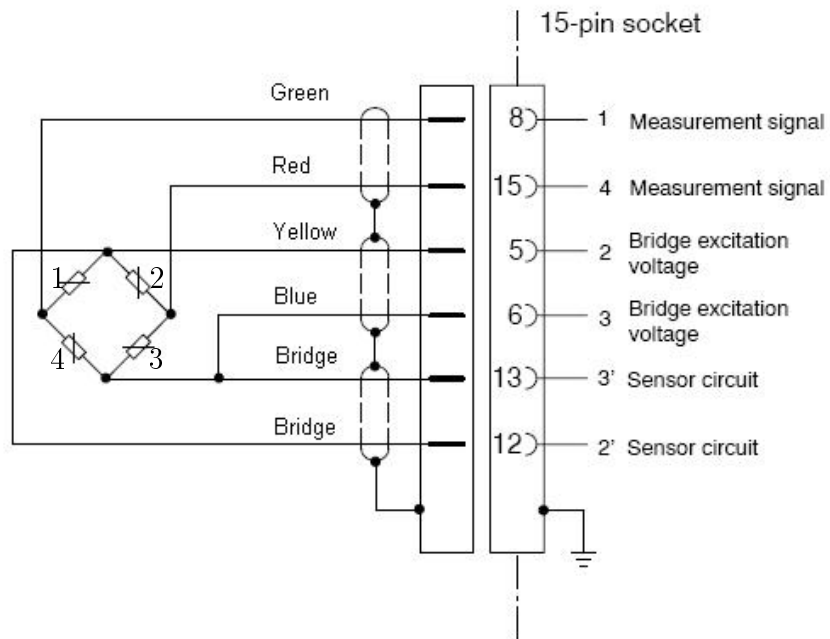


Figure B.1.1: Full bridge wiring diagram

Table B.1.1: Strain gauge specifications

Manufacturer	Vishay Micro-Measurements
Type	CEA-06-240UZ-120 (student gauge)
Resistance @ 24 °C	$120 \Omega \pm 0,3 \%$
Gauge factor @ 24 °C	$2,075 \pm 0,5 \%$
Transverse sensitivity @ 24 °C	$+0,4 \pm 0,2 \%$





**Figure B.1.2:** Calibration setup and load cell connection

**Table B.1.2:** Spider™ information

Manufacturer	Hotinger Baldwin Messtechnik (HBM)
Type	Spider8 4,7 kHz carrier-frequency (8 channel)

a lower link. The link was fixed to the ground on the one end and to the crane on the other via a five ton load cell.

Four dynamic calibrations were done on each arm by tensioning it to 2,2t for the lower links and 1,2t for the top link. When the respective loads were reached the load was released slowly. The load cell output and the strain gauge output were read and recorded with a Spider™ and the laptop computer with Catman™3 software (the same used for the field testing, Spider info given in table B.1.2).

The mV/V reading of the links were plotted against the force reading from the load cell to determine a calibration constant. A linear trend line was fitted through each data set and an average for the slopes of the four tests done was used as calibration constant. Figure B.1.3 shows a typical calibration curve that was

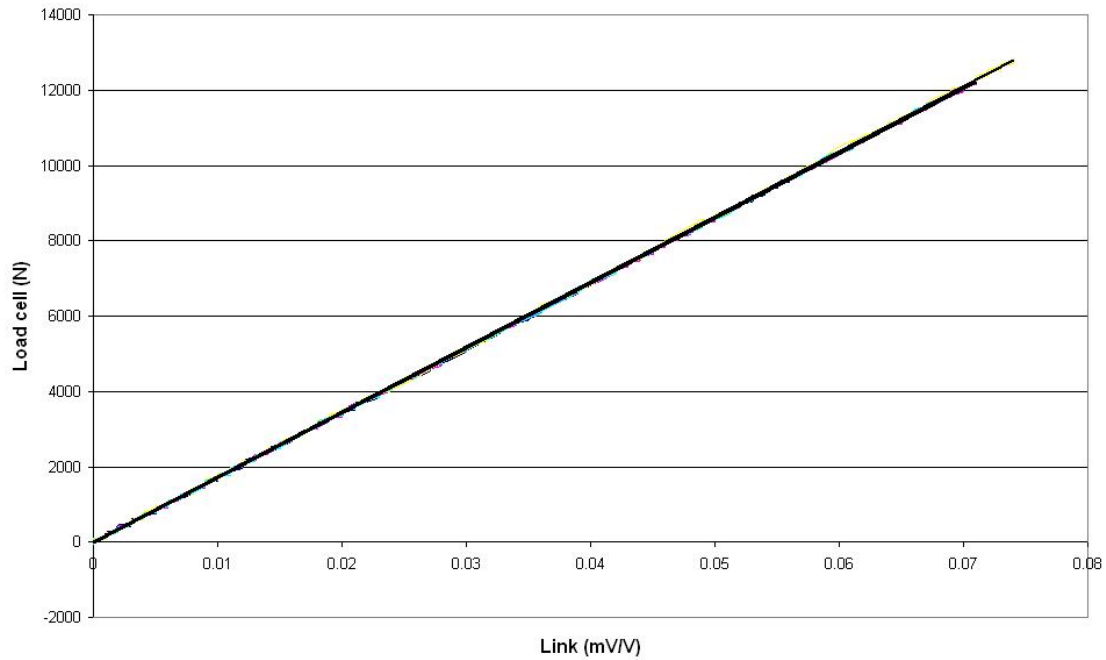


**Figure B.1.3:** Typical calibration curve (top link)

**Table B.1.3:** Calibration constants

Left lower link	131 879,33 N/(mV/V)
Right lower link	105 520,75 N/(mV/V)
Top link	172 521,25 N/(mV/V)

obtained, this one is for the top link.

The calibration values for the lower and top links are tabulated in table B.1.3.

## B.2 Shear Box Sensor Calibration

The sensors used on the direct shear apparatus included a load cell and two Linear Variable Differential Transducers (LVDT).

The load cell used with the shear apparatus was a 2 kN HBM load cell with specifications and calibration constant as shown in table B.2.1.

The LVDTs was Wykeham Farrance transducers and needed calibration (range and serial number given in table B.2.2). The LVDT used for the horizontal displace-

**Table B.2.1:** Shear box load cell information

Manufacturer	Hotinger Baldwin Messtechnik (HBM)
Type	U2AK
Full load	2 kN
Calibration value	2 kN=2 mV/V
Serial no.	D82867

**Table B.2.2:** LVDT information

Manufacturer	Wykeham Farrance England
Horizontal LVDT	
Type	HS25 (25 mm extension)
Serial no.	HS25/3839
Vertical LVDT.	
Type	HS10 (10 mm extention)
Serial no.	HS10/3980

ment measurement had a range of 25 mm and the one used for vertical displacement measurement, a range of 10 mm. They were calibrated with the aid of a Instron extension meter calibration set.

The calibration device (shown in figure B.2.1) consists of a moveable and fixed platen. The moveable platen is moved via a screw mechanism with a turn knob calibrated like a micrometer (shown in figure B.2.1, right), with an accuracy of  $2\ \mu\text{m}$ .

The main body of the LVDT's were fastened to the fixed platen and the extendable core rested against the moveable platen. The LVDTs were then extended from zero to full range in five equal increments, at each increment the knob reading of the calibration device and the reading from the LVDT (via a Spider<sup>TM</sup> and laptop) was recorded. The LVDTs were extended to full range and returned in the same increments to zero, this cycle was repeated twice for each LVDT.

The mV/V readings of LVDTs were plotted against the displacement reading from the calibration device in order to obtain a calibration constant for each LVDT. The average value obtained from the four curves (two extension, two compression) was used as the calibration constant, for each LVDT. A typical calibration curve is shown in figure B.2.2 and the calibration constants for the two transducers are tabulated in table B.2.3. The slope is negative due to the fact that the LVDT output is a maximum at zero extension.

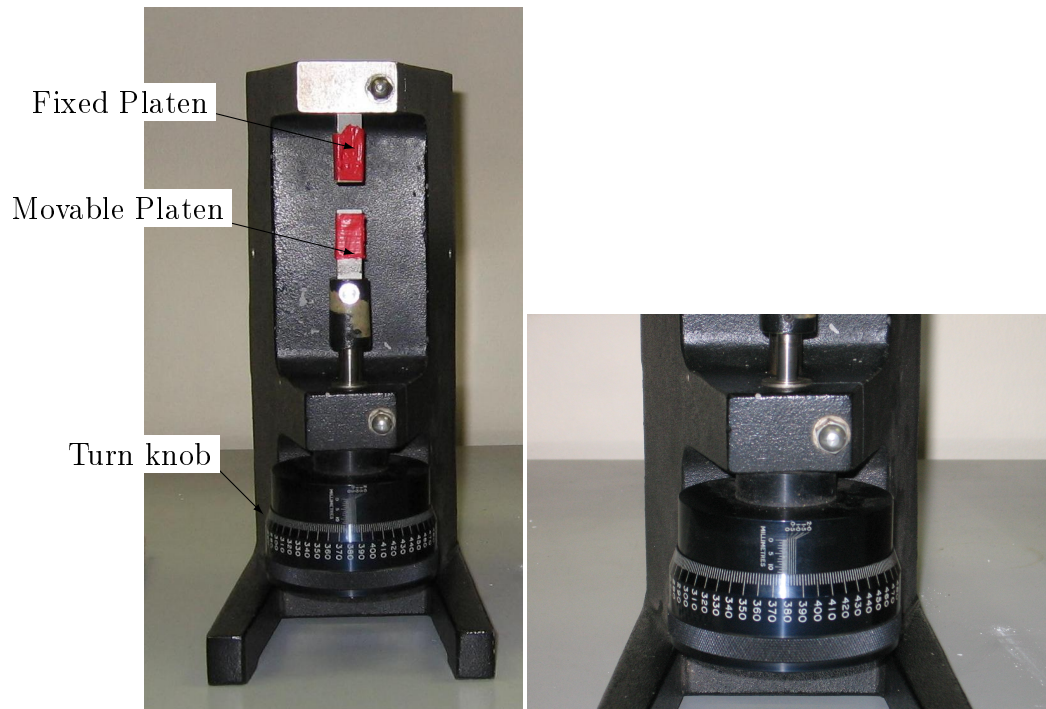
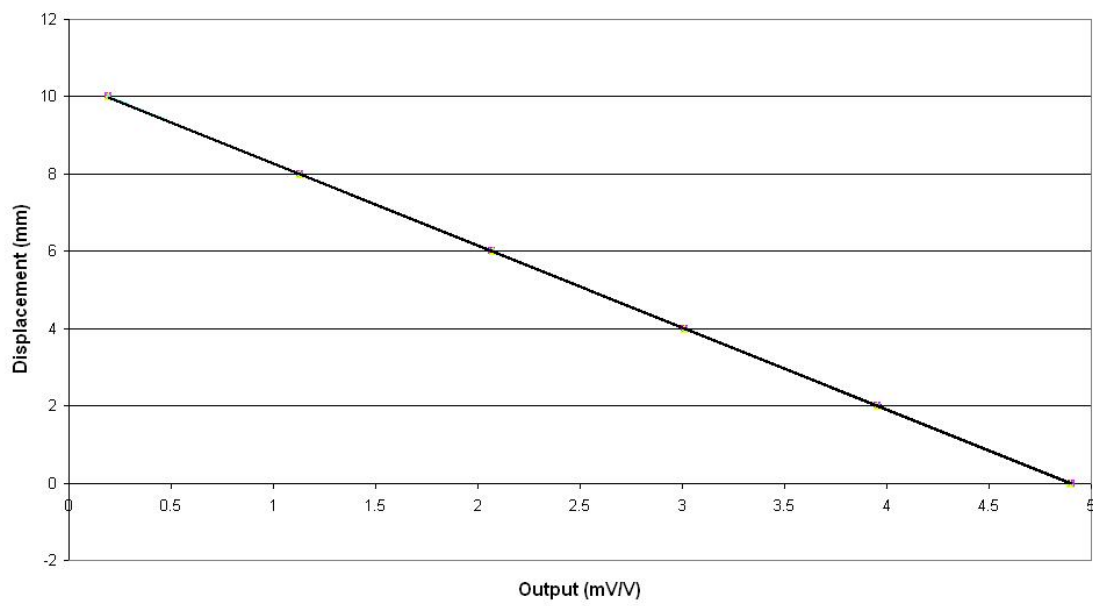


Figure B.2.1: Instron calibration device

Table B.2.3: Calibration constants for LVDTs

Vertical LVDT	$-2,124 \text{ mm}/(\text{mV}/\text{V})$
Horizontal LVDT	$-3,664 \text{ mm}/(\text{mV}/\text{V})$



**Figure B.2.2:** Calibration curve for vertical displacement LVDT

# Appendix C

## Soil Property Testing

### C.1 Direct Shear Tests

The shear tests were done with a Wykeham Farrance model 25300 (serial no: 779) direct shear apparatus as was depicted in figure 4.2.1. The tests were conducted according to the *BS 1377 – 7 : 1990* standards and procedure. The shear box dimensions as measured before the tests are tabulated in table C.1.1.

Since the soil in its natural state in the field are only under pressure of its own weight, the range of normal loads used during the shear tests were at the lower limit of the machine. The three pressures tested at were: 27,52 kPa, 55,05 kPa and 82,57 kPa. These pressures were calculated as follows:

$$P = \frac{m \times g \times r}{A} \quad (\text{C.1.1})$$

where  $m$  is the mass of the weights that was placed on the loading frame (1 kg, 2 kg and 3 kg respectively),  $g$  is the gravitational acceleration (9,81 m/s<sup>2</sup>),  $r$  is the moment arm ratio of the loading frame (for this machine  $r = 10$ ), and  $A$  is the area of the shear box as stated in table C.1.1.

The shear force was measured by the load cell on the machine. The force data

**Table C.1.1:** Shear box dimensions

Length of box	59,7 mm
Width of box	59,7 mm
Area of box	0,003 56 m <sup>2</sup>
Depth of box from base plate to top of top half	44,5 mm

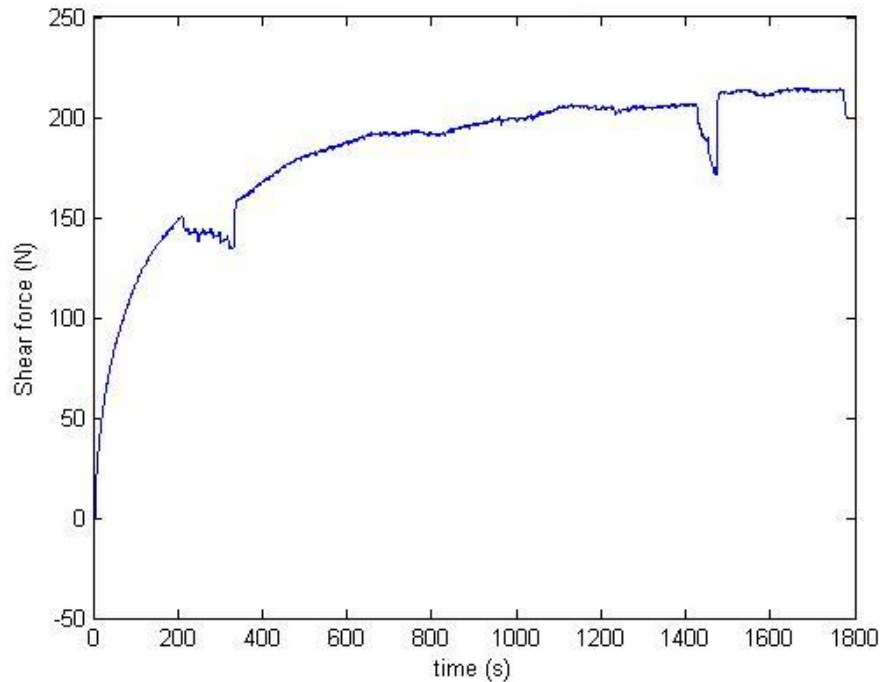


**Figure C.1.1:** Shear force vs. time for 2kg normal load

was analyzed in Matlab to obtain the maximum force, which was divided by the box area to determine the shear stress. A typical shear force vs. time data set from the tests is shown in figure C.1.1.

The maximum measured shear stress for the different normal loads, were plotted with shear stress on the vertical axis and normal stress on the horizontal axis so as to represent points on Mohr circles. A straight line was fitted to these points and the slope of this line was taken as the internal friction angle of the soil and its intercept with the vertical axis were taken as the soil cohesion. Such a plot is shown in figure C.1.2. The normal and shear stress values for this specific test set are given in table C.1.2 along with the friction angle and cohesion.

## C.2 Soil/Metal Friction Coefficient

The soil/metal friction coefficient and adhesion was determined in a similar manner as the soil internal friction angle and cohesion. Instead of filling both halves of the shear box with soil, the bottom half was covered with a mild steel plate and the top filled with an undisturbed soil sample.

The same normal loads were used as in the shear tests and are tabulated along

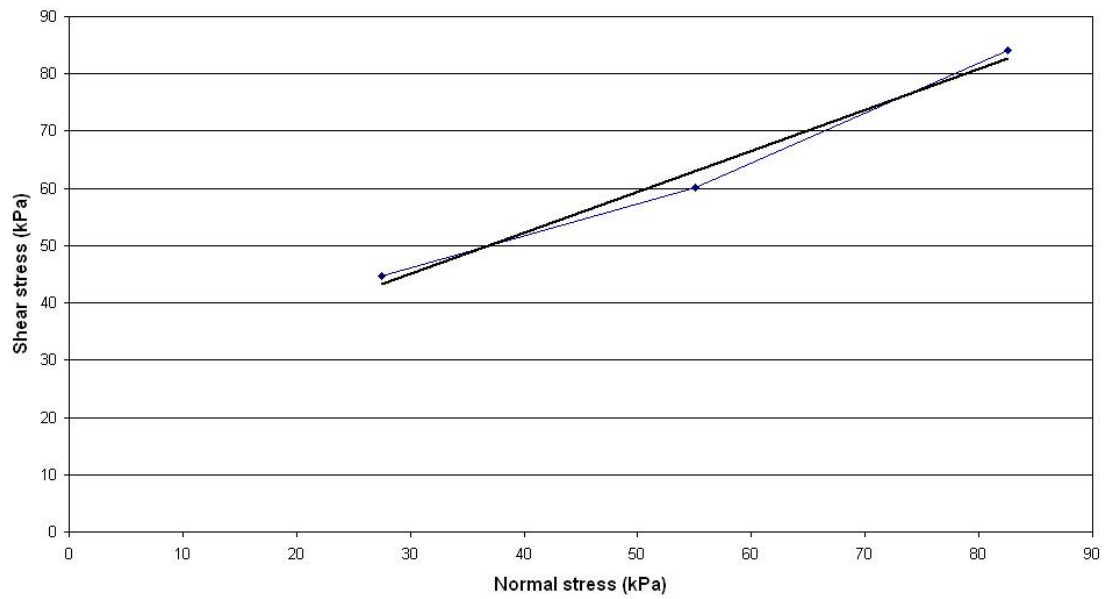


**Figure C.1.2:** Shear stress vs. normal stress with linear regression line

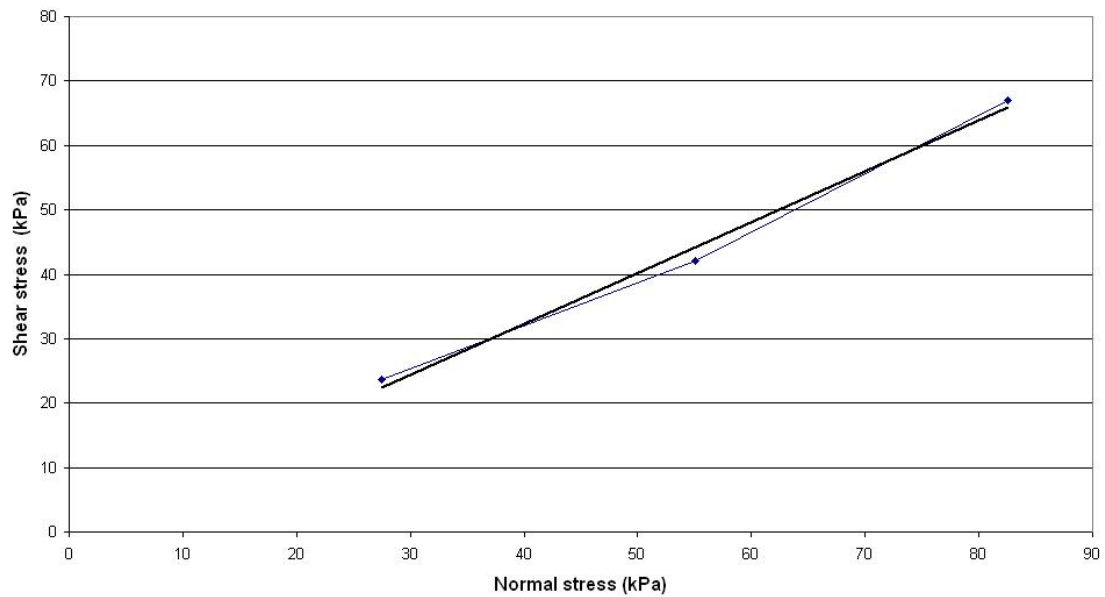
**Table C.1.2:** Shear test data and results

Normal stress kPa	Shear stress kPa
27,525	44,679
55,049	60,234
82,574	84,038
Friction angle	Cohesion
35,56°	23,625 kPa



**Table C.2.1:** Shear test data and results for soil/metal friction coefficient

Normal stress kPa	Shear stress kPa
27,525	23,568
55,049	41,993
82,574	66,934
Friction angle	Adhesion
38,23°	0,8 kPa

**Figure C.2.1:** Shear stress vs. normal stress for soil/metal friction coefficient with linear regression line

with the accompanying shear stresses in table C.2.1. The friction angle and adhesion obtained are also tabulated in table C.2.1. Figure C.2.1 shows the shear vs. normal stress graph for this test.

### C.3 Compression Test

Compression tests were done on the soil to determine its stiffness in order to calibrate the numeric model. The compression test done here was done in the shear apparatus by using its vertical displacement meter and vertical loading frame. This compression test resembles a confined compression test done in a compression test apparatus.

For this test the bottom half of the shear box was covered with the mild steel plate and only the top half of the box was filled with soil. This was done in order to minimize the effect of shear forces, from the walls of the box, on the compression cycle.

After the undisturbed soil sample has been placed in position, the loading plate and frame was put in position along with the vertical displacement meter. The displacement reading was zeroed at this point with no load on the loading frame. The soil sample was loaded in increments by adding weights to the loading frame starting at total weight of 1 kg going on to 2 kg, 3 kg and finally 5 kg. The load was then released by removing the weights in the same increments.

Each time a weight is added or removed the displacement is allowed to stabilize before the displacement reading is taken. The resultant curve obtained from this is shown in figure 4.2.2.

### C.4 Particle Size Analysis

The particle size analysis was done with a variation on the pipette method described in Black *et al.* (1965) and the classification was done according to the USDA classification scheme.

Samples from the three soil layers were oven dried and sieved with a 2 mm sieve. The < 2 mm fraction was used for further analysis.

A sample of this soil was mixed with distilled water to obtain a saturated solution for the measurement of the soil electrical resistance. The three samples had resistances far exceeding 500  $\Omega$ , thus the amount of soluble salts in the soil was negligible. It was thus not necessary to remove any salts from the soil.

A 25 g sample was taken in beakers for each soil layer and wetted with distilled water. After the addition of 5 ml of Hydrogen Peroxide ( $H_2O_2$ ) the samples were placed over a hot water bath and heated. A chemical reaction took place and frothing occurred. When excessive frothing occurred the beakers were removed from the heat and allowed to cool, small amounts of ethanol was dripped onto the foam to brake the surface. More  $H_2O_2$  were added and the beakers were placed back on the heat. This procedure was followed until the chemical reaction stopped. The beakers were then placed in an oven to dry the samples at 105 °C. The dry samples was then

weighed to determine the amount of organic matter removed.

After organic matter removal distilled water was added along with a dispersing agent to loosen the soil particles from one another. This mixture was then transferred to a mixing flask and mixed for 5 min with an electrical mixer. It was then passed through a  $53\ \mu\text{m}$  sieve into a 11 measuring cylinder. The  $> 53\ \mu\text{m}$  fraction was thoroughly washed and washings added to the cylinders. The measuring cylinders were then filled to 11 with distilled water.

The sand fraction ( $> 53\ \mu\text{m}$ ) was then oven dried and passed through a nest of sieves. This nest of sieves comprised of a  $500\ \mu\text{m}$ ,  $250\ \mu\text{m}$ ,  $106\ \mu\text{m}$  and  $53\ \mu\text{m}$  sieve and a pan, in sequence. Each sieve and the pan was weighed. The sand was placed on the top sieve and covered, the whole nest was then placed on a sieve shaker for 5 min. Each sieve and the pan was then weighed with the sand in order to determine the mass of each fraction.

The fractions still in the cylinders were allowed to settle. It was then stirred up with a hand stirrer for 1 min. A fraction was then extracted with a 25 ml pipette at a depth of 100 mm and released in a tared ceramic dish. This fraction contains the  $< 20\ \mu\text{m}$  fraction (coarse silt, fine silt and clay). The cylinders were again stirred up with a hand stirrer, for 4 min. Another fraction was extracted at a depth of 100 mm and released into a tared ceramic dish. This fraction contains the  $< 5\ \mu\text{m}$  fraction (fine silt and clay). The cylinders were then left to settle for 5 h 25 min. The  $< 2\ \mu\text{m}$  (clay) fraction was then extracted at a depth of 100 mm and released into a tared ceramic dish.

The ceramic dishes were then heated to evaporate the water and dry the soil fractions. The weight of these soil fractions were then determined in order to calculate a concentration of each fraction in the soil according to the following equation:

$$C_c = \frac{(m_p - D_c)}{V_p} \quad (\text{C.4.1})$$

where  $C_c$  is the corrected concentration of the soil fraction in g/L,  $m_p$  is the mass from the pipette samples in g,  $D_c$  is the concentration factor for the amount of dispersing agent added to the mixture (0,012 in this case), and  $V_p$  is the pipette volume (25 ml).

To determine the concentration of coarse silt alone, the concentration of the fine silt and clay must be subtracted from it. Thus the weight of the second pipette sample must be subtracted from the first sample. The weight of the fraction in the pan left after the sieving of the sand fraction was added to the weight of the coarse silt fraction. To determine the concentration of the fine silt alone, the concentration of the clay fraction must be subtracted from it. Thus the weight of the third pipette sample must be subtracted from the weight of the second sample.

**Table C.4.1:** Soil fraction percentages

	Top	Middle	Bottom
Clay	7,84 %	6,11 %	4,51 %
Fine silt	17,97 %	14,48 %	6,44 %
Coarse silt	5,80 %	6,64 %	8,21 %
Total silt	23,77 %	21,11 %	14,64 %
Fine sand	15,03 %	15,56 %	14,88 %
Medium/Fine sand	23,36 %	23,97 %	22,73 %
Medium sand	13,64 %	15,20 %	15,04 %
Coarse sand	12,78 %	14,03 %	20,07 %
Total sand	64,80 %	68,76 %	72,73 %

**Table C.4.2:** Average fraction content over depth of soil

Clay	6,15 %
Silt	19,84 %
Sand	68,76 %

To determine the percentage of each sand fraction in the soil, the weight left on each sieve was divided by the total weight left after organic matter removal. The same for the silt and clay fractions, the respective concentrations was divided by the total sample weight after organic matter removal. The percentage of each fraction for the different soil layers are as shown in table C.4.1. The soil was classified according to the average clay, silt and sand content over the entire depth of the soil tested, table C.4.2 shows the average fraction content. According to the USDA classification system, this is classified as a sandy-loam soil.

## C.5 Bulk Density

The bulk density was determine with the aid of the clot-method as described in Chapter 4. This section will only show a sample calculation of the soil bulk density.

Just for clarity equation 4.2.1 will be repeated here:

**Table C.5.1:** Parameters for density calculation

$m_{sa}$	0,4863 kg
$m_{pa}$	0,0123 kg
$m_{spw}$	0,2165 kg
$m_{ods}$	0,4723 kg
$\rho_w$	998 kg/m <sup>3</sup>
$\rho_p$	900 kg/m <sup>3</sup>

$$\rho_b = \frac{\rho_w m_{ods}}{m_{sa} - m_{spw} + m_{pa} - (m_{pa} \rho_m / \rho_p)} \quad (\text{C.5.1})$$

where

$\rho_w$  is the density of water at the temperature of determination

$m_{ods}$  the oven dry mass of the clot

$m_{sa}$  the net mass of the clot in air

$m_{spw}$  the net mass of soil plus wax in water

$m_{pa}$  the mass of wax coating in air and

$\rho_p$  the density of wax.

The values of these parameters for a specific soil clot are tabulated in table C.5.1. The water density was at a temperature of 15°. The mass of wax in air was determined by subtracting the mass of the clot from that of the clot with wax.

The oven dry mass of the clot was determine with the aid of equation C.5.2. The water content for this specific clot ( $\theta_w$ ) was 0,0295 g/g.

$$m_{ods} = \frac{m_{sa}}{1 + \theta_w} \quad (\text{C.5.2})$$

By substituting the tabulated values into equation C.5.1, the bulk density for this specific clot was determined to be 1755,95 kg/m<sup>3</sup>. This specific soil sample was from the bottom soil layer.

Two soil samples for each layer of soil was tested and an average for each layer was used to determine an average for the soil in total. The bulk densities of each sample is tabulated in table C.5.2, the averages for each layer and the total average is tabulated in table C.5.3.

**Table C.5.2:** Sample densities

Top 1	1701,38 kg/m <sup>3</sup>
Top 2	1667,11 kg
Middle 1	1659,95 kg/m <sup>3</sup>
Middle 2	1651,91 kg/m <sup>3</sup>
Bottom 1	1755,95 kg/m <sup>3</sup>
Bottom 2	1733,21 kg/m <sup>3</sup>

**Table C.5.3:** Average densities

Top average	1684,24 kg/m <sup>3</sup>
Middle average	1655,93 kg/m <sup>3</sup>
Bottom average	1744,58 kg/m <sup>3</sup>
Total average	1694,92 kg/m <sup>3</sup>

**Table C.6.1:** Moisture content

Top	5,97 %
Middle	5,09 %
Bottom	4,17 %
Total average	5,08 %

## C.6 Moisture Content

The moisture content of the soil was determined by taking a sample from each soil layer, weighing it, drying it till constant weight and weighing it again. The difference in weight before and after drying was the weight of the water in the original samples. This weight was then divided by the original mass of the sample to determine the weight percentage of moisture of the soil. The moisture content of each soil layer and average for the soil as a whole is tabulated in table C.6.1 as weight percentage.

# Appendix D

## Experimental Data

### D.1 Draft Force

The data recorded for the force measurement was analyzed in a spread sheet. Here the zero load readings and the calibration constants were incorporated to give force values. The forces from the two lower links were added to give the total lower link force, which was multiplied with the cosine of the lower link angle with horizontal ( $4,1^\circ$ ), and with the cosine of the angle the links made with the direction of travel ( $10,3^\circ$ ), to give the horizontal force component. The top link force was also multiplied with the cosine of its angle (with horizontal,  $14,1^\circ$ ) and added to the horizontal component of the total lower link force to obtain a total horizontal (draft) force. Figure D.1.1 shows the total horizontal force, total lower link force, and the top link force for a specific test run done without vibration, and figure D.1.2 shows one with vibration.

It should be noted that the top link is in compression during the test run, thus the force is negative and is effectively subtracted from the lower link force. It should also be pointed out that the forces shown at the beginning and end of the graph (where the draft is negative), was measured when the implement was in the raised position. Since the angles of the linkage differs from when the implement is in working position and in the raised position, these force are not correct and was thus not used in any further calculations.

After discarding the incorrect forces, as described above, a (10%) trim-mean was calculated for the steady state portion of each test run. A 10% trim-mean is the average of the data set calculated after the top 5% and bottom 5% of the data values were discarded, thus reducing the effect of any out lyres in the data.

The difference between trim-mean for test runs done adjacent to each other, with and without vibration, was taken as the reduction in draft force. Table D.1.1 shows the trim-mean values for test runs as well as the differences calculated for

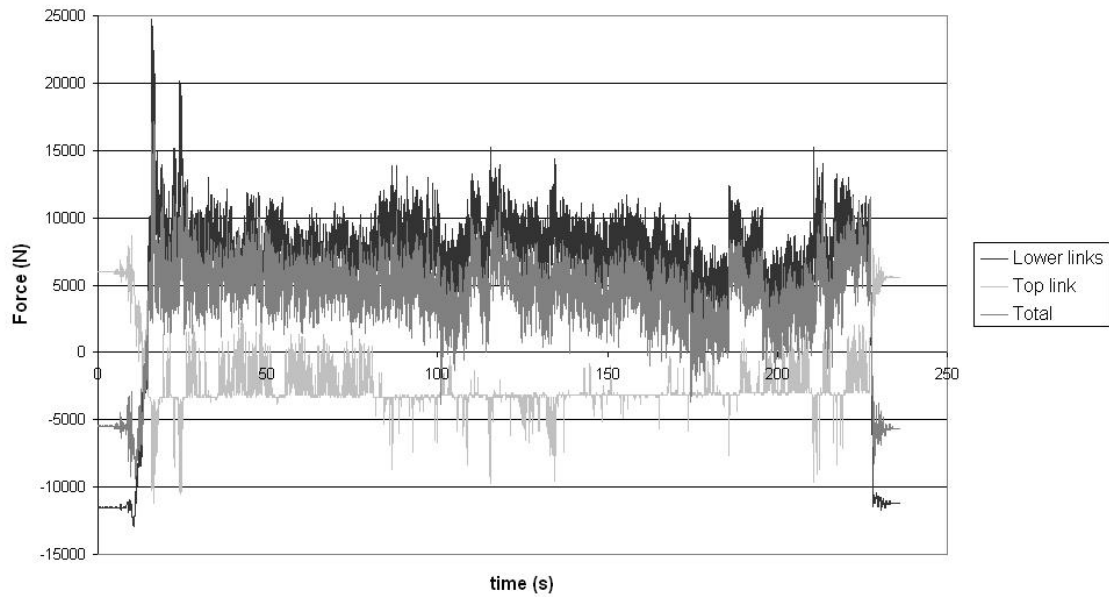


**Figure D.1.1:** Horizontal force components for a test run without vibration

**Table D.1.1:** Draft results for 12,7 Hz test

Test run	Mean	Mean	Difference	
	No vibration	Vibration	Draft	%
1	4,75 kN	2,74 kN	2,01 kN	42,4 %
2	5,35 kN	1,17 kN	4,18 kN	78,0 %
Average				60,2 %

the 12,7 Hz frequency and table D.1.2 for the 16,1 Hz frequency.

## D.2 Soil Profile Measurement

The soil profile was measured with a pin profile meter as shown in figure 4.3.2. With the profile meter the depth of the disturbed soil was measured at 20 mm horizontal intervals and plotted as shown in figure 4.5.2. Two samples were measured for each test run, and samples taken for adjacent runs (with and without vibration) were taken at the same point in the length of the field (next to each other)

The area of the disturbed soil was determined with the aid of the trapezium numerical integration method. The area was determined as follows:



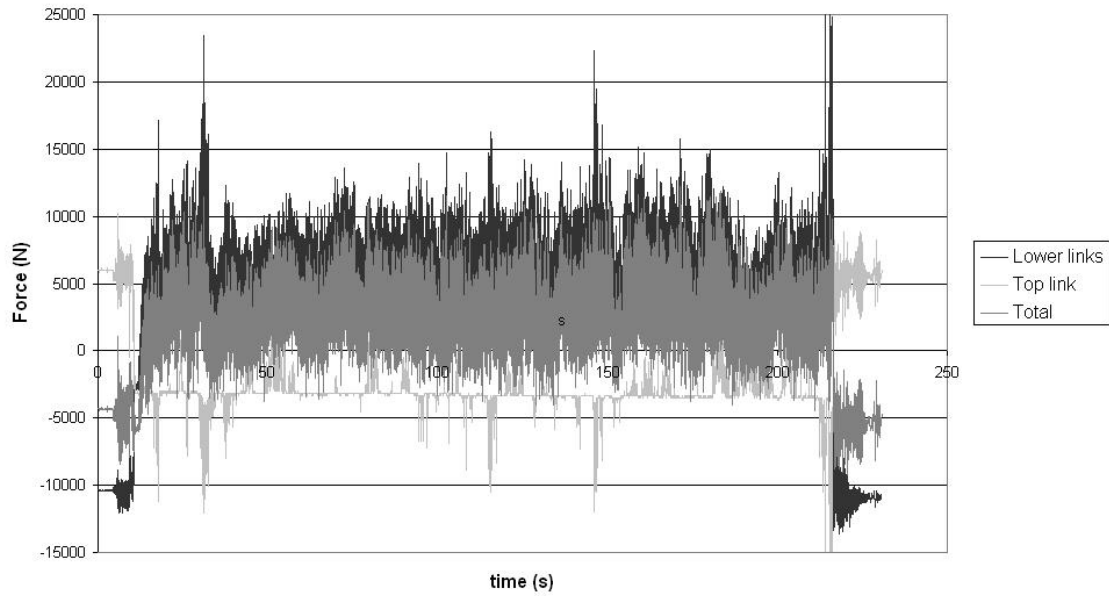


**Figure D.1.2:** Horizontal force components for a test run with vibration

**Table D.1.2:** Draft results for 16,1 Hz test

Test run	Mean No vibration	Mean Vibration	Difference Draft	%
1	4,44 kN	2,71 kN	1,73 kN	39,0 %
2	6,40 kN	2,57 kN	3,82 kN	59,8 %
3	4,40 kN	1,76 kN	2,64 kN	60,1 %
			Average	52,9 %

**Table D.2.1:** Area loosened for 12,7 Hz frequency

Test run	Area nv	Area wv	Diff
1 sample 1	70 700 mm <sup>2</sup>	78 460 mm <sup>2</sup>	10,98 %
1 sample 2	67 160 mm <sup>2</sup>	78 900 mm <sup>2</sup>	17,48 %
2 sample 1	66 160 mm <sup>2</sup>	73 460 mm <sup>2</sup>	11,03 %
2 sample 2	81 040 mm <sup>2</sup>	79 900 mm <sup>2</sup>	-1,41 %
		Average	9,52 %

**Table D.2.2:** Area loosened for 16,1 Hz frequency

Test run	Area nv	Area wv	Diff
1 s1	77 360 mm <sup>2</sup>	78 820 mm <sup>2</sup>	1,89 %
1 s2	85 480 mm <sup>2</sup>	113 660 mm <sup>2</sup>	32,97 %
2 s1	91 300 mm <sup>2</sup>	99 200 mm <sup>2</sup>	8,65 %
2 s2	93 320 mm <sup>2</sup>	103 320 mm <sup>2</sup>	10,72 %
		Average	13,56 %

$$A = \frac{1}{2}h (y_0 + 2y_1 + 2y_2 + \dots + 2y_{n-1} + y_n) \quad (\text{D.2.1})$$

where  $h$  is the horizontal distance between measurements and  $y_i$  ( $i = 1 \dots 46$ ) is the vertical measurements. Tables D.2.1 and D.2.2 show the area disturbed soil for the tests runs with and without vibration as well as the differences.

# Appendix E

## Simulation Data

### E.1 Draft Force

All the forces exerted on the walls in a *PFC3D* model are directly accessible to the user. The sum of the forces exerted in the  $x$  direction on the set of walls comprising the tine was taken as the draft force on the tine. Similarly, all the forces in the  $z$  direction was taken as the vertical forces on the tine. The moments exerted on the walls around a specified axis was also directly available to the user. The moment around an axis running through the point resembling the pivot point of the real tine, and running parallel to the  $y$  axis was taken as the moment exerted on the tine.

This data obtained from the simulation was analyzed in a spread sheet where the average values for the steady state portions of the data were calculated. Figure E.1.1 shows typical draft force data obtained from the simulations for a vibration run as well as for a non vibration run. Lines showing the average values of these two simulations runs are also shown. The draft forces obtained from the simulations are tabulated in table E.1.1 for *run 1* and table E.1.2 for *run 2*.

**Table E.1.1:** Draft force for simulation *run 1* (30 mm amplitude)

Frequency	Velocity ratio	Draft force (N)	Draft reduction (%)
No Vibration	0	1002,084	0
8,71 Hz	1,85	670,370	33,10
12,7 Hz	2,69	623,876	37,74
16,1 Hz	3,41	588,443	41,28
20 Hz	4,24	574,280	42,69
24 Hz	5,09	590,908	41,03

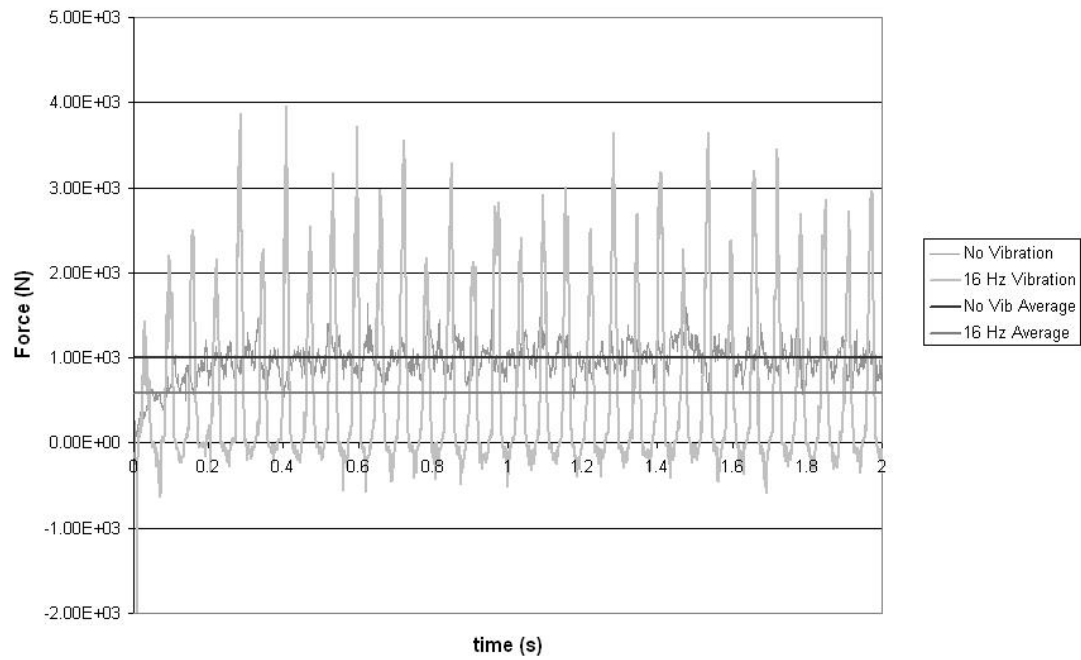


**Figure E.1.1:** Draft force for a simulation run with and without vibration

**Table E.1.2:** Draft force for simulation *run 2* (40 mm amplitude)

Frequency	Velocity ratio	Draft force (N)	Draft reduction (%)
6,53 Hz	1,85	624,954	37,63
9,53 Hz	2,69	541,382	45,97
12,08 Hz	3,41	538,207	46,29
15 Hz	4,24	571,219	43,00
18 Hz	5,09	553,928	44,72

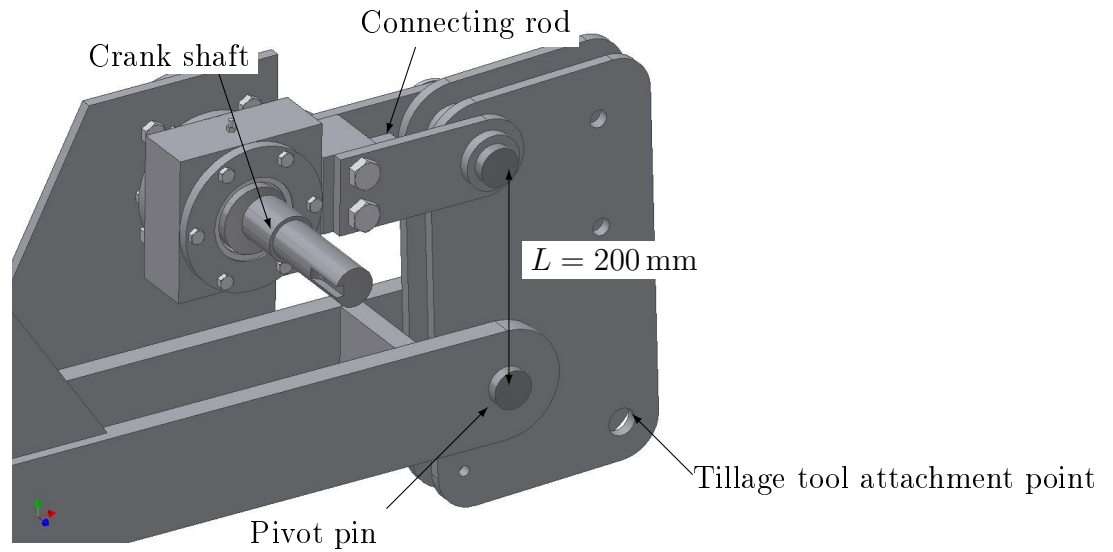


**Figure E.2.1:** Subsoiler crank and pivot layout

## E.2 Power Requirement

The moment exerted on the tine around its pivot point was used to calculate the torque that would have been required at the crank of the physical machine to oscillate the tine.

The moment along with the dimensions of the physical machine was used to calculate the force that would be exerted on the connecting rod between the tine and crank as follows:

$$F_{cr} = \frac{M_t}{L} \quad (\text{E.2.1})$$

Here  $F_{cr}$  is the force in the connecting rod,  $M_t$  is the moment on the tine around the pivot point and  $L$  is the distance between the pivot point and the connecting rod pivot point. Figure E.2.1 shows the position of the pivot point and the distance between the pivot point and connecting rod as well as the crank position.

This force along with the moment arm of the crank around the shaft was then used to calculate the torque in the crank shaft. The angular velocity of the tine is an input in the simulations, thus the exact position of the crank is known at each time step. The exact position of the crank, and hence its moment arm, can be derived from the tine position.

When the tine is in the vertical position, which is its starting position with angular displacement zero, the crank moment arm is at its maximum. When the tine is at a maximum angular displacement (velocity is zero) the crank moment arm is zero. The crank moment arm follows the same function with time as the

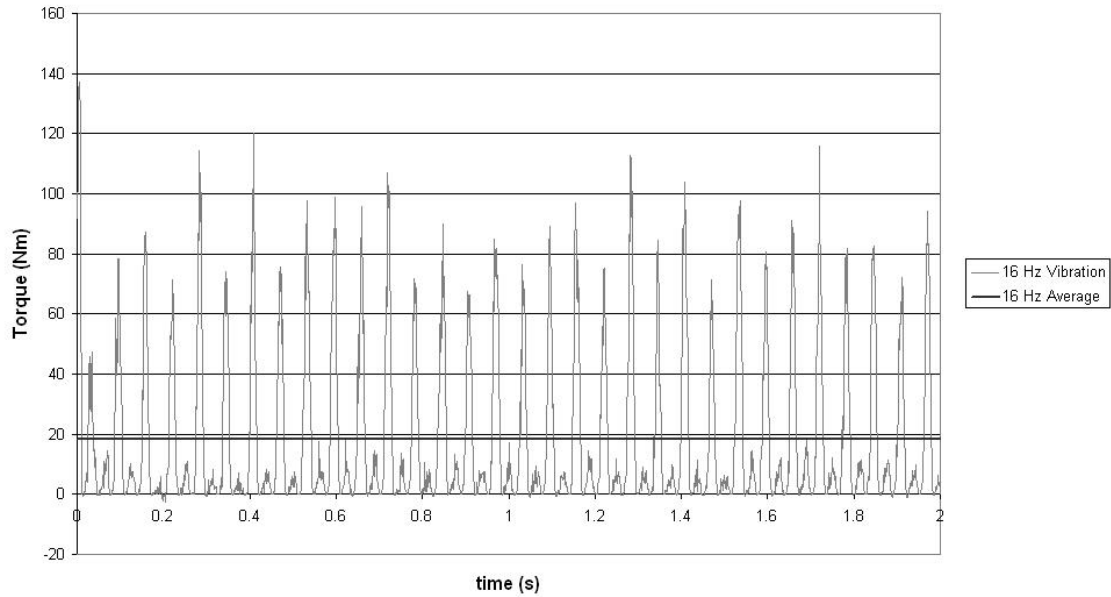


**Figure E.2.2:** Torque on crank shaft

tine velocity, which is a cosine function, with the same rotational frequency. Thus the moment arm follows the following function with time:

$$R_{crank} = A \cos(\omega t) \quad (\text{E.2.2})$$

Here  $R_{crank}$  is the crank moment arm,  $A$  is the amplitude of the moment arm,  $\omega$  is the rotational velocity ( $\omega = 2\pi f$  where  $f$  is the vibrating frequency) and  $t$  is time. The amplitude for *run 1* is 7,5 mm and for *run 2* the amplitude is 10 mm. Figure E.2.2 shows a typical torque graph obtained from the above calculations.

Multiplying the average torque by the rotational velocity of the crank yielded the power required to oscillate the tine. The power consumption and power ratios obtained for the different vibration simulations are shown in tables E.2.1 and E.2.2 for *run 1* and *run 2* respectively. As mentioned before, the power ratio is the ratio between the total power required with vibration and the total power required without vibration.

**Table E.2.1:** Power consumption data for simulation *run 1* (30 mm amplitude)

Frequency	Velocity ratio	Torque (Nm)	Power cons. (W)	Power ratio
No Vibration	0	0	890,853	1
8,71 Hz	1,85	15,98	1470,615	1,651
12,7 Hz	2,69	18,919	2064,324	2,317
16,1 Hz	3,41	18,503	2383,245	2,675
20 Hz	4,24	18,084	2783,035	3,124
24 Hz	5,09	18,902	3375,708	3,789

**Table E.2.2:** Power consumption data for simulation *run 2* (40 mm amplitude)

Frequency	Velocity ratio	Torque (Nm)	Power cons. (W)	Power ratio
6,53 Hz	1,85	20,224	1385,726	1,556
9,53 Hz	2,69	26,111	2043,990	2,294
12,08 Hz	3,41	25,068	2380,325	2,672
15 Hz	4,24	25,911	2949,830	3,311
18 Hz	5,09	25,192	3341,630	3,751

### E.3 Soil Stresses

The stresses and strain rates was determined at the four measurement spheres as described in Chapter 6. At each of these spheres, a complete stress tensor was extracted. This was used to calculate the maximum and minimum principle stresses from where the maximum shear stress was determined.

In *PFC3D* the stress within a measurement sphere is calculated with an averaging technique where the stresses in all the particles in the sphere are averaged over the volume of the sphere. The stress tensor of a particle is determined by dividing the sum of all the contact forces on a particle by the volume of the particle. The average stress within a sphere is calculated by summing the product of the individual particle stresses and volumes, and dividing it by the sum of the particle volumes and taking into account the porosity of the material as follows (Itasca, 2003a):

$$\bar{\underline{\sigma}} = \left( \frac{1 - n}{\sum_{N_p} V^{(p)}} \right) \sum_{N_p} \underline{\sigma}^{(p)} V^{(p)} \quad (\text{E.3.1})$$

Here  $n$  is the particle porosity,  $V^{(p)}$  is the individual particle volumes and  $\underline{\sigma}^{(p)}$  is the individual particle stresses.

The normal stresses in the  $x$ ,  $y$  and  $z$  direction along with the accompanying shear stresses were extracted form the simulations in tabular form. From here it

was used in a Matlab code for analysis where the the stresses were placed in a tensor matrix as follows:

$$\underline{\underline{\sigma}} = \begin{bmatrix} \sigma_x & \tau_{xy} & \tau_{xz} \\ \tau_{yx} & \sigma_y & \tau_{yz} \\ \tau_{zx} & \tau_{zy} & \sigma_z \end{bmatrix} \quad (\text{E.3.2})$$

The Eigen values of the tensor matrix was determined which yielded the three principle stresses. The maximum and minimum principle stresses were then used to calculate the maximum shear stress as follows:

$$\tau_{max} = \frac{1}{2}(\sigma_1 - \sigma_3) \quad (\text{E.3.3})$$

Here  $\sigma_1$  is the algebraic maximum principle stress and  $\sigma_3$  is the algebraic minimum (Benham *et al.*, 1996).



# List of References

- Abo-Elnor, M., Hamilton, R. and Boyle, J.T. (2004). Simulation of soil-blade interaction for sandy soil using advanced 3d finite element analysis. *Soil & Tillage Research*, vol. 75, pp. 61–73.
- Asaf, Z., Rubinstein, D. and Shmulevich, I. (2006). Evaluation of link-tack performance using dem. *Journal of Terramechanics*, vol. 43, pp. 141–161.
- Bandalan, E.P., Salokhe, V.M., Gupta, C.P. and Niyamapa, T. (1999). Performance of an oscillating subsoiler in breaking hardpan. *Journal of Terramechanics*, vol. 36, pp. 117–125.
- Benham, P.P., Crawford, R.J. and Armstrong, C.G. (1996). *Mechanics of Engineering Materials*. Second edition edn. Prentice Hall.
- Black, C.A., Evans, D.D., White, J.L., Ensminger, L.E., Clark, F.E. and Dinauer, R.C. (eds.) (1965). *Methods of Soil Analysis: Part 1, Physical and Mineralogical Methods*. American Society of Agronomy, Inc.
- Brilliantov, N.V., Spahn, F., Hertzsch, J.-M. and Pöschel, T. (1996). Model for collisions in granular gases. *Physical Review E*, vol. 53, no. 5, pp. 5382–5392.
- Butson, M.J. and MacIntyre, D. (1981). Vibrating soil cutting i: Soil tank studies of draught and power requirements. *J. agric. Engng Res.*, vol. 26, pp. 409–418.
- Butson, M.J. and Rackham, D.H. (1981). Vibratory soil cutting ii: An improved mathematical model. *J. agric. Engng Res.*, vol. 26, pp. 419–439.
- Chi, L. and Kushwaha, R.L. (1991). Three-dimensional, finite element interaction between soil and simple tillage tool. *Transactions of the ASAE*, vol. 34, pp. 361–366.
- Cleary, P.W. (2000). Dem simulation of industrial particle flows: case studies of dragline excavators, mixing in tumblers and centrifugal mills. *Powder Technology*, vol. 109, pp. 83–104.

- Coetzee, C.J. (2000). *Forced Granular Flow*. Master's thesis, Department Mechanical Engineering, University of Stellenbosch.
- Coetzee, C.J., Basson, A.H. and Vermeer, P.A. (2006). Discrete and continuum modelling of excavator bucket filling. *Journal of Terramechanics*.
- Cundall, P.A. and Strack, O.D.L. (1979). A discrete numerical model for granular assemblies. *Geotechnique*, vol. 29.
- Dymond, G.F.D. (2006 August). *The use of DEM in dragline bucket filling*. Master's thesis, University of Stellenbosch Department of Mechanical Engineering.
- Fielke, J.M. (1999). Finite element modelling of the interaction of the cutting edge of tillage implements with soil. *J. agric. Engng Res.*, vol. 74, pp. 91–101.
- Franco, Y., Rubinstein, D. and Shmulevich, I. (2005 September). Determination of discrete element model parameters for soil-bulldozer interaction. In: *Proceedings of the 15th International Conference of the ISTVS*. Hayama, Japan.
- Godwin, R.J. (2006). A review of the effect of implement geometry on soil failure and implement forces. *Soil & Tillage Research*, vol. Article in press.
- Godwin, R.J. and O'Dogherty, M.J. (2006). Integrated soil tillage force prediction models. *Journal of Terramechanics*.
- Godwin, R.J. and Spoor, G. (1977). Soil failure with narrow tines. *J. agric. Engng Res.*, vol. 22, pp. 213–228.
- Itasca (2003a). *PFC3D: Particle Flow Code in 3 Dimentions-Theory and Background*. Itasca Consulting Group, Inc., Minneapolis, Minisota, USA, 2nd edn.
- Itasca (2003b). *PFC3D: Particle Flow Code in 3 Dimentions-User's Guide*. Itasca Consulting Group, Inc., Minneapolis, Minisota, USA, 2nd edn.
- Johnson, K.L. (1987). *Contact Mechanics*. Cambridge Uneversaty Press.
- Kofoed, S.S. (1969). Kinematics and power requirement of oscillating tillage tools. *Journal of Gricultural Engineering Research*, vol. 14, pp. 54–73.
- Koolen, A.J. and Kuipers, H. (1983). *Agricultural Soil Mechanics*. Springer-Verlag.
- Liu, C. and Evett, J.B. (2003). *Soil Properties: Testing, Measurement, and Evaluation*. Prentice Hall.
- Luding, S. (1998). Collisions & contacts between two particles. In: *Physics of Dry Granular Media*.

- Luding, S. (2004). Molecular dynamics simulations of granular materials. In: *The Physics of Granular Media*.
- McKyes, E. (1985). *Soil Cutting and Tillage*, vol. 7 of *Developments in Agricultural Engineering*. Elsevier.
- McKyes, E. and Ali, O.S. (1977). The cutting of soil by narrow blade. *Journal of Terramechanics*, vol. 14, pp. 43–58.
- Mindlin, R.D. and Deresiewicz, H. (1953). Elastic spheres in contact under varying oblique forces. *ASME Journal of Applied Mechanics*, vol. 20, p. 327.
- Mishra, B.K. (2003). A review of computer simulation of tumbling mills by the discrete element method: Part i-contact mechanics. *Int. J. Miner. Process.*, vol. 71, pp. 73–93.
- Momozu, M., Oida, A., Yamazaki, M. and Koolen, A.J. (2003). Simulation of a soil loosening process by means of the modified distinct element method. *Journal of Terramechanics*, vol. 39, pp. 207–220.
- Mouazen, A.M. and Nemenyi, M. (1999). Tillage tool design by the finite element method: Part 1. finite element modelling of soil plastic behaviour. *J. Agric. Engng Res.*, vol. 72, pp. 37–51.
- Niyamapa, T. and Salokhe, V.M. (1993). Laboratory investigations into soil failure under vibratory tillage tools. *Journal of Terramechanics*, vol. 30, pp. 395–403.
- Niyamapa, T. and Salokhe, V.M. (2000a). Force and pressure distribution under vibratory tillage tool. *Journal of Terramechanics*, vol. 37, pp. 139–150.
- Niyamapa, T. and Salokhe, V.M. (2000b). Soil disturbance and force mechanics of vibrating tillage tool. *Journal of Terramechanics*, vol. 37, pp. 151–166.
- Panagiotopoulos, N. (1962). Investigation into the variation of cutting resistance of dozer blade under the effect of oscillation. In: *2nd Inter.l Conf. of the Inter Soc. for Terrain-Vehicle Systems*, pp. 516–545.
- Sakai, K., Hata, S.I., Takai, M. and Nambu, S. (1993). Design parameters of a four-shank vibrating subsoiler. *Transactions of the ASAE*, vol. 36, pp. 23–26.
- Schafer, J., Dippel, S. and Wolf, D.E. (1996). Force schemes in simulations of granular materials. *Journal de Physique 1*.

- Shahgoli, G., Saunders, C., Desbiolles, J. and Fielke, J. (2006). An investigation into the performance of vibratory tillage using straight and bent tines. In: *International Soil Tillage Research Organisation 17th Triennial Conference*, pp. 74–81. Kiel, Germany.
- Shen, J. and Kushwaha, R.L. (1998). *Soil Machine Interaction: A Finite Element Perspective*. Marcel Dekker.
- Slattery, M. and Desbiolles, J. (2003 July). Effect of vibrating tines, multi-depth and multi-pass subsoiling on soil loosening and tractor power use. In: *International Soil Tillage Research Organisation 16th Triennial Conference*, pp. 1149–1156. Brisbane, Australia.
- Smith, J.L., Dais, J.L. and Flikke, A.M. (1972a). Theoretical analysis of vibratory tillage. *Transactions of the ASAE*, pp. 831–833.
- Smith, J.L., Hillman, K. and Flikke, A.M. (1972b). Experimental analysis of vibratory tillage. *Transactions of the ASAE*, pp. 834–837.
- Sokolovski, V.V. (1954). *Statics of soil media*. Butterworth Scientific Publications. (Translated 1960).
- Szabo, B., Barnes, F. and Ko, H.Y. (1998). Effectiveness of vibrating bulldozer and plow blades on the draft force reduction. *Transactions of the ASAE*, vol. 41, pp. 283–290.
- Tanaka, H., Oida, A., Daikoku, M., Sumikawa, O., Nakashima, H. and Kuroyanagi, T. (2005 September). The effect of design parameters of vibrating wide subsoiler in its performance simulated by the distinct element method. In: *Proceedings of the 15th International Conference of the ISTVS*. International Society of Terrain-Vehicle Systems, Hayama, Japan.
- Van der Linde, J. (2005). The design and test of a vibratory mouldboard plough and subsoiler. Tech. Rep., Department Mechanical Engineering, University of Stellenbosch.
- Vu-Quoc, L. and Zhang, X. (1999). An elastoplastic contact force-displacement model in the normal direction: displacement-driven version. *Proceedings of the Royal Society*, vol. 455, pp. 4013–4044.
- Vu-Quoc, L., Zhang, X. and Walton, O.R. (2000). A 3-d discrete-element method for dry granular flows for ellipsoidal particles. *Computer Methods in Applied Mechanics and Engineering*, vol. 187, pp. 483–528.

- Walton, O.R. and Braun, R.L. (1986). Viscosity, granular-temperature and stress calculations for shearing assemblies of inelastic, frictional discs. *Journal of Rheology*, vol. 30, pp. 949–980.
- Zhang, R. and Li, J. (2006). Simulation on mechanical behavior of cohesive soil by distinct element method. *Journal of Terramechanics*, vol. 43, pp. 303–316.